Thesis

Spatially controlled bandgap engineering and charge carrier recombination in lead halide perovskites by optical trapping

(光トラッピングによるハロゲン化鉛ペロブスカイトにおけるバンドギャップ工学と電荷キャリア再結合の空間的制御**)**

Graduate School of Environmental Science

Hokkaido University

Md Shahjahan

September 2021

Acknowledgement

First and foremost, praise is to the Almighty ALLAH for giving me the blessing, strength, opportunity, and endurance to complete my Ph.D. dissertation in time. His continuous grace and mercy were with me throughout my life and even more during my research tenure. I acknowledge the support of all the staff and faculty members at the Graduate School of Environmental Science of Hokkaido University.

I express my greatest appreciation to my Ph.D. supervisor, Prof. Vasudevanpillai Biju, for his motivations, suggestions, comments, and encouragement throughout the journey. I am very grateful for allowing me to work with him in the advanced and fascinating perovskite field.

Also, I also express my sincere gratitude to Dr. Ken-ichi Yuyama for his guidance and supports and, above all, for his helpful discussions and warm guidance to complete my dissertation on time. His insightful discussions and suggestions helped me to improve my research work and think from different perspectives. Also, I would like to offer my humble gratitude to Prof. Yuta Takano for his kind cooperation and helpful directions to safely handle chemicals and apparatus. His kind suggestions in the regular weekly meetings helped me to improve my research work. Thanks to Dr. Takuya Okamoto for helping me with the SEM imaging and picosecond laser system. I would like to acknowledge Prof. Hiroaki Misawa for experimental support with the NIR laser.

I would like to thank Mrs. Atsuko Fujii for her kind support and cooperation in making administrative and daily living aspects easy during my stay in Japan.

I express my gratitude to all the former and current members of the Laboratory of Molecular Photonics, Hokkaido University for their kind support and help. Special thanks to my senior Dr. Md Jahidul Islam, for introducing me to the instruments from the very beginning of my research work. I would like to acknowledge my wonderful friends, Dr. Sushant Ghimire, Dr. Lata Chouhan, Dr. Devika Sasikumar, Bhagya Lakhsmi S. B, Jeladhara Sobhanan, Sachith B. M, and Danyang Chen and others, for being so supportive from the first day of my stay in Lab. I also thank and convey my best wishes to my dear fellows-Hanjun Zhao, Kazuya Yoshida, Xu Feijun, Dong Zhang, and Zhijing Zhang for their friendly and kind cooperation.

I would like to acknowledge my beloved origin-Department of chemistry, University of Dhaka, Bangladesh. I always feel blessed and proud of being a student of the most prestigious University of Bangladesh. I would like to show my gratitude to Prof. Dr. Md. Mufazzal Hossain for his inspirations.

I would like to show my gratitude to my respected parents and beloved siblings for their support throughout my life. Finally, I would like to thank my beloved wife, Dr. Mousumi Akther, for her unconditional support and inspiration to continue and complete my Ph.D. Last but not least, the greatest thanks to my lovely daughter Ayesha Shahreen Ruhana, her smile gave me joy, refreshment, strength, and inspirations.

Abstract

Organic-inorganic lead halide perovskites have attracted extensive attention to the next generation energy-harvesting and light-emitting devices, which is owing to their strong absorption of visible to near-infrared light, brilliant photo- and electro- luminescence, long-range diffusion of electrons and holes, low-temperature solution processability, and. The high degree of defect tolerance. In addition, being a direct bandgap material, the optical and electronic properties of this class of materials can be easily modified in the entire UV-visible to near-infrared region by tuning their bandgaps. On the other hand, laser-based optical trapping is being used in a wide variety of fields to manipulate microscopic objects by confining, assembling, or modifying them from the beginning of the inception by Arthur Ashkin. The optical tweezer is often used in biological system to manipulate viruses, living cells and organelles and in chemistry to grow or confine several molecules such as proteins, amino acids, polymers, nanoparticles, and quantum dots in the focal volume, where the assemblies are formed through trapping. In this thesis, I utilize the potential of an optical trapping system for the site-specific bandgap tuning and halide vacancy filling of lead halide perovskite materials and study the charge carrier dynamics in the fabricated bandgap-graded heterojunctions. This thesis consists of five chapters. In chapter 1, I reviewed the general introduction of lead halide perovskites in terms of their chemical composition, structure, properties, and applications. I discuss the most widely followed synthesis techniques of perovskite microcrystals, nanocrystals, and thin films. I have highlighted the characterization methods of perovskite materials using different microscopic and spectroscopic tools. Subsequently, I explain the charge carrier properties and their recombination pathways, followed by the absorption and emission properties. Furthermore, I describe the halide exchange reactions of perovskites in different dimensions such as nanocrystals, microcrystals, and nanowires, which proceeds homogeneously or site-specifically in the parent crystals. Despite being highly defect tolerant, the abundant defects limit the overall performance of perovskite materials. Hence, I reviewed the origin and types of the defects present in perovskite materials. I further discuss the working principle of an optical trapping system to modify the bandgap and passivate defects in perovskite crystals. In the application section, I reviewed the perovskite solar cells, LEDs, and lasers, and finally, I describe the motivation and objectives of my research work. Chapter 2 discusses the experimental methods and materials used in this dissertation. The chapter includes detailed information on the chemicals and materials used

and the synthesis process of perovskite microcrystals, nanocrystals, and thin films. I used the solvent evaporation technique for preparing microcrystals, and the ligand-assisted reprecipitation method for synthesizing nanocrystals. Thin films of the nanocrystals are prepared by the drop-casting method. In the instrumentation section, I discuss the basic working principle and instrumental setup for the laser trapping system using the 1064 nm near-infrared laser and spectroscopic analysis using 1064 nm and 405 nm continuous-wave lasers. The charge carrier dynamics in perovskites are studied using a time-correlated single-photon counting system. I characterize the perovskite samples using steady-state fluorescence and UV-vis absorption spectroscopy techniques. The sample surface analysis and elemental mapping are also performed using a scanning electron microscope and the energy-dispersive X-ray spectroscopy. In chapter 3, I demonstrate a new laser trapping-based methodology for the site-specific halide exchange reaction in the halide perovskite crystals. In general, the halide exchange reaction proceeds homogeneously in the whole crystal, and the bandgap is varied in the entire region when they are exposed to the reactant halide solutions. Here, I introduce a focused near-infrared laser beam to induce halide exchange reaction in the entire region of the selected small microplates and at the desired center part of the large microplate- and microrod-shaped perovskite crystals in a temporally and spatially controlled manner. I confirmed the site-specific halide exchange reaction via spatio-temporal changes in the photoluminescence emission and spectra under near-infrared laser irradiation and wide-field ultraviolet laser irradiation. I discuss the possible mechanism of the exchange reaction from the viewpoint of local concentration increase of the halide ions at the focal volume under laser trapping. In chapter 4, I discuss the suppression of halide exchange reaction by optically controlled site-specific halide vacancy filling of the perovskite microcrystals. The spontaneous halide exchange reaction of the as-prepared crystals occurs homogeneously in the entire region, which can be suppressed by treating the crystals with a constituent reaction solution. The precursor treatment reduces the halide vacancies of the initial crystals and inhibits the halide exchange reaction in the entire region. I demonstrated such halide exchange suppression at specific sites of the microrod crystals through vacancy filling using a NIR laser beam. The NIR laser irradiation fills the halide vacancies exclusively at the irradiated part, while the characteristic features of the nonirradiated parts remain unchanged. The corresponding photoluminescence spectra, scanning electron microscope images, and energy-dispersive x-ray mapping confirm the halide vacancy filling of the crystals. Furthermore, an increase in the PL lifetime at the irradiated part suggests the suppression of nonradiative recombination

through vacancy filling. In chapter 5, I prepare perovskite heterojunction at desired locations and control the transport and accumulation of charge carriers across the heterojunction in perovskite microcrystals or nanocrystal films. I fabricate microscopic heterojunctions with two distinct bandgap-gradient regions composed of iodide-rich and bromide-rich regions through the site-specific halide exchange reaction. I observed the efficient accumulation of charge carriers in the narrow-bandgap iodide-rich region in the built-in halide gradient structures. The corresponding time-resolved spectroscopic analysis revealed the transportation of photogenerated excitons/charge carriers from the surrounding wide-bandgap bromide-rich regions to the narrow-bandgap iodide-rich region. In summary, this thesis develops the construction of perovskite heterostructures with distinct emission color and bandgap and controls the intrinsic properties of halide perovskite. Such laser trapping-based findings offer a new area of interest toward the fabrication of high-quality perovskite heterojunction-based optoelectronic devices.

Abbreviations and Symbols

A	Absorbance
AFM	Atomic force microscopy
AVC	Antisolvent vapor crystallization
APD	Avalanche photodiode
ASE	Amplified spontaneous emission
BSSG	Bottom-seeded solution growth
CBM	Conduction band minimum
CCD	Charge-coupled device
cm	Centimeter
cw	Continuous-wave
D	Dimensional
DCM	Dichloromethane
DMSO	Dimethyl sulfoxide
DMF	*N,N*-dimethylformamide
EMCCD	Electron multiplying charge-coupled device
ETL	Electron transporting layer
e	Electronic charge
E_g	Band-gap energy
EDX	Energy dispersive X-ray
ETL	Electron transporting layer
FTO	Fluorine-doped tin oxide
GBL	γ-butyrolactone
HTL	Hole transporting layer
IPA	Isopropyl alcohol
ITC	Inverse temperature crystallization
ITO	Indium tin oxide
k_1	The rate constant of monomolecular recombination
k_2	The rate constant of bimolecular recombination
k_3	The rate constant of nonradiative recombination
K_B	Boltzmann constant
LARP	Ligand-assisted reprecipitation

LED	Light-emitting diodes
MA	Methylammonium
MABr	Methylammonium bromide
MAI	Methylammonium iodide
min	Minute
mg	Milligram
mL	Milliliter
Mm	Millimeter
mmol	Millimolar
mW	Milliwatt
μm	Micrometer
μL	Microliter
n	Charge carrier density
NA	Numerical aperture
NCs	Nanocrystals
NIR	Near-infrared
nm	Nanometer
PBS	Polarizing beam splitter
$PbBr_2$	Lead(II) bromide
PeLED	Perovskite light-emitting diode
PL	Photoluminescence
PLQY	Photoluminescence quantum yield
PNC	Perovskite nanocrystals
PSC	Perovskite solar cell
r_a	Ionic radii of A-site cation
r_b	Ionic radii of B-site anion
r_x	Ionic radii of X-site halide ion
rpm	Rotation per minute
SCLC	Space-charge limited current
SEM	Scanning electron microscopy
STL	Solution temperature-lowering
t	time
T	Temperature

TCSPC	Time-correlated single-photon counting
TEM	Transmission electron microscopy
TSSG	Top-seeded solution growth
UV	Ultraviolet
UV-vis	Ultraviolet-visible
VBM	Valance band maximum
v:v	Volume: volume
WGM	Whispering gallery mode
XRD	X-ray diffraction
η	Refractive index
μ	Charge carrier mobility
τ	Photoluminescence lifetime
^{o}C	Degree Celsius
λ	Wavelength
ε	Molar extinction coefficient

Table of Contents

Chapter 1

Introduction

In recent years, a ground-breaking revolution has been achieved in the field of perovskite-based solar cells, lasers, and LEDs due to their incredible optoelectronic properties such as high photoluminescence quantum yield, high absorption coefficient, high charge carrier mobility, tuneable bandgap over the whole ultraviolet-visible-near infrared region and high defect tolerance. Despite of having countless advantages compared to the conventional semiconductor materials, lead halide perovskites are still far from commercialization due to several limitations. Thus, more detailed study to grow high-quality crystals, controlling the bandgap through localized halide exchange reaction, defect passivation, and controlling the carrier properties is still necessary. In this chapter, I briefly discuss the general introduction of lead halide perovskites in terms of their chemical composition, structure, properties, and applications. Since most of the optoelectronic properties and device efficiency depends on the initial crystal quality, I also discuss the most widely utilized growth techniques of perovskite microcrystals, nanocrystals, and thin films. In the next section, I have highlighted the characterization methods of perovskite materials using different microscopic and spectroscopic tools. Subsequently, I explain the charge carrier properties and their recombination pathways, followed by the absorption and emission properties. Furthermore, I describe the spontaneous and spatially-resolved halide exchange reactions of perovskites in different dimensions such as nanocrystals, microcrystals, and nanowires. The solution-processed perovskite crystals contain an abundant number of defects, which adversely affect the performance of perovskite devices. Thus, defect characterization, classification, and passivation are important challenges in the perovskite field. In this regard, the origin and types of the defects are reviewed in this chapter. I further discuss the working principle of an optical trapping system utilized to modify the bandgap and passivate defects in perovskite crystals. In the application section, I reviewed the perovskite solar cells, LEDs, and lasers. Finally, I describe the motivation and objectives of my research work.

1.1 General introduction

The journey of perovskites began in 1839 when Gustav Rose improvised a mineral composed of $CaTiO_3$ and named after famous Russian mineralogist Count Lev A. Perovskiy.[1] Later, in the 1890s, halide perovskites having halide anions instead of oxide ions emerged as a new class of semiconductor materials.[2] In recent years, lead halide perovskites have become the center of attraction for scientists as an alternative to conventional semiconductors because of their implausible optoelectronic properties. The wide optical absorption and emission range, high photoluminescence quantum yield (PLQY), tuneable bandgap, high charge carrier mobility, long carrier diffusion length, and high defect tolerance of these materials have made them a global candidate for next-generation photovoltaic applications such as solar cells, LEDs, photodetectors, sensors and lasers.[3-19]

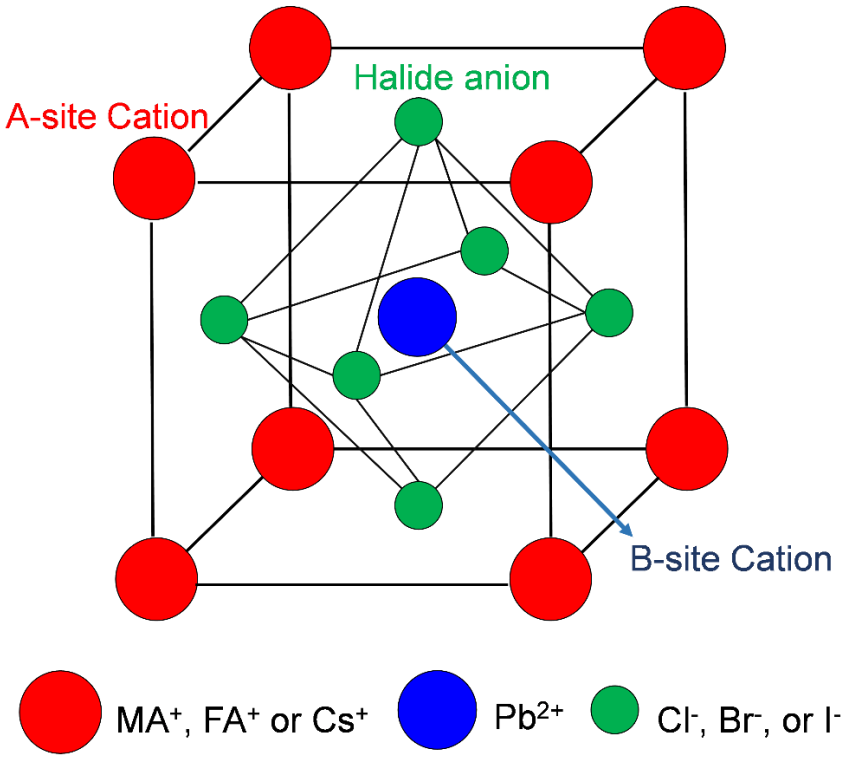

Figure 1.01: The lead halide perovskite crystal structure.

The crystal structure of lead halide perovskites is generally represented by the chemical formula ABX_3, where 'A' stands for the organic or inorganic monovalent cations such as caesium (Cs^+), methylammonium ($CH_3NH_3^+$ or MA^+), and formamidinium ($(CH(NH_2)_2)^+$ or FA^+)), 'B' denotes divalent cations such as Pb^{2+}, Sn^{2+}, Ge^{2+} and 'X' is the halogen anions Cl^-, Br^-, I^-. In a typical cubic ABX_3 crystal structure, the A-site cations fit into the voids of

the corner-sharing BX_6 octahedra. B-site cations are located at the center of the octahedra, which is surrounded by six halide anions.[20,21] The Goldschmidt tolerance factor and the octahedral factor predict the stability of a perovskite crystal/lattice.[22] These factors are expressed as

Tolerance factor, $t = (r_a + r_x)/[\sqrt{2}\,(r_b + r_x)]$

Octahedral factor, $\mu = r_b/r_x$

In this expression, r_a, r_b and r_x are the corresponding ionic radii of A, B, and X ions. Based on the equations, a stable cubic structure is formed when t is in the range 0.9-1.0, and μ ranges from 0.44 to 0.9.[23] An octahedral tilting of this ideal structure occurs when A-site cation is replaced by a smaller cation and results in tetragonal or orthorhombic perovskite phases and the tolerance factor ranges between 0.7-0.9.[24] Furthermore, a large A-site cation leads to the formation of a hexagonal structure with $t > 1$. A stable room temperature phase can also undergo phase transition when the temperature is varied. For example, a room temperature tetragonal $MAPbI_3$ crystal changes to cubic phase at 60 ^oC.[25] Besides, the variation in the halide composition offers the PL emission and optical bandgap tuning throughout the entire ultraviolet-visible-near infrared (UV-vis-NIR) region.

1.2 Synthesis of halide perovskites

The growth technique of lead halide perovskite crystals with different sizes (nano, micro or milli scale) has attained an importance in recent years. Since the basic optoelectronic properties and performance of perovskite-based devices mostly depend on the crystal quality, in this section, I discuss recently developed and the most widely utilized growth techniques for perovskite nanocrystals, microcrystals, and thin films. High-quality bulk crystals ranging from micro to millimeter size can be obtained by the solution temperature-lowering (STL) method, inverse temperature crystallization (ITC) method, anti-solvent vapor-assisted crystallization (AVC) method and laser trapping induced crystallization method. On the other hand, colloidal synthesis of nanocrystals includes hot-injection method and ligand-assisted reprecipitation (LARP) method. Moreover, the fabrication of perovskite thin films with a large size and high quality can be attained by facile one-step and two-step deposition methods.

1.2.1 Synthesis of microcrystals

The synthesis methods of perovskite microcrystals have been developed to attain unbroken and continuous crystal lattices without grain boundaries and fewer defects. Among various growth techniques, the STL method, ITC method, and AVC method are widely applied to grow single perovskite microcrystals. Except for these methods, I discussed here a new approach of growing single perovskite crystals by the laser trapping technique.

The STL method is a widely applied traditional method, which is used for the crystal growth of perovskite crystals. The perovskite solubility in the corresponding acid halide (HX, X= Cl, Br, I) solvents decreases with a lower solution temperature. Based on this principle, Poglitsch et al[26]. obtained MA-based perovskite single crystals in 1987 by cooling the precursor temperature. Briefly, they obtained $MAPbX_3$ crystals by lowering the temperature of a concentrated aqueous solution of HX acid, Pb^{2+}, and $CH_3NH_3^+$ from 100 ^oC to room temperature. In this process, the decrease in the solution temperature induced the solute saturation, and the saturated aqueous perovskite precursor HX solution containing an inorganic metal salt and an organic halide salt slowly form the halide perovskite crystal. Recently, STL method is being used by fixing seed crystals in different positions in the vessel to obtain larger crystals with a regular shape. In general, small size seed crystals are obtained by the STL method. Top-seeded solution growth (TSSG) and bottom-seeded solution growth (BSSG) are commonly used optimal methods for synthesizing of high-quality large single crystals. For instance, Dong et al.[3] reported the synthesis of a bulk single crystal of $MAPbI_3$ with the size of 10 mm × 3.3 mm via the TSSG synthetic route. In this process, the seed crystal is fixed to a silicon substrate on the top half of the precursor solution. The bottom half of the vial containing precursor and seed crystals is heated in an oil bath, while the top half is air-cooled to remove the heat and create a temperature gradient. Because of the temperature disparity between the top and bottom of the solution, the supersaturation is induced in the top solution, which resulted in the formation of bulk $MAPbI_3$ single crystals. Also, the growth of centimeter-sized $MAPbI_3$ bulk single crystal was first reported by Dang et al.[27] with the BSSG method using seed crystals. In this crystal growth process, the tray with a high-quality seed crystal was placed in the middle of the solution and rotated using an electric motor. Finally, the saturated solution was gradually cooled down by decreasing the temperature from 65 ^oC to 40 ^oC, which results formation of a high-quality single crystal with dimensions of 10 mm × 10 mm × 8 mm. Afterwards, Lian et al.[19] also obtained bulk single crystals of 12 mm × 12 mm

× 7 mm dimensions by utilizing a seed crystal fixed to an unreactive platinum wire after decreasing the solution temperature from 100 ºC to 57 ºC. STL method is a simple and effective approach to grow large-sized single crystals with high quality under controlled and stable conditions. However, being time-consuming is the main drawback of this method, limiting its extensive use and led to the domination of other crystallization methods.

The ITC method is now the most extensively used one for the synthesis of perovskite single or mixed halide crystals. This method is suitable for those materials whose solubility in particular solvents is high at room temperature but decreases with increasing temperature. The mechanism is that, at low temperatures, the perovskite forms complexes with the solvent, exhibiting high solubility. As the temperature increases, the bonds break, perovskite molecules become free, and the solubility drops, thus keeping the precursor at

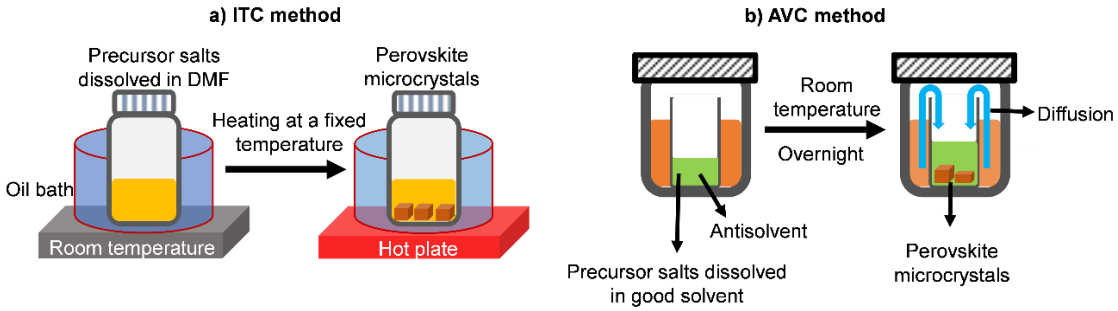

Figure 1.02: Schematic representations of the growth techniques for perovskite single crystals by (a) the ITC method, and (b) the AVC method.

a high temperature can promote crystallization of the crystals. Figure 1.02a shows the crystallization of crystals through the ITC method. The Bakr group, Liu group and Yang group explored the solubility of lead halide perovskites in γ-butyrolactone (GBL), *N, N*-dimethylformamide (DMF), and dimethylsulphoxide (DMSO).[28-32] This method is widely applied to methylammonium and formamidinium lead halide perovskites as well as mixed halide perovskite. For example, the Bakr group first proposed this method in 2015 and synthesized high-quality bulk single crystals of $MAPbX_3$ perovskites based on the solubility in various solutions at different temperatures.[28] To grow $MAPbBr_3$, they added MABr and $PbBr_2$ in DMF solution at room temperature and heated the solution in an oil bath to 80 ºC. Similarly, the iodide solution was prepared at 60 ºC and heated to 110 ºC for the $MAPbI_3$ crystals. The ITC method is a highly effective approach for growing size- and shape-controlled crystals faster compared to other methods. However, the growth rate is hard to control and consequently induces more defects.

The AVC method is used to grow the perovskite materials that are highly soluble in a good solvent but have poor solubility in other solvents. Halide perovskites show good solubility in DMSO, DMF, and GBL, while they are insoluble or show low solubility in dichloromethane (DCM), chlorobenzene, benzene, diethyl ether, etc. The mechanism is to use the large solubility difference of perovskite in different solvents to prepare the crystals. For example, by the diffusion of a highly volatile poor solvent slowly into the precursor solution to decrease the solubility, leading to the growth of high-quality crystals (Figure 1.02b). Based on this hypothesis, the Bakr group achieved millimeter-sized $MAPbX_3$ single crystals, where the anti-solvent DCM slowly diffused into the solution containing precursor solutions dissolved in DMF or GBL.[33] The most prominent feature of the AVC method is that it is a temperature-independent process operated at room temperature. This method can be adapted to grow small-sized single crystals but not large-sized single crystals, thus constraining its effective utilization for producing optoelectronic devices.

Recently, our group reported an innovative method for preparing single perovskite crystals utilizing optical trapping force. Since Ashkin et al.[34] developed optical trapping with the use of a tightly focused laser beam, this technique has been widely used as an optical tweezer for confining and assembling nanoparticles, quantum dots, polymers, etc. in the focal volume.[35,36] We used this laser trapping tool in a spatiotemporally controlled manner to synthesize $MAPbX_3$ single crystals and mixed halide $MAPbBr_nCl_{3-n}$ single crystals.[37,38] For the crystallization of $MAPbBr_3$ by optical trapping, we used 1.2 $molL^{-1}$ $MABr/PbBr_2$ precursor solution dissolved in DMF and subsequently focused a 1064 nm focused laser beam onto the solution surface to induce crystallization. Eventually, by increasing the local concentration of the precursor solution at the focal volume, we obtained crystals of $MAPbBr_3$ at the desired location. Similarly, for the synthesis of $MAPbBr_nCl_{3-n}$ (n=0.5-2.0) crystals, the precursor solution was prepared by dissolving $MABr/PbBr_2$ and $MACl/PbCl_2$ in DMSO/DMF solution mixture and utilized the 1064 nm laser beam to initiate the crystallization. Through this crystallization technique, we could overcome the problem of multiple nucleation at different positions, which is common to other synthesis methods. We grew a single crystal of uniform shape at the desired location by utilizing the potential of laser trapping.

1.2.2 Synthesis of nanocrystals

The nanocrystals of perovskites with high photoluminescence quantum yield are mainly synthesized using the hot-injection method and the LARP method.[39,40] A typical synthesis of perovskite nanocrystals by hot injection method involves dissolving the lead halide

precursor (PbX_2) in octadecene along with oleic acid, oleyl amine and quickly injecting Cs-oleate or Cs-acetate under the N_2 atmosphere and at 140 ºC-200 ºC (Figure 1.03a).

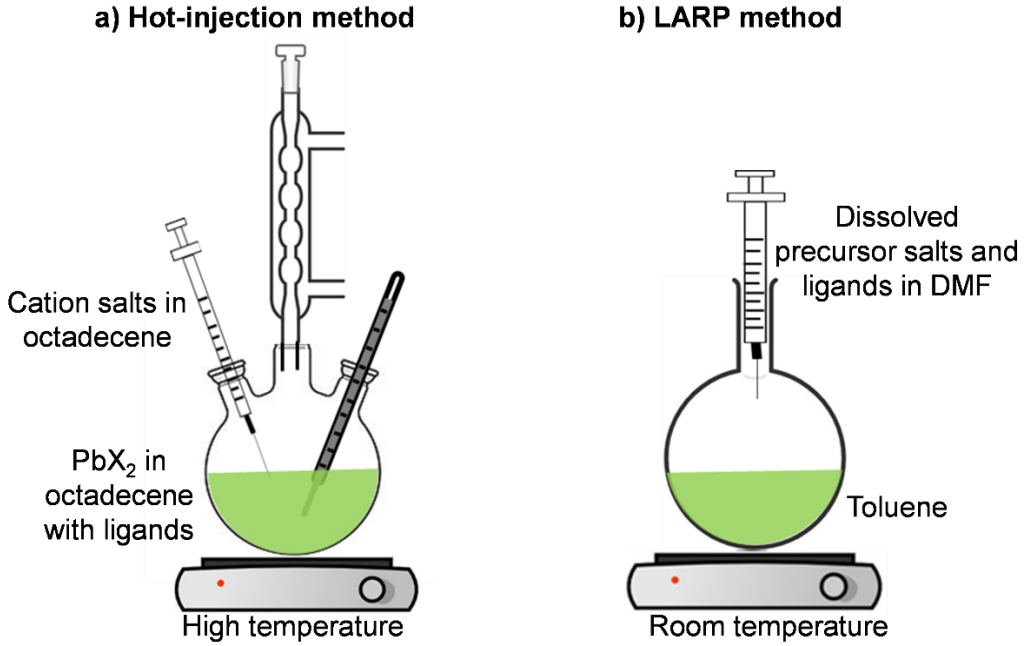

Figure 1.03: Synthetic strategies for the lead halide nanocrystals using (a) hot-injection method and (b) LARP method.

In the entire process, heat is provided to dissolve the long-chain capping ligands. For the precipitation of nanoparticles, the reaction is quenched within a very short time by placing the reaction mixture in an ice-water bath. Finally, the precipitate resuspended in hexane or toluene forms a stable colloidal solution. This method is the most used procedure for the synthesis of $CsPbX_3$ nanoparticles. Kovalenko's group first obtained $CsPbX_3$ nanocubes with 4-15 nm size employing the hot injection method.[39] This method is applicable for the synthesis of shape-controlled halide perovskite nanocrystals with high PLQY up to 95%. However, this method is very sensitive to reaction temperature and the atmosphere.

LARP method to synthesize perovskite nanocrystals is based on the reprecipitation technology, which utilizes the aggregation characteristics of perovskites in the presence of ligands. As shown in Figure 1.03b, during this process, first, the perovskite precursor solution is dissolved in a good solvent such as DMF, DMSO, or GBL along with the long-chain ligands (*n*-octylamine, oleic acid, etc.). The precursor solution is then mixed with the poor non-polar solvents of the perovskite, such as hexane or toluene under continuous stirring at room temperature. The solubility difference between the polar and non-polar solvents initiates the recrystallization of nanocrystals. Finally, the perovskite nanocrystals

are obtained by centrifugation along with other operations. LARP strategy was first carried out by Dong's group in 2015, demonstrating the synthesis of colloidal $MAPbX_3$ nanocrystals with 3.3 nm size.[40] They prepared $MAPbBr_3$ nanocrystals by dissolving MABr and $PbBr_2$ salts as well as the ligands *n*-octylamine and oleic acid in DMF to make a precursor solution. Consequently, the solution mixture was dissolved in toluene under vigorous stirring, and after centrifugation large particles were discarded and $MAPbBr_3$ nanoparticles were obtained. This method is widely used due to its simple and fast operation at room temperature and convenience for scale-up synthesis with 100% PLQY. The main drawback of this process is the degradation and solvation of the resultant nanoparticles in polar solvents which limits their application to photoelectric devices.

1.2.3 Preparation of thin films

Halide perovskite thin films, one of the most important materials to achieve high-efficiency perovskite solar cells can be fabricated by many facile and low-temperature routes. Preparation of the perovskite thin films is broadly grouped into two main categories, namely, the one-step deposition method and the sequential deposition method (Figure 1.04). In a typical one-step synthesis process, a precursor solution is prepared by dissolving all the precursor salts in a polar solvent such as DMF, DMSO, GBL or a mixture of such solvents. Using a spin coater, this precursor solution is then dropped onto a spinning substrate to remove the liquid from its surface. Afterward, through evaporation of the remaining solution by annealing, the perovskite crystallization is initiated onto the substrate, which eventually grows towards a large crystal. The one-step spin coating method was first successfully demonstrated by the Miyasaka group[12] in 2009. They spin-coated precursor solutions of $MAPbBr_3$ and $MAPbI_3$ on a TiO_2 substrate to fabricate the thin films. In this process, they prepared the $MAPbBr_3$ and $MAPbI_3$ precursor solutions by dissolving MABr and $PbBr_2$ in DMF, and MAI and PbI_2 in GBL, respectively. Later, other groups utilized many other one-step deposition techniques like solvent engineering, antisolvent/solvent extraction, gas quenching, drop-casting etc. to achieve the improved morphology of perovskite films.[41-43]

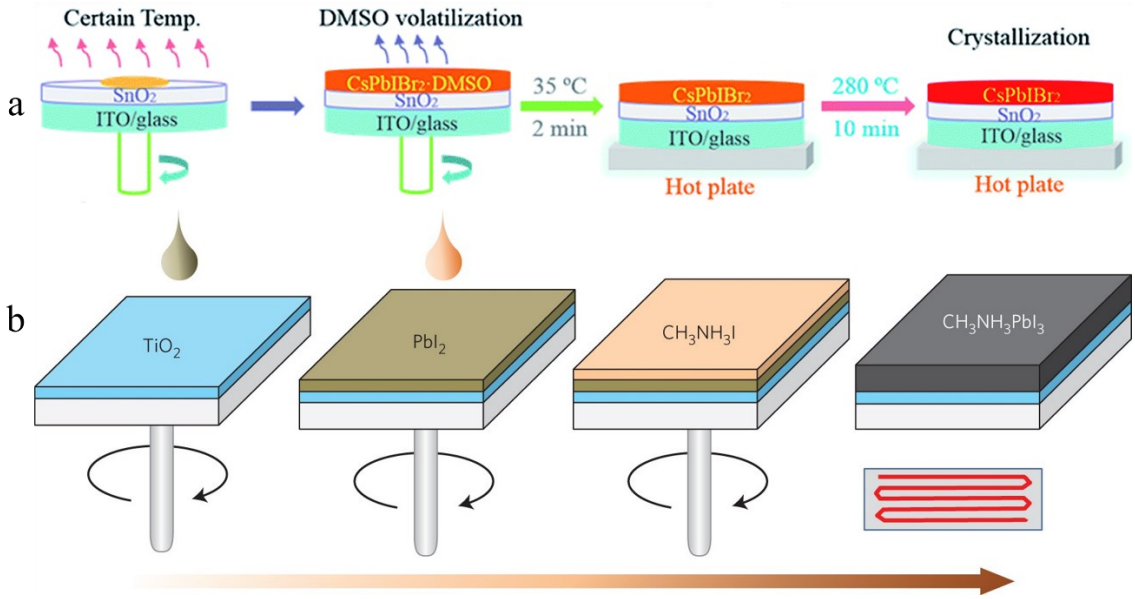

Figure 1.04: Schemes of the deposition methods for the synthesis of perovskite thin films via (a) one-step deposition, and (b) sequential deposition method. Reproduced from (a) Guo et al.,[48] and (b) Im et al.[49]

On the other hand, in a sequential synthesis process, first, a metal precursor solution (usually PbX_2) is deposited on the substrate, and then, the substrate is exposed to an organic salt (AX) to drive the reaction that produces the thin films (Figure 1.04b). Liang et al.[44] reported the fabrication of perovskite film by the sequential deposition method in which the MAI diffuses into the PbI_2 precursor film to form $MAPbI_3$ perovskite by dipping the PbI_2 film in the MAI solution. Apart from these laboratory methods, doctor-blading, spray-coating, inject printing, slot-die coating, soft-cover coating, etc have been adopted for the commercial production of thin films used in perovskite solar cells.[45-47]

1.3 Characterization of perovskites

To reveal the insights of perovskite crystals related to their chemical and electrical properties, different characterization techniques have been employed. The chemical composition, morphology, electronic band structures, and crystallographic patterns are obtained by different electron microscopy and spectroscopy techniques. The most common electron microscopy techniques are scanning electron microscopy (SEM) and transmission electron microscopy (TEM).[50-55] These two microscopic tools are used to understand the size, shape, and thickness of perovskite materials with different dimensions. The crystallization steps to control the thickness of perovskite thin films are monitored with SEM micrographs.[50] SEM studies also identify the changes in the grain boundaries of

perovskite thin films generated during different deposition techniques. Also, the TEM enables high-resolution atomic structure images of perovskite nanomaterials. For example, Figure 1.05a revealed the TEM images of $CsPbX_3$ (X= Cl, Br, I) nanocrystals, where the size of the parent nanocrystals remained unchanged after the anion exchange reaction. Also, nanocrystal with different shapes such as cube, platelet, and rod or wire have been revealed through TEM micrographs.[50,55] Another direct approach to measure the thickness of a particular perovskite crystal is atomic force microscopy (AFM). AFM provides detailed analytical information about the surface roughness of perovskite thin films by mapping the morphological distribution of the film.[56] Energy dispersive X-ray (EDX) spectroscopy is another advanced characterization technique combined with SEM or TEM. The elemental composition of perovskite crystals is calculated from the stoichiometric ratios of elements in the expected crystals.[54,57] Figure 1.05b shows the SEM of a single-crystalline $CsPbBr_3$ nanowire and corresponding elemental distribution of Cs, Pb, and Br determined from EDX mapping. Also, the Pb:I ratio is expected to be 3 in an ideal $MAPbI_3$ crystal but the EDX elemental distribution shows a much higher or lower ratio than expected because of the uncoordinated MAI or PbI_2.[57,58] The crystallographic structure of perovskite crystals is determined by the XRD studies.[28,39,59-61] During the growth of perovskite crystals, they crystallize into different phases such as cubic, tetragonal or orthorhombic.[61] The XRD diffraction patterns of different crystals are specified for different phases, which can be rationalized with size, chemical composition and temperature.[28,39,54] For instance, Figure 1.05c shows the size dependent XRD pattern of $CsPbBr_3$ nanowires, where an orthorhombic crystal structure of the nanowires was found with larger crystal sizes. The dominant miller indices for cubic, and tetragonal phases are (100), (110), (200), (210) and (110), (220), (114), (224) respectively. The miller indices for orthorhombic are similar to the cubic phase, but the peak at 30^o is divided into two. The width of diffraction peaks also determines the particle size of the crystals. When a crystal size is comparable to the Bohr radius, the peak width becomes very sharp while a broadening of these peaks is observed from the crystal size exceeding the Bohr radius. Moreover, the structural orientation of perovskites due to a change in A-site cation or halide composition also shift the diffraction peak to higher or lower 2Θ angle.

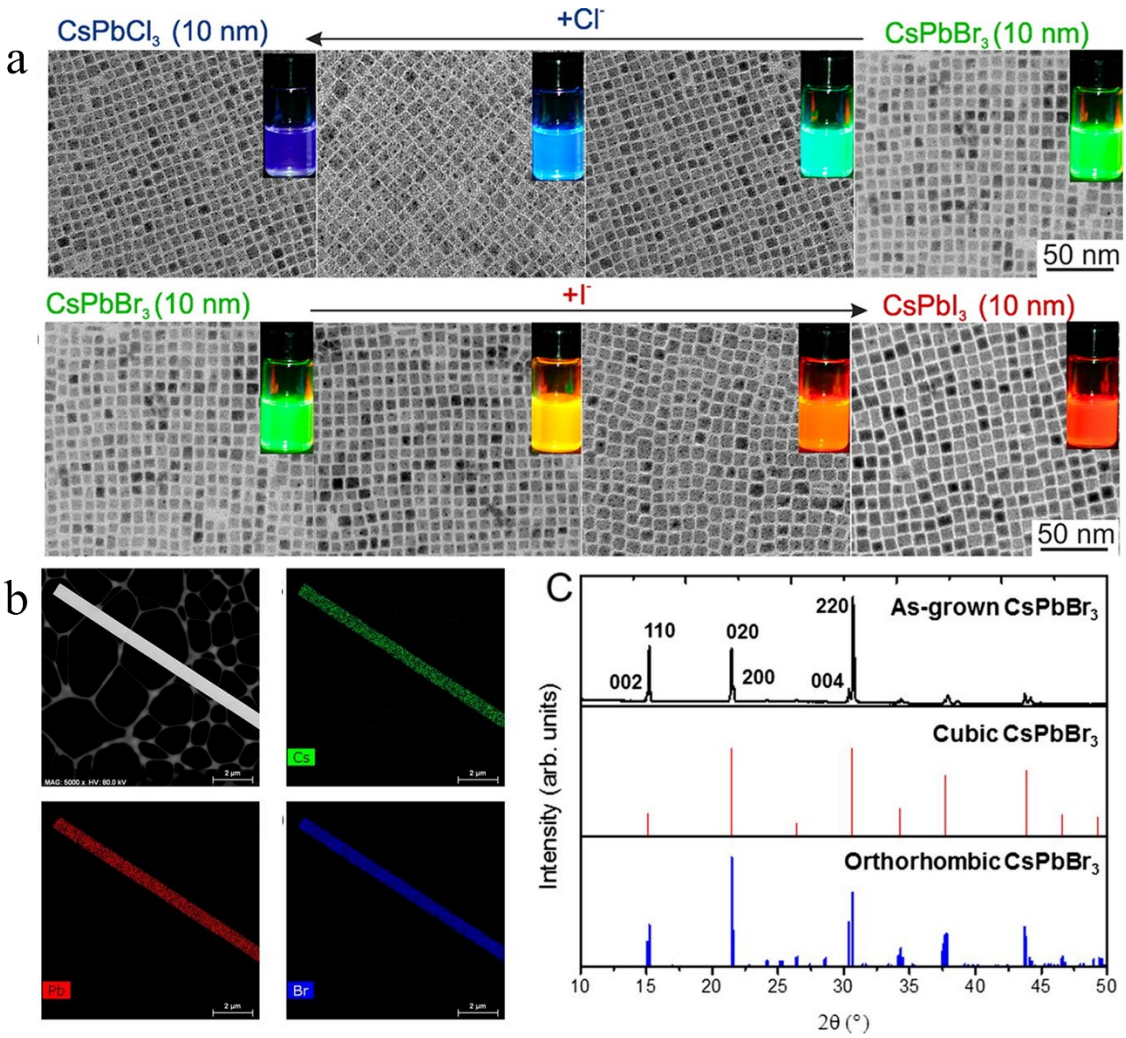

Figure 1.05: Characterization of lead halide perovskites. (a) TEM micrographs of $CsPbX_3$ nanocrystals upon varying the halide ions from Cl^--Br^--I^-, (b) the SEM image of a single $CsPbBr_3$ nanowire combined with the corresponding EDX elemental map images, (C) XRD pattern of an as-grown $CsPbBr_3$ crystal with cubic and orthorhombic phases. Reproduced from (a) Nedelcu et al.[61], (b,c) Eaton et al.[54]

Besides these microscopic characterization techniques, many spectroscopy-based convenient techniques have been developed for the characterization of perovskite materials (Figure 1.06a-c).[64-66] Upon photoirradiation, a perovskite sample absorbs the light and produces electrons and holes, which later recombine to give luminescence. Hence, UV-vis absorption and PL spectroscopy are the fundamental tools to understand the carrier dynamics including, generation, transport, and recombination of the charge carriers.[64,65] UV-vis spectroscopy measures the absorption of atoms and molecules when they undergo electronic transitions from the ground state to the excited state, while the transition from

the excited state to ground states is measured by PL spectroscopy. The PL spectral measurements also reveal the impurity or defect levels and monitor the

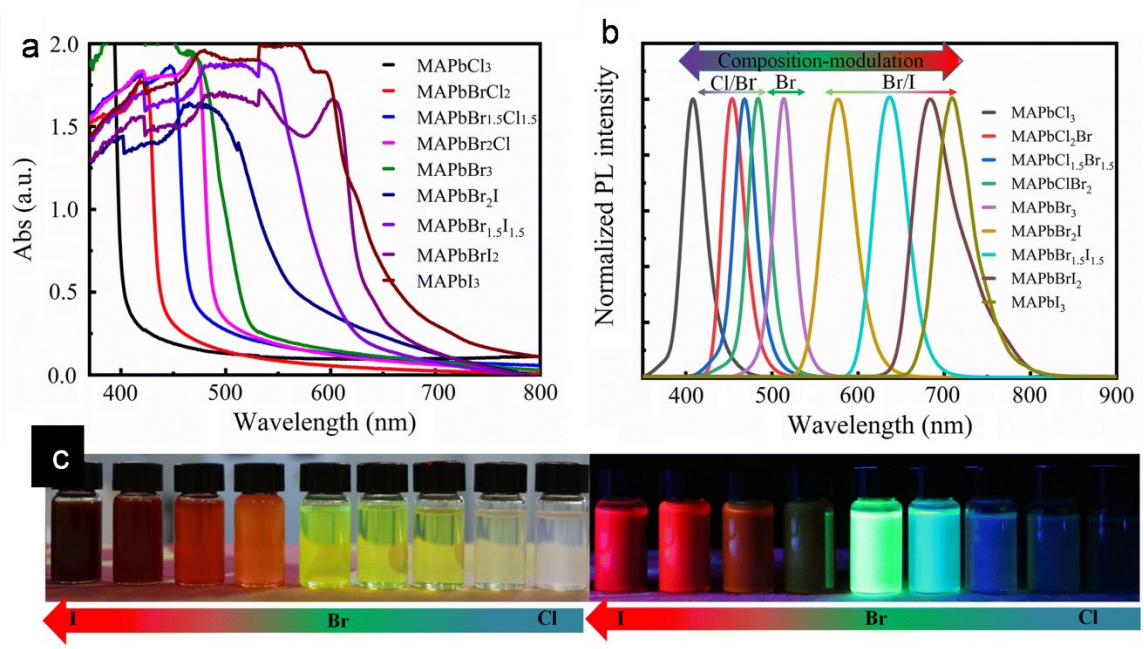

Figure 1.06: Spectroscopic analysis to characterize the optical properties of perovskites. (a) Optical absorption spectra and (b) PL spectra of $MAPbX_3$ perovskite quantum dots as a function of halide composition. Optical images of $MAPbX_3$ solutions in toluene (c)under sunlight and UV light. Reproduced from Zhenfu et al.[67]

by shifting the band-edge emission peaks toward shorter or longer wavelength regions (Figure 1.06)[39,62,63] As shown in Figure 1.06a,b the optical UV–Vis absorption of the $MAPbX_3$ quantum dots showed a single peak with a narrow spectral bandwidth with different halide compositions. Corresponding to the absorption spectra, the emission peaks in the PL spectra also changed from 408 to 710 nm with different halides components. Moreover, different emission colors shown in Figure 1.06c under ambient light and 380-nm ultraviolet light can be achieved through bandgap modification, which are difficult to obtain through direct synthesis.

1.4 Properties of lead halide perovskites

1.4.1 Charge carrier properties

The power conversion efficiency of perovskite-based devices are directly dependent on the charge carrier properties of lead halide perovskites. Hence, it is very important to understand the basic properties such as the carrier mobility, carrier diffusion length, and

carrier lifetime of these materials to fabricate high-performance perovskite devices. Carrier mobility is positively related to the transportation and extraction of charge carriers, 2which can be calculated by different methods like space-charge limited current (SCLC), Hall effect, time-of-flight, field-effect transistor, or THz pulse measurement.[3,70-73] Among these methods, SCLC is the most widely utilized one to calculate the carrier mobility using the following equation,[3]

$$Jd = \frac{9\epsilon\epsilon_o\mu v^2}{8L^3}$$

Here J_d denotes the current density, v is the applied voltage, L is the crystal thickness and μ is the carrier mobility. Again, the diffusion length of perovskites depends on the carrier mobility and carrier lifetime of the corresponding materials.[7,74] The diffusion length of the perovskite materials is estimated from the following derivation,

$$L_D = \sqrt{\frac{K_B T \mu \tau}{e}}$$

where K_B stands for the Boltzmann constant, μ is the carrier mobility, T is the temperature, e is electronic charge, and τ is the PL lifetime. Moreover, the charge carrier lifetime also plays an important role in photovoltaic process. Depending on the dimension, nature, and quality of the materials lifetime values varies from sub-nanoseconds to microseconds. Upon photon absorption, the perovskite becomes electronically excited, where the excitons/charge carriers recombine again radiatively or nonradiatively. The excition/charge carrier recombination pathways can be explained with the following differential equation,[75,76]

$$-\frac{dn}{dt} = k_1 n + k_2 n^2 + k_3 n^3$$

Here, n is the charge carrier density, k_1 is the trap-assisted monomolecular recombination constant, k_2 is the bimolecular radiative recombination rate constant, and k_3 is the nonradiative Auger recombination rate constant. A scheme for the charge carrier recombination pathways in halide perovskites is shown in Figure 1.07.

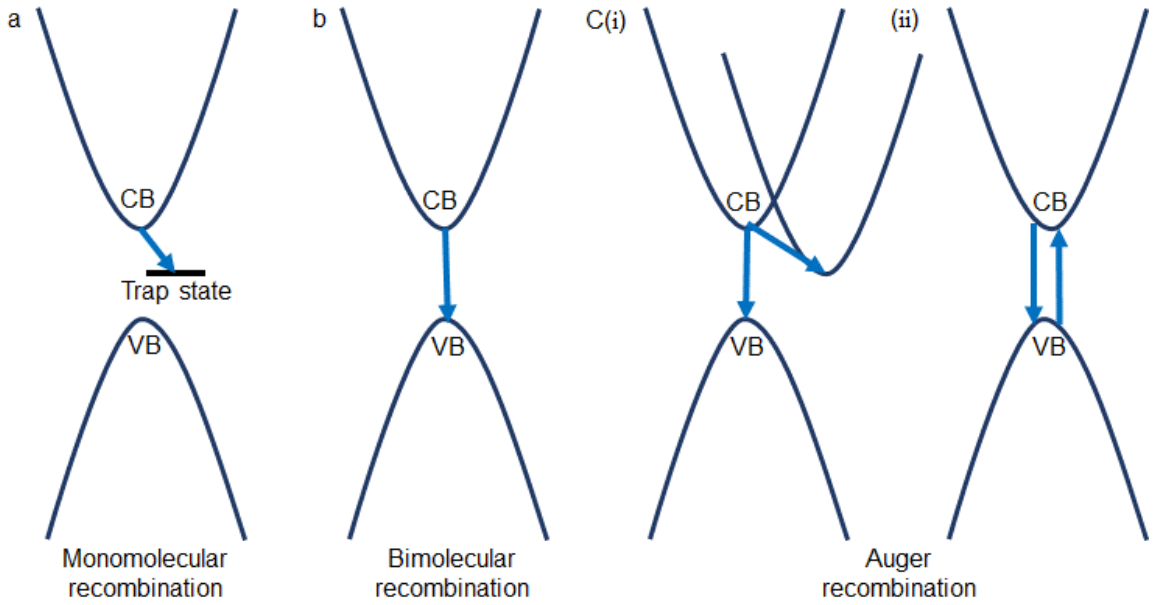

Figure 1.07: A scheme for the charge carrier recombination pathways in halide perovskites: (a) trap-assisted monomolecular recombination, (b) bimolecular recombination, and (c) Auger recombination.

The monomolecular decay component is originated from the trap-assisted recombination and depends on the density and distribution of trap states. As shown in Figure 1.07a, in this process, a single charge carrier such as, an electron, a hole or an excition recombines with a trap in the bandgap. Depending on the material processing the recombination rate differs in a wide range from 4.9×10^6 s^{-1} for mixed halide $MAPbI_{3-x}Cl_x$ to 15×10^6 s^{-1} in a $MAPbI_3$ thin films.[77,78] The bimolecular recombination (Figure 1.07b) means the direct combination of an electron in the conduction band with a hole in the valance band. This process is dominant at moderate charge carrier density when the traps are mostly filled, and recombination takes place radiatively. Moreover, under high charge carrier density, many-body nonradiative recombination, namely, Auger recombination becomes dominant. As illustrated in Figure 1.07c(i, ii), this process involves the recombination of electrons and holes which is transferred to an additional charge carrier known as Auger electron or hole.

1.4.2 Absorption and emission properties of perovskites

Halide-based perovskite shows strong absorption and emission upon light illumination and cover the whole visible to near infrared wavelength region. These materials also exhibit the direct bandgap between the valance band and conduction band, which can be altered by varying the cation and anion.[17,39,40,79,80] The density of states suggests that the conduction

band minimum and valance band maximum of lead halide perovskite materials are located at the p-orbitals of lead and halides, respectively. Thus, the absorption and emission properties can be readily tuned from the short-wavelength region to the long-wavelength region by changing the halide ions from Cl^- to I^-. Similarly, replacing the Pb^{2+} cation with another divalent cation like Sn^{2+} further shifts the wavelength to longer region.[81] Figure 1.08 shows the absorption and emission peak of the $CsPbX_3$ (X= Cl, Br, I) nanocrystals. As shown in Figure 1.08a Protesescu et al tuned the

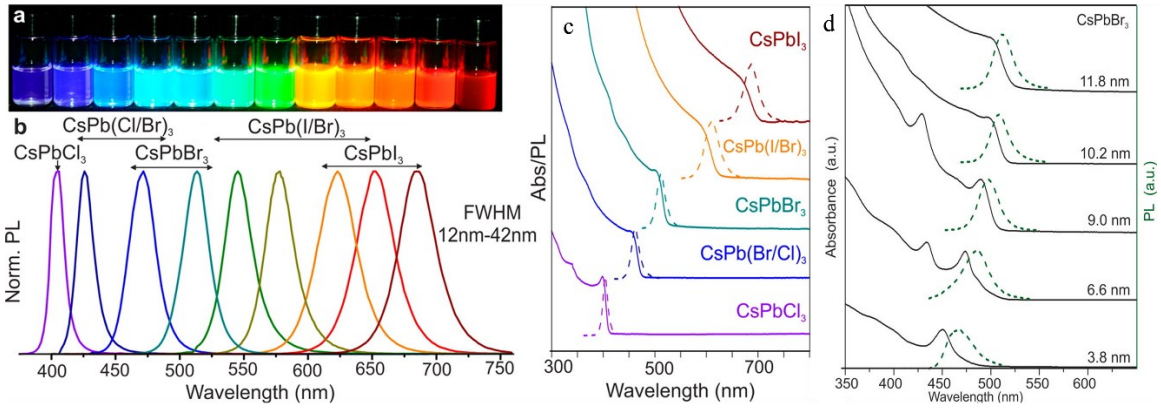

Figure 1.08: (a) A photograph of $CsPbX_3$ nanocrystals under the UV light, showing different PL color depending on their halide compositions, (b) the corresponding PL spectra of halide ion-exchanged $CsPbX_3$ nanocrystals, (c) absorption and emission spectra based on different halide composition, (d) absorption and emission spectra of $CsPbBr_3$ nanocrystals varying with the particle sizes. Reproduced from Protesescu et al.[39]

PL color of the parent $CsPbX_3$ nanocrystals over the entire visible spectral region by adjusting the ratio of halides. They also demonstrated the change in absorption edge and emission maxima from 410-700 nm by changing the halide ions from Cl- to I- (Figure 1.08b,c). Also, these properties of perovskite materials can be controlled by crystal size. Due to the quantum confinement effect, a decrease in the particle size shifts the maxima to lower wavelength region and vice-versa.[39] For example, the absorption edge and emission peak were blue-shifted when the size of $CsPbBr_3$ nanocrystals decreases from 11.8 nm to 3.8 nm (Figure 1.08d).

1.4.3 Halide exchange reaction of lead halide perovskites

The optical properties and chemical composition of halide perovskites can be tuned over the whole UV-visible-NIR spectral region through halide exchange reaction. The substitution of X-site halide ions with Cl, Br, or I ions thus alters the bandgap of perovskites

dramatically over a wide range. As the halide ion of a parent crystal changes from Cl to Br to I, their valance orbital also changes from 3p to 4p to 5p, respectively, which leads to the variation in properties of perovskites. A variety of mixed halide compositions can be attained through halide exchange reactions, which are not possible to fabricate by direct synthesis methods. In a typical halide exchange reaction, the parent crystals are exposed to another halide precursor solution to induce the exchange reaction. Due to the high mobility of halide ions, they diffuse inside the crystal lattice via the solid-state diffusion mechanism and undergo halide exchange reaction by substituting the original halide ions. The halide exchange reaction has been studied extensively in different morphologies of perovskite crystals such as nanocrystals and bulk crystals (Figure 1.09) to attain advanced optical and electrical properties from the parent crystals.

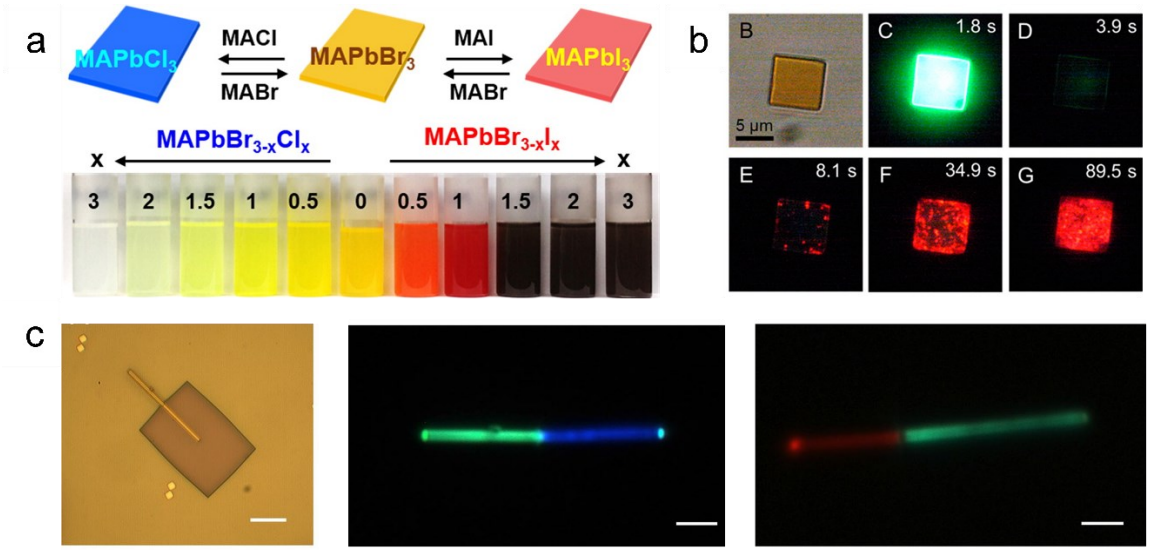

Figure 1.09: Halide exchange reaction of lead halide perovskite crystals in different dimensions. (a) reversible halide exchange reaction of $MAPbBr_3$ nano-plates, (b) gradual halide exchange reaction of a single $MAPbBr_3$ microcrystal with an MAI solution, and (c) partial halide exchange reaction of the $CsPbBr_3$ nanowires. Reproduced from (a) Jang et al.,[84] (b) Karimata et al.,[86] (c) Dou et al.[89]

As shown in Figure 1.09a Song and co-workers synthesized a series of mixed halide nanocrystals from plate-type $MAPbBr_3$ nanocrystals.[84] They produced $MAPbBr_{3-x}Cl_x$ or $MAPbBr_{3-x}I_x$ nanocrystals by treating the as-grown $MAPbBr_3$ NCs with MACl and MAI precursor solutions and achieved a full range bandgap tuning from 1.6 to 3.0 eV. Manna and co-workers reported fast halide exchange reaction of colloidal $CsPbX_3$ NCs by using the halide salts as a source of anions.[85] Also, Nedulcu et al.[61] demonstrated the

compositional fine-tuning of highly luminescent $CsPbX_3$ nanocrystals through an anion exchange reaction by mixing the specific ratio of the desired halide source and $CsPbX_3$ NCs. Furthermore, as shown in Figure 1.09b, Karimata et al.[86] demonstrated the halide exchange reaction of a single $MAPbBr_3$ crystal upon immersing the crystals in an MAI reaction solution. The initial green emissive $MAPbBr_3$ single crystal changed its emission color in the whole area for 90 seconds. They observed the progress of the exchange reaction from $MAPbBr_3$ to $MAPbBr_{3-x}I_x$ using single-particle PL imaging and revealed the carrier dynamics during the reaction. Also, the thickness-dependent halide exchange reaction of $CsPbBr_3$ single crystals was studied by Zhang et al.[87] The micrometer-sized $CsPbBr_3$ nanoplates undergo halide exchange reaction in the vapor phase where the iodide vapor changed the initial $CsPbBr_3$ into $CsPbI_3$ because of the rapid halide exchange reaction. They revealed the kinetics of anion exchange reaction from the edges to the center of $CsPbBr_3$ crystals with different thicknesses, which proceeded through halide vacancy-assisted diffusion mechanism.

Another interesting feature of the halide exchange reaction is the perovskite heterostructure that can be created through a precisely controlled halide exchange reaction (Figure 1.09c). The spatially controlled halide exchange reaction can be induced at specific positions, and the bandgap is tuned. For instance, Son and co-workers[88] demonstrated a photoinduced halide exchange reaction in the absence of any reacting anion source. The photoinduced electron transfer from $CsPbX_3$ NCs to a halogenated solvent induces the spatial exchange reaction. They also demonstrated patterning of $CsPbBr_3$ in a thin fluorescent film of $CsPbCl_3$ NCs by partially irradiating them. Yang and co-workers reported precisely controlled anion exchange in single-crystalline $CsPbX_3$ perovskites by using a nanofabrication technique.[89] A spatially resolved exchange reaction was induced in a specific uncovered area by dipping the crystals into a halide precursor solution. The other parts of the crystals were masked with a thin layer of poly (methyl methacrylate) to avoid the halide exchange reaction.

1.4.4 Defects in halide perovskites

The cost-effective, simple synthesis process of halide perovskites made them promising for next-generation optoelectronic devices. Despite being defect tolerant, the formation of defects during the solution-processed fabrication limits their application in terms of power conversion efficiency and long-term stability. Because of the fast crystal growth process, a large number of defects are present in these materials. The soft lattice structure of

perovskite crystals undergoes imperfect lattice alignment from its ideal structure and induces defects. The non-stoichiometric precursor ratio and purity of the precursor salts also influence the crystal quality.[90,91] Moreover, the low lattice energies and the presence of organic contents also facilitates defect formation when the crystals are exposed to moisture, oxygen, or light.

The defects in semiconductors are mainly classified as point defects, Schottky and Frenkel defects, dislocations, and grain boundaries[92-96] (Figure 1.10). The point defects in halide perovskites are namely vacancy defects V_A, V_B, V_X; interstitial defects A_i, B_i, X_i; and antisites A_B, A_X, B_A, B_X, I_A, I_B.[92] The types of defects in perovskite materials are determined either by the formation energy or the position of the defect energy levels.

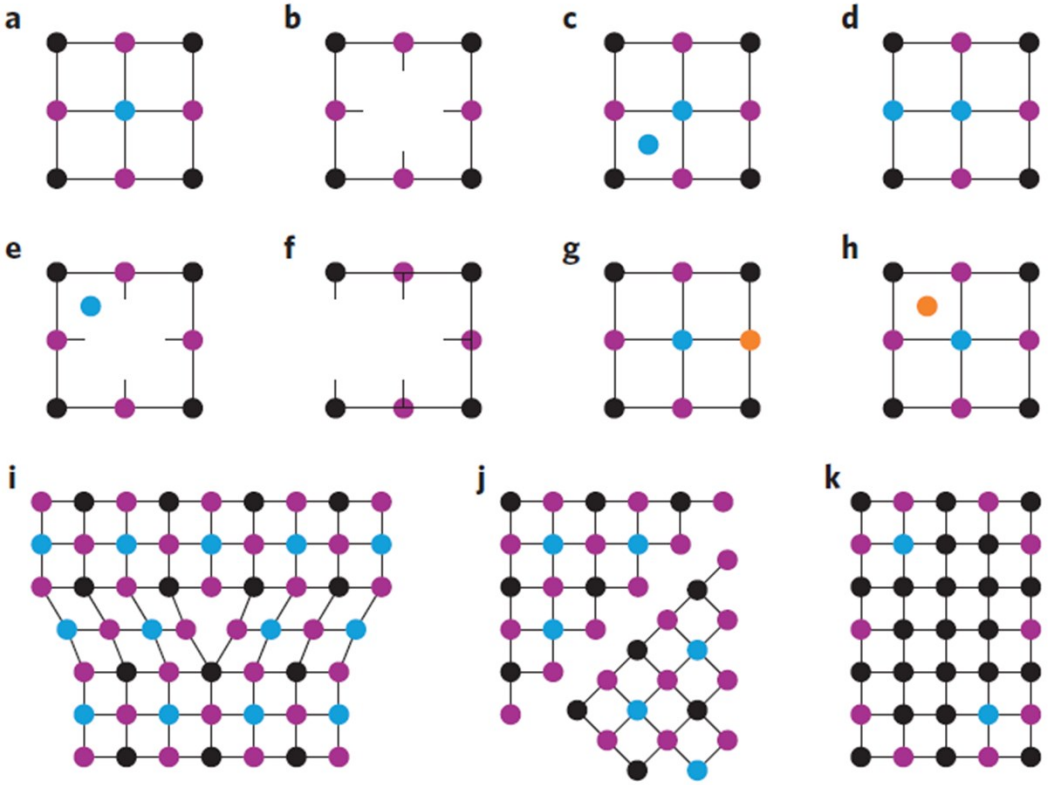

Figure 1.10: (a) An ideal perovskite crystal structure without defects, (b-k) types of possible defects in perovskites. (b-d) point defects, (e-h) Schottky and Frenkel defects, (i-k) higher dimensional defects. Reproduced from Ball et al.[101]

The first principle theoretical calculation reveals the formation energy of defects in perovskite semiconductors.[97] Furthermore, depending on the positions in the band edge, the defects can be classified as shallow-level traps or deep-level traps. The point defects, close to the VBM or CBM in the energy levels are called shallow defects and can be easily

detrapped and release the charges to band edges.[98] On the other hand, the deep traps are located in the middle of the forbidden band and cannot detrap easily. In general, the halide vacancy (Vi) and its complexes are responsible for the deep traps that act as the nonradiative recombination center. The point defects can also exhibit array configuration, which are commonly known as Schottky and Frenkel defects. Schottky defects are the anion and cation vacancies coexist in the same crystal, while the Frenkel defects are generated by ion vacancies from the same pair of ions.[93] Besides these, the 1-dimensional dislocation defects and 2-dimensional grain boundary defects are common types of defects in perovskites originated from the crystal discontinuation and difference in the crystal orientation.[99,100] Regardless of the types of defects, all of them induces unavoidable charge recombination center and trap the free charges, which eventually reduce the carrier mobility, carrier lifetime, and diffusion length. Thus, passivation of the defects is mandatory to achieve the theoretical limit of power conversion efficiency from perovskite-based photovoltaic and optoelectronic devices.

1.5 Optical trapping

The foundation of laser-based optical trapping was developed by Arthur Ashkin in the 1970s.[34] In the beginning, he demonstrated the movement of micron-sized dielectric particles in both air and water under laser irradiation and utilized the laser beam to trap the particles based on the counter propagation of two laser beams. Later he extended the trapping experiments to manipulate living cells like viruses and bacteria and for trapping and cooling of neutral atoms.[102,103] Since then, laser trapping or optical tweezers are being used as a versatile tool in chemistry and biological research. The various targets such as nanoparticles, polymers, proteins, and amino acids are trapped at the focal volume using the laser trapping technique.[35,36] In this section, I discussed the basic principle of laser trapping in brief.

When a laser beam is tightly focused on a dielectric particle, it experiences a force near the focal point due to the transfer of momentum from the incident photons. The resulting force generated by the incident photons can be classified as scattering force and gradient force. The scattering force is proportional to the incident light intensity and acts in the direction of incident light while the gradient force is proportional to the gradient of intensity and acts along the intensity gradient.[104] A general scheme for the generation of the stable, the scattering, and the gradient optical force is shown in Figure 1.11. When the particle

with radius *a* is larger than the trapping laser wavelength, λ, i.e., a >> λ, the Mie scattering conditions are satisfied, and both the forces can be calculated by geometrical ray-optics model.[105] As illustrated in Figure 1.11a, for a homogeneous electric field, the incident light is readily reflected and absorbed by the particle, which

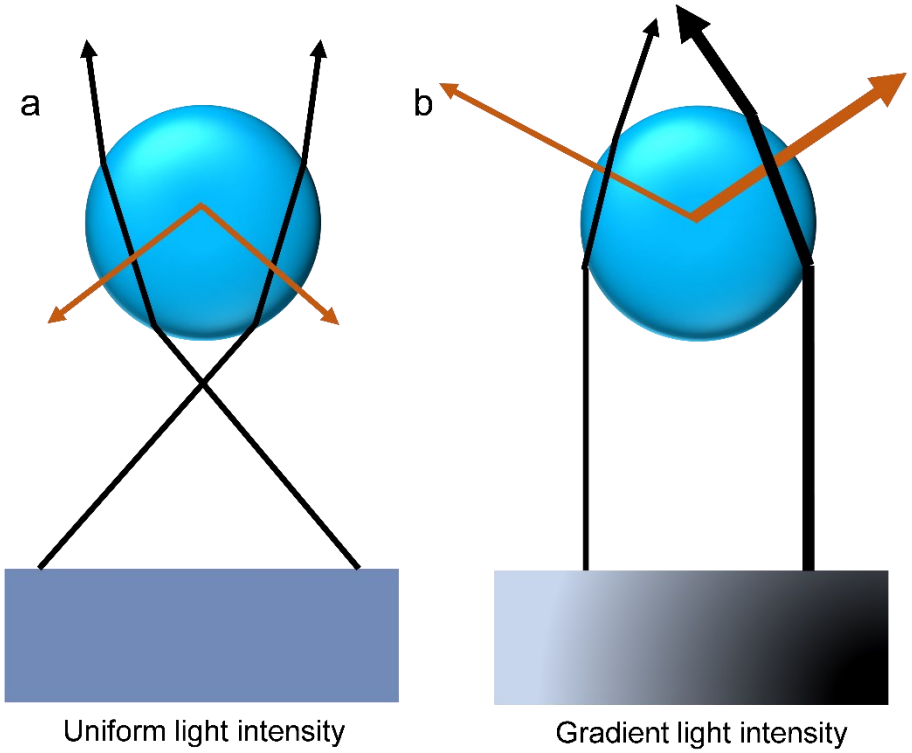

Figure 1.11: A schematic illustration for the generation of (a) a stable optical force by uniform light intensity and (b) the scattering and the gradient optical force due to the intensity gradient

arises the scattering component, and the scattering force is calculated from the optical momentum transfer. On the other hand, for an inhomogeneous electric field, the incident light undergoes refraction, and the change in momentum of the particle is considered according to the gradient force. In an optical trapping system, the Gaussian intensity profile beam of laser induces fluctuating dipoles in the particle, and the interaction of these dipoles with the inhomogeneous electric field at the focus results in the gradient trapping force (Figure 1.11b). To utilize stable trapping the trapping force that is pulling the particle towards the focal region must exceed the scattering force. In another case, when the radius *a* of the particle is smaller than the laser wavelength λ, i.e., a << λ, the conditions for Rayleigh scattering are satisfied, and the particle is considered as a point dipole to calculate the optical force.[105] Under this condition, the scattering force is expressed as,

$$F_{scat} = \frac{I_o \sigma n_m}{c}$$

where,

$$\sigma = \frac{128\pi^5 a^6}{3\lambda^4}\left(\frac{m^2-1}{m^2+2}\right)^2$$

Here, I_o is the light intensity, σ denotes scattering cross-section, n_m is the refractive index of the medium, m is the refractive index contrast ($m = n_s/n_m$), n_s is the refractive index of the surroundings, and λ is the wavelength of laser. Again, for an inhomogeneous electric field, the gradient force arises from the dipoles is termed as,

$$F_{grad} = \frac{2\pi\alpha}{cn_m{}^2}\nabla I_o$$

Where,

$$\alpha = n_m{}^2 a^3 \left(\frac{m^2-1}{m^2+2}\right)$$

Here, α denotes the particle polarizability, c is the speed of light in the vacuum. A higher refractive index of the particle than the surrounding medium allows the forces to act on the particle and bring it towards the higher light intensity region. As a result, the particle is trapped at the focus point where the laser intensity is maximum.

1.6 Applications of lead halide perovskites

1.6.1 Solar cells:

Perovskite-based solar cells (PSC) have received enormous attention in recent years because of their superior optoelectronic properties, such as high absorption coefficient, slow carrier recombination, long carrier diffusion length, and unusually high defect tolerance. A radical change in solar cell architecture has been achieved since Kojima et al.[12] fabricated the PSC with 3.8 % power conversion efficiency in 2009. In general, the structure of PSCs can be classified as a n-i-p-i type or a p-i-n-i type junction. In both structures, the perovskite layer is sandwiched between the hole transporting layer (HTL) and electron transporting layer (ETL) to improve the charge extraction and transport characteristics. The HTL is contacted to fluorine-doped tin oxide (FTO) or indium tin oxide (ITO), while the HTL is contacted to a counter electrode like Au, Ag, and Cu, etc. Finally, the outer layers are connected to an external load. Figure 1.12a. Shows a model structure of a solar cell based on $MAPbI_3$ perovskite crystals. Upon irradiation, the perovskite absorption layer generates electron and hole charge carriers which are extracted by the

charge transport layers HTL or ETL. Thus, the adoption of a suitable charge transport layer plays a crucial role in determining the performance of PSC. Various ETLs such as TiO_2, SnO_2, and ZnO and HTLs such as 2,20,7,70-tetrakis-(N, N-dimethoxyphenylamino)-9,90-spirobifluorene (spiro-MeOTAD), poly(triarylamine) [PTTA], poly(3,4 ethylene dioxythiophene)-polystyrene sulfonate (PEDOT;PSS) are commonly used to achieve high efficiency and stable PSCs. (Figure 1.12b).

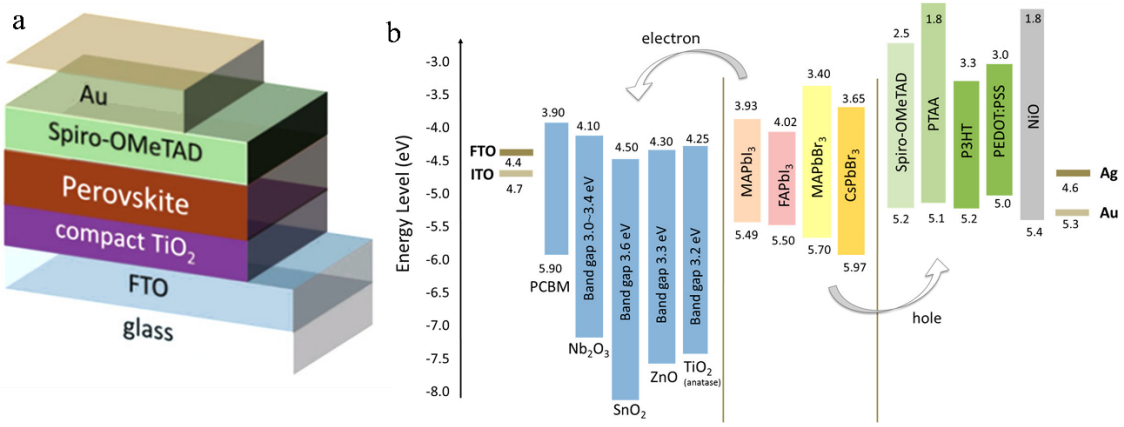

Figure 1.12: (a) Device architecture of a solar cell fabricated by using $MAPbI_3$ single crystal, (b) Energy levels of various commonly used perovskite materials, HTLs and ETLs in solar cells. Adopted from Jena et al.[116]

For an energetically stable PSC, the lowest unoccupied molecular orbital of the ETL should be lower than CBM and the highest occupied molecular orbital should be higher than VBM.

Besides the charge transporting layers, the most fundamental and critical factor for high-efficiency PSC is the crystal quality. The defects in perovskite thin films or single crystals can induce shallow or deep charge traps, which lead to the decrease in carrier lifetime and mobility. Considering these defects, detailed studies have been employed to passivate the perovskite layers of PSCs through controlled deposition and crystal growth mechanisms.[106,107] Also, different compositional engineering by altering the stoichiometric ratio and post-synthetic chemical treatments by Lewis acids and bases, cations, and anions are reported to enhance the efficiency of PSCs.[108-110] Along with the intrinsic crystal properties, the stability of the perovskite layers is also significantly affected by several external factors such as moisture, oxygen, heat, and light. Several encapsulation strategies, such as treating the perovskites with additives, coating with large cations or polymers, and modifying the composition with mixed halides, are employed to improve the performance of PSCs.[22,111-113] For instance, Chaudhary et al.[113] adopted an ultra-thin layer of polyvinyl

pyridine to coat the $MAPbI_3$ perovskite surface, which improves the water-resistance of $MAPbI_3$ when immersed in water. Despite of these limitations, the power conversion efficiency of PSCs has reached to 26.5% in a single junction and 29.5% in a perovskite/Si multi-junction perovskite solar cell.[114]

1.6.2 Perovskite light-emitting diodes (PeLEDs)

Owing to the high color purity, narrow emission band, and high photoluminescence quantum yield (PLQY) perovskite materials find their application in LEDs. Similar to the solar cell structure, PeLEDs structure also consists of an anode, an HTL, a perovskite layer, an ETL and a cathode. Figure 1.13a shows the device architecture for a PeLED using $CsPbBr_3$ perovskite nanocrystals. The HTLs efficiently transport the holes, and the ETLs are adopted to transport the electrons and prevent holes at the interface. When an external voltage is applied, electrons and holes transport from the cathode and anode, respectively. The excitons are generated and consequently recombine radiatively to release energy as light or nonradiatively by releasing heat. For example, as shown in Figure 1.13b, a green-emitting PeLED was prepared by Ling et al.[16] using $MAPbBr_3$ nanosheets as emitting materials, which exhibit high color purity with bright green electroluminescence centered at 530 nm with full width half maximum of 20 nm and 85% PLQY at 7 V. However, the efficiency of PeLEDs is intensely affected by the leakage currents resulting from the pinholes of thin films as well as the presence of excess metallic Pb atoms.[118,119] These shortcomings can be resolved by blending the perovskites with suitable polymers and treating the surface with excess precursor salts.[119,120]

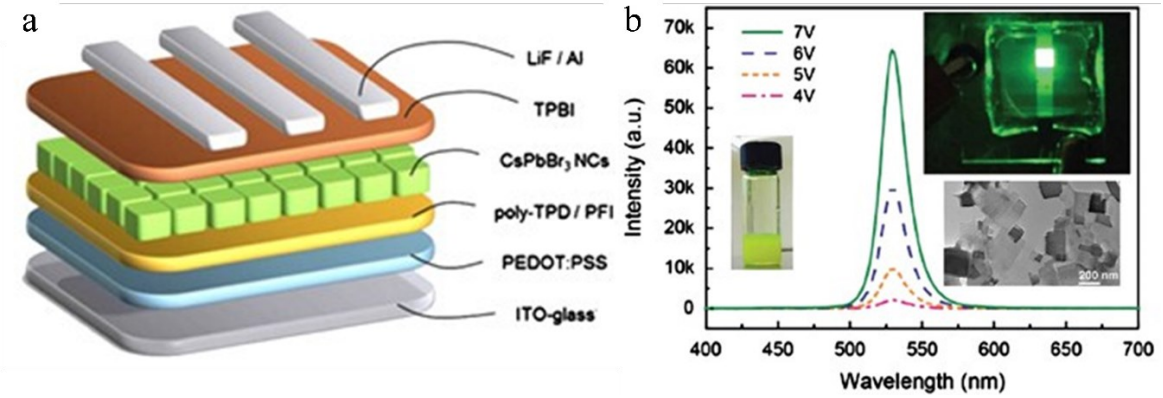

Figure 1.13: (a) A scheme for the device fabrication of PeLED, (b) A perovskite-based LED showing emission and electroluminescence spectrum at different applied voltages. Reproduced from (a) Huang et al.[117] (b)Ling et al.[16]

For example, a reduction in leakage current and trap passivation of $CsPbBr_3$ using a MABr layer was reported by Lin et al.[118] with a high external quantum efficiency of 20%. Besides these, manipulating the crystallization process, using low dimensional perovskites and tuning the precursor ratios to create multiple quantum well can also accelerate the efficiency of PeLEDs.[121,122] The chemical and structural stability of perovskites are also affected by external factors such as moisture, air, and heating. Using all inorganic Cs-based perovskite instead of MA-based perovskites have shown improved stability.[123] Also, mixed cation composition and layered perovskite structures are other ways to improve the LED stability.[124]

1.6.3 Lasers

Low temperature, solution-processed perovskite materials possess high crystallinity with slow nonradiative decay making them highly potential in lasing applications. The perovskite materials can easily achieve the population inversion, which is mandatory to act as a gain medium in lasers. Since the demonstration of amplified spontaneous emission ASE) by Xing et al.[17] from $MAPbX_3$ thin films, various dimensions of perovskites, such as quantum dots, cuboids, platelets, and wires or rods have been introduced to gain lasing from these materials. Also, the perovskite materials are placed in different types of cavities such as random cavities, Fabry-Perot cavities and whispering gallery mode (WGM) cavities to achieve low lasing threshold power.[125-127] Beyond the minimum threshold, the emission intensity increases sharply with redshifted, and ultranarrow peak, characteristic of multimode or single-mode lasing. For instance, solution processed $MAPbX_3$ nanowires were prepared by Zhu et al.[128] which exhibited low lasing thresholds at 200 nJ/cm^{-2} with a high Q-factor of 3600 and tuneable wavelength over the whole visible wavelengths (Figure 1.14).

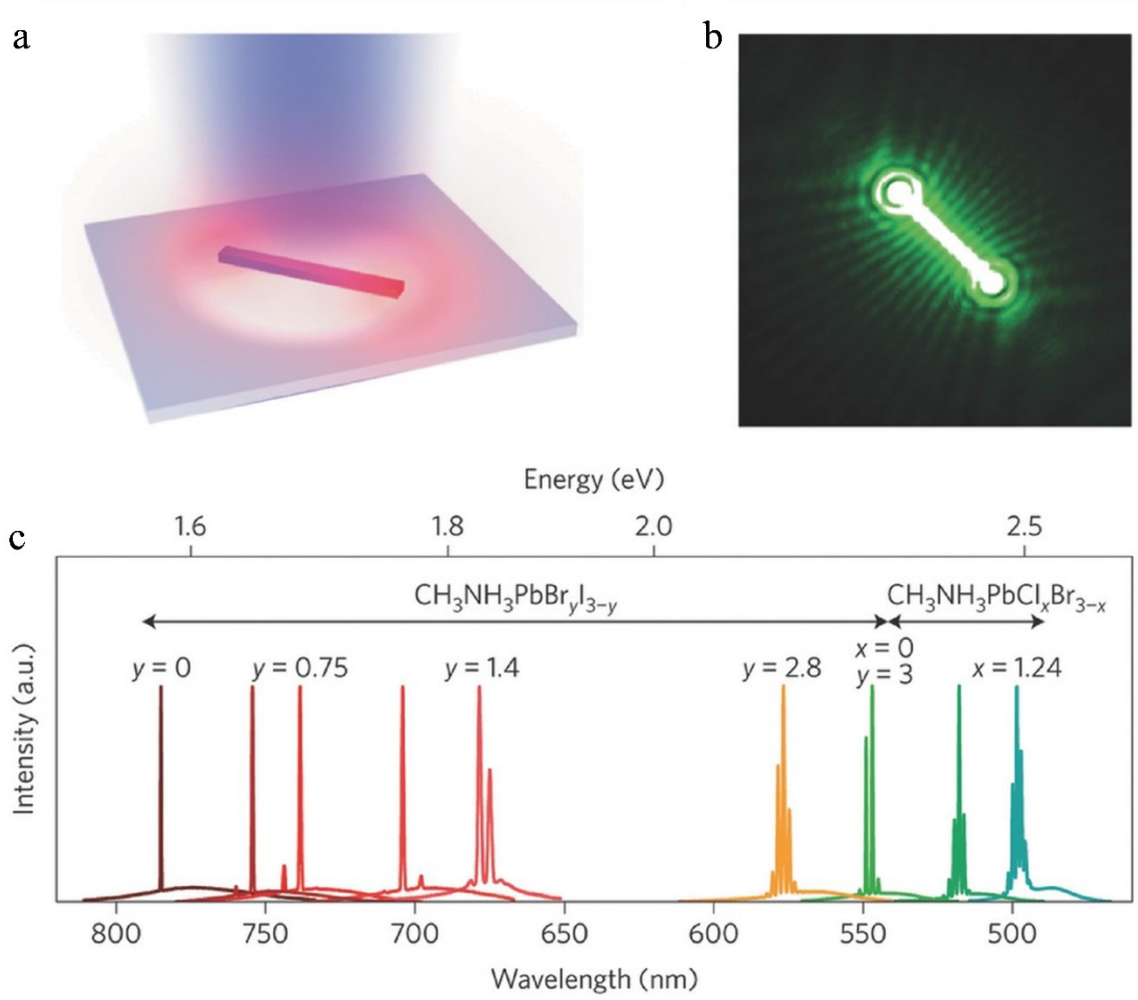

Figure1.14: (a) A scheme of a $MAPbX_3$ nanowire under laser excitation, (b) amplified emission from the nanowire over lasing threshold, and (c) lasing emission spectra from MA-based mixed halide composition. Reproduced from Zhu et al.[128]

(Also, the WGM cavities were found in $MAPbI_3$ nanoplatelets with a lasing threshold of 37 $\mu J/cm^{-2}$.[129] However, the lasing threshold in various cavities hugely depends on the size, shape, halide composition, and crystal quality. Thus, considering these factors during the crystal growth is also essential to achieve desired lasing from the perovskite materials.

1.7 Research motivation and objectives

Lead halide perovskites are being extensively studied due to their low-cost fabrication and superior optoelectronic properties. These materials are expected to be one of the most promising semiconducting materials for next-generation photovoltaic devices. The optoelectronic properties of perovskite materials can be easily tuned by post-synthetic halide exchange reaction. Moreover, the fast solution-processed crystal growth process also creates many defects in these materials, especially cation and anion vacancies. On the other

hand, recently our group has demonstrated the crystallization of halide perovskites by laser trapping. In this process, the crystallization of perovskite crystal was induced at the focal volume of the trapping laser by tightly focusing it. The new laser trapping-based crystallization approach motivated me to further explore the laser trapping potentials to modify perovskite crystals in terms of halide exchange reaction, vacancy filling, and controlling the charge carrier dynamics. Thus, the thesis aims to induce the halide exchange reaction at the desired positions and tune the emission color and bandgap of perovskite microcrystals and nanocrystal films. Moreover, in this research, the laser trapping tool is further utilized to fill the vacancies of the as-grown lead halide crystals to control the charge carrier dynamics. Thus, this study offers innovative laser-based site-specific reaction for spatially-resolved bandgap tuning, halide vacancy filling, and controlling of the properties of perovskite by fabricating heterojunctions.

1.8 References

1. Chakhmouradian A. R.; Woodward P. M. Celebrating 175 Years of Perovskite Research A Tribute to Roger H. Mitchell. *Phys. Chem. Miner.* **2014**, *41*, 387−391.

2. Wells H. L., Über die Cäsium- und Kalium-Bleihalogenide. *Zeitschrift für anorganische Chemie* **1893**, *3*, 195−210.

3. Dong Q.; Fang Y.; Shao Y.; Mulligan P.; Qiu J.; Cao L.; Huang J. Solar Cells. Electron-Hole Diffusion Lengths > 175μm in Solution-Grown $CH_3NH_3PbI_3$ Single Crystals. *Science* **2015**, *347*, 967−970.

4. Jeng J−Y.; Chiang Y.−F., Lee M.−H., Peng S.−R., Guo T.−F., Chen P., Wen T.−C., $CH_3NH_3PbI_3$ Perovskite/Fullerene Planar-Heterojunction Hybrid Solar Cells. *Adv. Mater.* **2013,** *25*, 3727−3732.

5. Kojima A., Ikegami M., Teshima K., Miyasaka, T. Highly Luminescent Lead Bromide Perovskite Nanoparticles Synthesized with Porous Alumina Media. *Chem. Lett.* **2012**, *41*, 397−399.

6. Lee M. M., Teuscher J., Miyasaka T., Murakami T. N., Snaith H. J., Efficient Hybrid Solar Cells Based on Meso-Superstructured Organometal Halide Perovskites. *Science* **2012,** *338*, 643−650.

7. Stranks S. D., Eperon G. E., Grancini G., Menelaou C., Alcocer M. J. P., Leijtens T., Herz L. M., Petrozza A., Snaith H. J. Electron-Hole Diffusion Lengths Exceeding 1 Micrometer in an Organometal Trihalide Perovskite Absorber. *Science* **2013**, *342*, 341−345.

8. Xing G., Mathews N., Sun S., Lim S. S., Lam Y. M., Grätzel M., Mhaisalkar S., Sum T. C. Long-Range Balanced Electron- and Hole-Transport Lengths in Organic-Inorganic $CH_3NH_3PbI_3$. *Science* **2013**, *342*, 344−347.

9. Juarez-Perez E. J., Sanchez R. S., Badia L., Garcia-Belmonte G., Kang Y. S., Mora-Sero I., Bisquert J. Photoinduced Giant Dielectric Constant in Lead Halide Perovskite Solar Cells. *J. Phys. Chem. Lett*. **2014**, *5*, 2390−2394.

10. Ming W., Shi H., Du M.−H. Large Dielectric Constant, High Acceptor Density, and Deep Electron Traps in Perovskite Solar Cell Material $CsGeI_3$. *J. Mater. Chem. A* **2016**, *4*, 13852−13858.

11. Galkowski K., Mitioglu A., Miyata A., Plochocka P., Portugall O., Eperon G. E., Wang J. W., Stergiopoulos T., Stranks S. D., Snaith H. J., Nicholas R. J. Determination of the Exciton Binding Energy and Effective Masses for Methylammonium and Formamidinium Lead Tri-halide Perovskite Semiconductors. *Energy Environ. Sci.* **2016**, *9*, 962−970.

12. Kojima A., Teshima K., Shirai Y., Miyasaka T., Organometal halide perovskites as visible-light sensitizers for photovoltaic cells *J. Am. Chem. Soc*., **2009**, *131*, 6050–6051.

13. Kim H. S., Lee, C. R.; Im, J. H.; Lee, K. B.; Moehl, T.; Marchioro, A.; Moon, S. J.; Humphry-Baker, R.; Yum, J. H.; Moser, J. E.; Gratzel, M.; Park, N. G. Lead Iodide Perovskite Sensitized All-Solid-State Submicron Thin Film Mesoscopic Solar Cell with Efficiency Exceeding 9%. *Sci. Rep.* **2012,** *2,* 591−597.

14. Singh, S. P.; Nagarjuna, P. Organometal Halide Perovskites as Useful Materials in Sensitized Solar Cells. *Dalton Trans*. **2014**, *43*, 5247−5251

15. Tan, Z. − K.; Moghaddam, R. S.; Lai, M. L.; Docampo, P.; Higler, R.; Deschler, F.; Price, M.; Sadhanala, A.; Pazos, L. M.; Credgington, D. Bright Light-Emitting Diodes Based on Organometal Halide Perovskite. *Nat. Nanotechnol*. **2014,** *9*, 687−692

16. Ling Y., Yuan Z., Tian Y., Wang X., Wang J. C., Xin Y., Hanson K., Ma B., Gao H. Bright light-emitting diodes based on organometal halide perovskite nanoplatelets *Adv. Mater.* **2016**, *28*, 305–311

17. Xing, G.; Mathews, N.; Lim, S. S.; Yantara, N.; Liu, X.; Sabba, D.; Grätzel, M.; Mhaisalkar, S.; Sum, T. C. Low-Temperature Solution-Processed Wavelength-Tunable Perovskites for Lasing. *Nat. Mater*. **2014**, *13*, 476−480.

18. Fu, Y.; Zhu, H.; Schrader, A. W.; Liang, D.; Ding, Q.; Joshi, P.; Hwang, L.; Zhu, X. Y.; Jin, S. Nanowire Lasers of Formamidinium Lead Halide Perovskites and Their Stabilized Alloys with Improved Stability. *Nano Lett.* **2016**, *16*, 1000−1008.

19. Lian, Z.; Yan, Q.; Lv, Q.; Wang, Y.; Liu, L.; Zhang, L.; Pan, S.; Li, Q.; Wang, L.; Sun, J. − L. High-Performance Planar-Type Photodetector on (100) Facet of $MAPbI_3$ Single Crystal. *Sci. Rep*. **2015**, *5*, 16563−16573.

20. Mitzi D. B., Synthesis, Structure, and Properties of Organic– Inorganic Perovskites and Related Materials, *Progress in Inorganic Chemistry*, **2007**, 1–121

21. Park N.-G., Perovskite solar cells: an emerging photovoltaic technology *Mater. Today,* **2015**, *18*, 65–72.

22. Li Z., Yang M., Park J.-S., Wei S.-H., Berry J. J. and Zhu K., Stabilizing Perovskite Structures by Tuning Tolerance Factor: Formation of Formamidinium and Cesium Lead Iodide Solid-State Alloys *Chem. Mater*., **2015**, *28*, 284–292

23. Travis W., Glover E., Bronstein H., Scanlon D, Palgrave R., On the application of the tolerance factor to inorganic and hybrid halide perovskites: a revised system *Chem. Sci.*, **2016**, *7*, 4548–4556.

24. E. L. Da Silva, J. M. Skelton, S. C. Parker and A. Walsh, Phase stability and transformations in the halide perovskite $CsSnI_3$ *Phys. Rev. B*., **2015**, *91*, 144107.

25. Wang Q., Dong Q., Li T., Gruverman A., Huang J., Thin insulating tunneling contacts for efficient and water resistant perovskite solar cells, *Adv. Mater*., **2016**, *28*, 6734–6739.

26. A. Poglitsch, D. Weber, Dynamic disorder in methylammoniumtrihalogenoplumbates (II) observed by millimeter-wave spectroscopy *J. Chem. Phys.* **1987**, *87,* 6373.

27. Y. Dang, Y. Liu, Y. Sun, D. Yuan, X. Liu, W. Lu, G. Liu, H. Xia, X. Tao Bulk crystal growth of hybrid perovskite material $CH_3NH_3PbI_3$. *CrystEngComm* **2015**, *17*, 665–670

28. M. I. Saidaminov, A. L. Abdelhady, B. Murali, E. Alarousu, V. M. Burlakov, W. Peng, I. Dursun, L. Wang, Y. He, G. Maculan, A. Goriely, T. Wu, O. F. Mohammed and O. M. Bakr High-quality bulk hybrid perovskite single crystals within minutes by inverse temperature crystallization *Nat. Commun*, **2015,** *6*, 7586.

29. G. Maculan, A. D. Sheikh, A. L. Abdelhady, M. I. Saidaminov, M. A. Haque, B. Murali, E. Alarousu, O. F. Mohammed, T. Wu and O. M. Bakr, $CH_3NH_3PbCl_3$ Single Crystals: Inverse Temperature Crystallization and Visible-Blind UV-Photodetector J. *Phys. Chem. Lett.*, **2015**, *6*, 3781.

30. M. I. Saidaminov, A. L. Abdelhady, G. Maculan, O. M. Bakr Retrograde solubility of formamidinium and methylammonium lead halide perovskites enabling rapid single crystal growth *Chem. Commun*., **2015**, *51*, 17658.

31. Y. Liu, Z. Yang, D. Cui, X. Ren, J. Sun, X. Liu, J. Zhang, Q. Wei, H. Fan, F. Yu, X. Zhang, C. Zhao, S. F. Liu Two-Inch-Sized Perovskite $CH_3NH_3PbX_3$ (X = Cl, Br, I) Crystals: Growth and Characterization *Adv. Mater*., **2015**, *27*, 5176.

32. Q. Han, S.-H. Bae, P. Sun, Y.-T. Hsieh, Y. M. Yang, Y. S. Rim, H. Zhao, Q. Chen, W. Shi, G. Li and Y. Yang, Single Crystal Formamidinium Lead Iodide ($FAPbI_3$): Insight into the Structural, Optical, and Electrical Properties *Adv. Mater*., **2016**, *28*, 2253.

33. D. Shi, V. Adinolfi, R. Comin, M. Yuan, E. Alarousu, A. Buin, Y. Chen, S. Hoogland, A. Rothenberger, K. Katsiev, Y. Losovyj, X. Zhang, P. A. Dowben, O. F. Mohammed, E. H. Sargent and O. M. Bakr Low trap-state density and long carrier diffusion in organolead trihalide perovskite single crystals *Science*, **2015**, *347*, 519

34. A. Ashkin, J. M. Dziedzic, J. E. Bjorkholm, S. Chu Observation of a Single-Beam Gradient Force Optical Trap for Dielectric Particles. *Opt. Lett.* **1986**, *11*, 288−290.

35. S. Ito, H. Yoshikawa, H. Masuhara Optical Patterning and Photochemical Fixation of Polymer Nanoparticles on Glass Substrates. *Appl. Phys. Lett*. **2001**, *78*, 2566−2568.

36. M. J. Guffey, N. F. Scherer All-Optical Patterning of Au Nanoparticles on Surfaces Using Optical Traps. *Nano Lett.* **2010**, *10*, 4302−4308.

37. K.-i. Yuyama, M. J. Islam, K. Takahashi, T. Nakamura, V. Biju Crystallization of Methylammonium Lead Halide Perovskites by Optical Trapping. *Angew. Chem*. **2018**, *130*, 13612−13616.

38. M.J. Islam, K.-i. Yuyama, K. Takahashi, V. Biju Mixed-halide perovskite synthesis by chemical reaction and crystal nucleation under an optical potential. *NPG Asia Mater* **2019**

39. L. Protesescu, S. Yakunin, M.I. Bodnarchuk, F. Krieg, R. Caputo, C.H. Hendon, R.X. Yang, A. Walsh, M.V. Kovalenko Nanocrystals of Cesium Lead Halide Perovskites ($CsPbX_3$, X = Cl, Br, and I): Novel Optoelectronic Materials Showing Bright Emission with Wide Color Gamut. *Nano Lett*. **2015**, *15*, 3692–3696.

40. F. Zhang, H. Zhong, C. Chen, X.-G. Wu, X. Hu, H. Huang, J. Han, B. Zou, Y. Dong Brightly Luminescent and Color-Tunable Colloidal $CH_3NH_3PbX_3$ (X = Br, I, Cl) Quantum Dots: Potential Alternatives for Display Technology. *ACS Nano* **2015**, *9*, 4533–4542.

41. N. J. Jeon, H. Na, E. H. Jung, T.-Y. Yang, Y. G. Lee, G. Kim, H.-W. Shin, S. I. Seok, J. Lee, J. Seo A Fluorene-Terminated Hole-Transporting Material for Highly Efficient and Stable Perovskite Solar Cells. *Nat. Energy* **2018**, *3*, 682−689.

42. F. Huang, Y. Dkhissi, W. Huang, M. Xiao, I. Benesperi, S. Rubanov, Y. Zhu, X. Lin, Jiang, L. Y. Zhou Gas-Assisted Preparation of Lead Iodide Perovskite Films Consisting of a Monolayer of Single Crystalline Grains for High Efficiency Planar Solar Cells. *Nano Energy* **2014**, *10*, 10−18.

43. A. Mei, X. Li, L. Liu, Z. Ku, T. Liu, Y. Rong, M. Xu, M. Hu, J. Chen, Y. Yang, A Hole-Conductor-Free, Fully Printable Mesoscopic Perovskite Solar Cell with High Stability. *Science* **2014**, *345*, 295−298.

44. K. Liang, D. B. Mitzi, M. T. Prikas Synthesis and Characterization of Organic-Inorganic Perovskite Thin Films Prepared Using a Versatile Two-Step Dipping Technique. *Chem. Mater.* **1998**, *10*, 403−411.

45. D. Vak, K. Hwang, A. Faulks, Y.-S. Jung, N. Clark, D.-Y. Kim, G. J. Wilson, S. E. Watkins 3D Printer Based Slot-Die Coater as a Lab-to-Fab Translation Tool for Solution-Processed Solar Cells. *Adv. Energy Mater*. **2015**, *5*, 1401539.

46. J. H. Heo, M. H. Lee, M. H. Jang, S. H. Im Highly efficient $CH_3NH_3PbI_{3-x}Cl_x$ Mixed Halide Perovskite Solar Cells Prepared by Re-dissolution and Crystal Grain Growth via Spray Coating. *J. Mater. Chem*. A **2016**, *4*, 17636−17642.

47. X. Peng, J. Yuan, S. Shen, M. Gao, A. S. R. Chesman, H. Yin, J. Cheng, Q. Zhang, D. Angmo Perovskite and Organic Solar Cells Fabricated by Inkjet Printing: Progress and Prospects. *Adv. Funct. Mater***. 2017**, *27*, 1703704.

48. Y. Guo, X. Yin, J. Liua, W. Que Highly efficient CsPbIBr2 perovskite solar cells with efficiency over 9.8% fabricated using a preheating assisted spin-coating method. J Mater Chem A, 2019, 7: 19008–19016.

49. J-H. Im, I-H. Jang, N. Pellet, M. Grätzel, N-G. Park Growth of $CH_3NH_3PbI_3$ cuboids with controlled size for high-efficiency perovskite solar cells. Nat Nanotech, 2014, 9: 927–932.

50. Shamsi J., Abdelhady A. L., Accornero S., Arciniegas M., Goldoni L., Kandada A. R.S., Petrozza A., Manna L. N-Methylformamide as a Source of Methylammonium Ions in the Synthesis of Lead Halide Perovskite Nanocrystals and Bulk Crystals *ACS Energy Lett.* **2016**, 1, 1042-1048.

51. W. Nie, H. Tsai, R. Asadpour, J.-C. Blancon, A. J. Neukirch, G. Gupta, J. J. Crochet, M. Chhowalla, S. Tretiak, M. A. Alam, H.-L. Wang, A. D. Mohite, High-efficiency solution-processed perovskite solar cells with millimeter-scale grains *Science* **2015**, *347*, 522.

52. Chen X., Wang Z., Investigating chemical and structural instabilities of lead halide perovskite induced by electron beam irradiation *Micron* **2019**, *116*, 73-79.

53 Zhang D., Zhu Y., Liu L., Ying X., Sougrat C.-E., Li K., Han Y., Atomic-resolution transmission electron microscopy of electron beam-sensitive crystalline materials *Science* **2018**, *1*, 675-679.

54. Eaton S. W., Lai M., Gibson N. A., Wong A. B., Dou L., Ma J., Wang L-W., Leone S. R., Yang P. Lasing in cesium lead halide perovskite nanowires *PNAS* **2016**, *113* 1993-1998.

55. Zhou N., Bekenstein Y., Eisler C. N., Zhang D., Schwartzberg A. M., Yang P., Alivisatos A. P., Lewis J. A. Perovskite nanowire–block copolymer composites with digitally programmable polarization anisotropy *Sci Adv*., **2019**, *31*, 8141.

56. Oliver R. A., Advances in AFM for the electrical characterization of semiconductors *Rep. Prog. Phys*. **2008**, *71*, 076501.

57. Im J.-H., Lee C.-R., Lee J.-W.,. Park S.-W, Park N.-G., 6.5% efficient perovskite quantum-dot-sensitized solar cell *Nanoscale,* **2011**, *3*, 4088-4093.

58. L. Peedikakkandy, P. Bhargava, Recrystallization and phase stability study of cesium tin iodide for application as a hole transporter in dye sensitized solar cells *Mater. Sci. Semicond. Process*. **2015,** *33*, 103-109.

59. Yang B., Mao X., Hong F., Meng W., Tang Y., Xia X., Yang S., Deng W., Han K., Lead-Free Direct Band Gap Double-Perovskite Nanocrystals with Bright Dual-Color Emission *J. Am. Chem. Soc.*, **2018**, *140*, 17001–17006.

60 Wang L., Williams N. E., Malachosky E. W., Otto J. P., Hayes D., Wood R. E., Guyot-Sionnest P., Engel G. S., *ACS Nano*, **2017**, *11*, 2689–2696.

61. Nedelcu G., Protesescu L., Yakunin S., Bodnarchuk M. I., Grotevent M. J., Kovalenko M. V. Fast anion-exchange in highly luminescent nanocrystals of cesium lead halide perovskites ($CsPbX_3$, X = Cl, Br, I). *Nano Letters* **2015**, 15, 5635–5640.

62. Huang L.,W. R. L. Lambrecht, Electronic band structure, phonons, and exciton binding energies of halide perovskites $CsSnCl_3$, $CsSnBr_3$, and $CsSnI_3$ *Phys. Rev. B: Condens. Matter Mater. Phys.*, **2013**, *88*, 165203.

62. Dong Y., Qiao T., Kim D., Parobek D., Rossi D., Son D. H., Precise Control of Quantum Confinement in Cesium Lead Halide Perovskite Quantum Dots via Thermodynamic Equilibrium Nano Lett., 2018, 18, 3716–3722.

63. Zhang D., Yu Y., Bekenstein Y., Wong A. B., Alivisatos A. P., Yang P., Synthesis of Composition Tunable and Highly Luminescent Cesium Lead Halide Nanowires through Anion-Exchange Reactions *J. Am. Chem. Soc*., **2016**, *138*, 13155–13158.

64. Tajima M., Characterization of semiconductors by photoluminescence mapping at room temperature *J. Cryst. Growth* **1990**, *103*, 1.

65. Vallikkodi M., Synthesis, Growth and Characterization of Piperazinium P-Aminobenzoate and Piperazinium P-Chlorobenzoate Nonlinear Optical Single Crystals, Alagappa University, Karaikudi, India 2018.

66. H. Zhou, Q. Chen, G. Li, S. Luo, T. Song, H.-S. Duan, Z. Hong, J. You, Y. Liu, Y. Yang, Photovoltaics. Interface engineering of highly efficient perovskite solar cells *Science,* **2014**, *345*, 542lp.

67. 1. Zhenfu Z., Liang. J., Zhihai, Jiong C., Miaomiao Z., Yafei H. Perovskite quantum dots as fluorescent materials for multi-colored lighting. *J Mater Sci* **2018**, *53*, 15430–15441.

68. Saidaminov, M. I.; Haque, M. A.; Almutlaq, J.; Sarmah, S.; Miao, X. − H.; Begum, R.; Zhumekenov, A. A.; Dursun, I.; Cho, N.; Murali, B.; Mohammed, O. F.; Wu, T.; Bakr, O. M. Inorganic Lead Halide Perovskite Single Crystals: Phase-Selective Low-Temperature Growth, Carrier Transport Properties, and Self-Powered Photodetection. *Adv. Opt. Mater.* **2017**, *5*, 1600704.

70. Chen Y., Peng J., Su D., Chen X., Liang Z., Efficient and Balanced Charge Transport Revealed in Planar Perovskite Solar Cells *ACS Appl. Mater. Interfaces*, **2015**, *7*, 4471–4475.

71. Chin X. Y., Cortecchia D., Yin J., Bruno A., Soci C., Lead iodide perovskite light-emitting field-effect transistor *Nat. Commun*., **2015**, *6*, 7383.

72. Takahashi Y., Hasegawa H., Takahashi Y. and Inabe T.Hall mobility in tin iodide perovskite $CH_3NH_3SnI_3$: Evidence for a doped semiconductor, *J. Solid State Chem*., **2013**, *205*, 39–43.

73. Xiao Z., Bi C., Shao Y., Dong Q., Wang Q., Yuan Y., Wang C., Gao Y., Huang J., Efficient, high yield perovskite photovoltaic devices grown by interdiffusion of solution-processed precursor stacking layers *Energy Environ. Sci*., **2014**, *7*, 2619–2623.

74. Wei, H.; Fang, Y.; Mulligan, P.; Chuirazzi, W.; Fang, H.-H.; Wang, C.; Ecker, B. R.; Gao, Y.; Loi, M. A.; Cao, L.; Huang, J. Sensitive X-ray Detectors Made of Methylammonium Lead Tribromide Perovskite Single Crystals. Nat. Photonics 2016, 10, 333−339.

75. Johnston M. B., Herz L. M. Hybrid Perovskites for Photovoltaics: Charge-Carrier Recombination, Diffusion, and Radiative Efficiencies. *Acc. Chem. Res*. **2016,** *49*, 146−154.

76. Manser J. S., Kamat P. V. Band Filling with Free Charge Carriers in Organometal Halide Perovskites. *Nat. Photonics* **2014,** *8*, 737−743.

77. Li C., Wang A., Deng X., Wang S., Yuan Y., Ding L., Hao F.. Insights into Ultrafast Carrier Dynamics in Perovskite Thin Films and Solar Cells. *ACS Photonics* **2020**, *7*, 1893-1907.

78. Kim J. Y., Lee J-W., Jung H. S., Shin H., Park N.-G.. High-Efficiency Perovskite Solar Cells. *Chemical Reviews* **2020**, *120*, 7867-7918.

79) Saliba, M.; Matsui, T.; Domanski, K.; Seo, J. Y.; Ummadisingu, A.; Zakeeruddin, S. M.; Correa-Baena, J. P.; Tress, W. R.; Abate, A.; Hagfeldt, A. Incorporation of Rubidium Cations into Perovskite Solar Cells Improves Photovoltaic Performance. *Science* **2016**, 354, 206−209.

80. Saliba, M.; Matsui, T.; Seo, J. Y.; Domanski, K.; Correa-Baena, J. P.; Nazeeruddin, M. K.; Zakeeruddin, S. M.; Tress, W.; Abate, A.; Hagfeldt, A. Cesium-Containing Triple Cation Perovskite Solar Cells: Improved Stability, Reproducibility and High Efficiency. *Energy Environ. Sci*. **2016**, 9, 1989−1997.

81. Jacobsson TJ, Pazoki M, Hagfeldt A, Edvinsson T. Goldschmidt's rules and strontium replacement in lead halogen perovskite solar cells: theory and preliminary experiments on $CH_3NH_3SrI_3$. *J Phys Chem C* **2015**, 119:25673–83.

82) Castelli, I. E.; García-Lastra, J. M.; Thygesen, K. S.; Jacobsen, K. W. Bandgap Calculations and Trends of Organometal Halide Perovskites. *APL Mater*. **2014**, 2, 81514.

83) Wang, L.; Yuan, G. D.; Duan, R. F.; Huang, F.; Wei, T. B.; Liu, Z. Q.; Wang, J. X.; Li, J. M. Tunable Bandgap in Hybrid Perovskite $CH_3NH_3Pb(Br_{3-y}X_y)$ Single Crystals and Photodetector Applications. *AIP Adv*. **2016**, 6, 45115.

84. Jang D. M., Park K., Kim D. H., Park J., Shojaei F., Kang H. S., Ahn J. P., Lee J. W., Song J. K. Reversible halide exchange reaction of organometal trihalide perovskite colloidal nanocrystals for full-range band gap tuning. *Nano Lett.* **2015**, 15, 5191–5199.

85. Akkerman Q. A., D'Innocenzo V., Accornero S., Scarpellini A.Petrozza, A., Prato M., Manna L. Tuning the optical properties of cesium lead halide perovskite nanocrystals by anion exchange reactions. *J. Am. Chem. Soc*. **2015**, 137, 10276−10281.

86. Karimata I., Kobori Y., Tachikawa T. Direct observation of charge collection at nanometer-scale iodide-rich perovskites during halide exchange reaction on $CH_3NH_3PbBr_3$. *The Journal of Physical Chemistry Letters* **2017**, 8, 1724–1728.

87. Zhang Y., Lu D., Gao M., Lai M., Lin J., Lei T., Lin Z., Quan L. N., Yang P. Quantitative imaging of anion exchange kinetics in halide perovskites *PNAS*, **2019**, *116* 12648-12653.

88. Parobek D., Dong Y., Qiao T., Rossi D., Son D. H. Photoinduced anion exchange in cesium lead halide perovskite nanocrystals. *J. Am. Chem. Soc*. **2017**, 139, 4358–4361.

89. Dou L., Lai M., Kley C. S., Yang Y., Bischak C. G., Zhang D., Eaton S. W.,Ginsberg N. S., Yang P. Spatially resolved multicolor $CsPbX_3$ nanowire heterojunctions via anion exchange. *PNAS*, **2017**, 114, 7216–7221.

90. Roldan-Carmona C., Gratia P., Zimmermann I., Grancini G., Gao P., Graetzel M., Nazeeruddin M. K. High efficiency methylammonium lead triiodide perovskite solar cells: the relevance of non-stoichiometric precursors *Energy Environ. Sci*., **2015**, *8*, 3550-3556.

91. Chang J, Zhu H, Li B, Isikgor F H, Hao Y, Xu Q and Ouyang J Boosting the performance of planar heterojunction perovskite solar cell by controlling the precursor purity of perovskite materials *J. Mater. Chem. A* **2016**, *4*, 887–93.

92) Yin W. J., Shi T. T., Yan Y. F., Unusual defect physics in $CH_3NH_3PbI_3$ perovskite solar cell absorber *Appl. Phys. Lett*. **2014**, *104*, 063903.

93) Kim J., Lee S. H., Lee J. H., Hong K. H., The role of intrinsic defects in methylammonium lead iodide perovskite *J. Phys. Chem. Lett.* **2014**, *5*, 1312.

94) Agiorgousis M. L., Sun Y., Zeng H., Zhang S., Strong covalency-induced recombination centers in perovskite solar cell material $CH_3NH_3PbI_3$ *J. Am. Chem. Soc.* **2014**, *136*, 14570.

95) Walsh A., Scanlon D. O., Chen S., Gong X. G., Wei S. H., Self-regulation mechanism for charged point defects in hybrid halide perovskites *Angew. Chem. Int. Ed.* **2015**, *54*, 1791.

96) Buin A., Comin R., Xu J., Ip A. H., Sargent E. H., Halide-dependent electronic structure of organolead perovskite materials *Chem. Mater.* **2015**, *27*, 4405.

97. Du M. H., Correction to "Density Functional Calculations of Native Defects in $CH_3NH_3PbI_3$: Effects of Spin–Orbit Coupling and Self-Interaction Error *J. Phys. Chem. Lett.,* **2015**, *6*, 1461–1466.

98. K. A. R. Srimath, S. Neutzner, V. D'Innocenzo, F. Tassone, M. Gandini, Q. A. Akkerman, M. Prato, L. Manna, A. Petrozza, G. Lanzani Nonlinear carrier interactions in lead halide perovskites and the role of defects *J. Am. Chem. Soc*., **2016,** *138,* 13604–13611.

99. De Quilettes D. W., Vorpahl S. M., Stranks S. D., Nagaoka H., Eperon G. E., Ziffer M. E., Snaith H. J., Ginger D. S. Impact of microstructure on local carrier lifetime in perovskite solar cells *Science* ,**2015,** *348,* 683–686.

100. Leblebici S., Leppert L., Li Y., Facet-dependent photovoltaic efficiency variations in single grains of hybrid halide perovskite *Nat. Energy* **2016,** *1,* 16093.

101. Ball J., Petrozza A., Defects in perovskite-halides and their effects in solar cells. *Nat Energy* **2016**, *1*, 16149.

102) Ashkin A., Dziedzic J. M. Optical trapping and manipulation of viruses and bacteria. *Science* **1987**, 235, 1517–1520.

103) Ashkin A., Dziedzic J. M., Yamane T. Optical trapping and manipulation of single cells using infrared laser beams. *Nature* **1987**, 330, 769–771.

104. Jackson J. D, Classical Electrodynamics, 2nd ed. (Wiley, New York, 1975).

105. Neuman K. C., Block S. M. Optical trapping *Review of Scientific Instruments* **2004**, *75*, 2787.

106. Ni Z., Bao C., Liu Y., Jiang Q., Wu W., Chen S., Dai X., Chen B., Hartweg B., Yu Z., Holman Z., Huang J., Resolving spatial and energetic distributions of trap states in metal halide perovskite solar cells *Science* **2020**, *367*, 1352–1358.

107. You S.; Bi S.; Huang J., Jia Q., Yuan Y., Xia. Y., Xiao Z., Sun Z., Liu J., Sun S., Additive-Enhanced Crystallization of Solution Process for Planar Perovskite Solar Cells with Efficiency Exceeding 19%. *Chem. Eur. J*. **2017**, *23*, 18140−18145.

108) Noel N. K., Abate A., Stranks S. D., Parrott E. S., Burlakov V. M., Goriely A., Snaith H. J., Enhanced Photoluminescence and Solar Cell Performance via Lewis Base Passivation of Organic–Inorganic Lead Halide Perovskites *ACS Nano* **2014**, *8*, 9815.

109. Abate A., Saliba M., Hollman D. J., Stranks S. D., Wojciechowski K., Avolio R., Grancini G., Petrozza A., Snaith H. J., *Nano Lett*., Supramolecular halogen bond passivation of organic–inorganic halide perovskite solar cells **2014**, *14*, 3247–3254.

110. Stewart R. J., Grieco C., Larsen A. V., Maier J. J., Asbury J. B., Approaching bulk carrier dynamics in organo-halide perovskite nanocrystalline films by surface passivation *J. Phys. Chem. Lett*. **2016**, *7*, 1148.

111. Smith I. C., Hoke E. T., Solis-Ibarra D., McGehee M. D., Karunadasa H. I. A., Layered Hybrid Perovskite Solar-Cell Absorber with Enhanced Moisture Stability. *Angew. Chem.* **2014**, *126*, 11414−11417.

112. Xie F. X., Su H., Mao J, Wong K. S., Choy W. C. H. Evolution of Diffusion Length and Trap State Induced by Chloride in Perovskite Solar Cell. *J. Phys. Chem. C* **2016**, *120*, 21248－21253.

113. Chaudhary B., Kulkarni A., Jena A. K., Ikegami M., Udagawa Y., Kunugita H., Ema K., Miyasaka T. Poly(4-Vinylpyridine)-Based Interfacial Passivation to Enhance Voltage and Moisture Stability of Lead Halide Perovskite Solar Cells *ChemSusChem*, **2017**, *10* , 2473-2479

114. A 26.5% Efficient Perovskite-Silicon Tandem Cell. Available online: https://www.pv-magazine.com/2020/12/09/a-26-5-efficient-perovskite-silicon-tandem-cell

115. Huang H., Polavarapu L., Sichert J. A., Susha A. S., Urban A. S., Rogach A. L. Colloidal lead halide perovskite nanocrystals: synthesis, optical properties and applications. *NPG Asia Mater,* **2016,** 8, 167.

116. Jena A. K., Kulkarni A., Miyasaka T.Halide Perovskite Photovoltaics: Background, Status, and Future Prospects *Chem. Rev.* **2019**, *119*, 5, 3036–3103

117. Huang H., Polavarapu L., Sichert J. A., Susha A. S., Urban A. S., Rogach A. L. Colloidal lead halide perovskite nanocrystals: synthesis, optical properties, and applications. *NPG Asia Mater,* **2016,** 8, 167.

118) Lin K., Xing J., Quan L. N., de Arquer F. P. G., Gong X., Lu J., Xie L., Zhao W., Zhang D., Yan C., Perovskite light-emitting diodes with external quantum efficiency exceeding 20 per cent. *Nature* **2018**, *562*, 245–248.

119) Cho H., Jeong S.-H., Park M.-H., Kim Y.-H., Wolf C., Lee C.-L., Heo J. H., Sadhanala A., Myoung N., Yoo S., Im S. H., Friend R. H.,. Lee T.-W, Overcoming the electroluminescence efficiency limitations of perovskite light-emitting diodes *Science*, **2015**, *350*, 1222

120. Li G., Tan Z. K., Di D., Lai M. L., Jiang L., Lim J. H., Friend R. H., Greenham N. C., Efficient Light-Emitting Diodes Based on Nanocrystalline Perovskite in a Dielectric Polymer Matrix. *Nano Lett.* **2015**, *15*, 2640−2644.

121. Yuan M., Quan L. N., Comin R., Walters G., Sabatini R., Voznyy O., Hoogland S., Zhao Y., Beauregard E. M., Kanjanaboos P. Perovskite Energy Funnels for Efficient Light-Emitting Diodes. *Nat. Nanotechnol*. **2016**, *11*, 872−877.

122. Quan. L. N., Zhao Y., Garcia de Arquer F. P., Sabatini R., Walters G., Voznyy O., Comin R., Li Y., Fan J. Z., Tan H., Pan J., Yuan M., Bakr O. M.; Lu, Z.; Kim, D. H., Sargent E.H., Tailoring the Energy Landscape in Quasi-2d Halide Perovskites Enables Efficient Green-Light Emission. *Nano Lett.* **2017**, *17*, 3701−3709

123. Kim H. P., Kim J., Kim B. S., Kim H.M., Kim J., Yusoff A. R. B. M., Jang J., Nazeeruddin M. K. High-Efficiency, Blue, Green, and near-Infrared Light-Emitting Diodes Based on Triple Cation Perovskite. *Adv. Opt. Mater*. **2017**, *5*, 1600920.

124. Quan L. N., Yuan M., Comin R., Voznyy O., Beauregard E. M., Hoogland S., Buin A., Kirmani A. R., Zhao K., Amassian A. Ligand-Stabilized Reduced-Dimensionality Perovskites. *J. Am. Chem. Soc*. **2016**, *138*, 2649−2655.

125) Zhou H., Yuan S., Wang X., Xu T., Wang X., Li H., Zheng W., Fan P., Li Y., Sun L., A. Pan, Vapor growth and tunable lasing of band gap engineered cesium lead halide perovskite micro/nanorods with triangular cross section *ACS Nano*, **2017**, *11*, 1189–1195.

126) Shi Z.-F., Sun X.-G., Wu D., Xu T.-T., Tian Y.-T., Zhang Y.-T., Li X.-J., Du G.-T., Near-infrared random lasing realized in a perovskite $CH_3NH_3PbI_3$ thin film *J. Mater. Chem. C*, **2016***, 4*, 8373–8379.

127) Tang B., Dong H., Sun L., Zheng W., Wang Q., Sun F., Jiang X., Pan A., Zhang L., Single-mode lasers based on cesium lead halide perovskite submicron spheres *ACS Nano*, **2017**, *11*, 10681–10688.

128) Zhu H., Fu Y., Meng F., Wu X., Gong Z., Ding Q., Gustafsson M. V., Trinh M. T., Jin S., Zhu X. Y. Lead Halide Perovskite Nanowire Lasers with Low Lasing Thresholds and High Quality Factors. *Nat. Mater*. **2015**, *14*, 636−642.

129) Zhang Q., Ha S. T., Liu X., Sum T. C., Xiong Q. Room- Temperature near-Infrared High-Q Perovskite Whispering-Gallery Planar Nanolasers *Nano Lett.* **2014**, *14,* 5995−6001.

Chapter 2

Experiments

This chapter discusses different experimental procedures to prepare perovskite samples and instrumentation techniques used for the analysis. Here, I listed the chemicals and materials' details, explaining the sample chamber fabrication, and synthesis of perovskite microcrystals, nanocrystals, and thin films. Perovskite microcrystals are prepared by the solvent evaporation technique, and nanocrystals are prepared by the ligand-assisted reprecipitation method. Thin films of the nanocrystals are prepared by the drop-casting method. In the instrumentation section, I discuss the laser trapping system using the 1064 nm near-infrared laser and spectroscopic analysis using 1064 nm and 405 nm continuous wave lasers. The charge carrier dynamics in perovskites are studied using a time-correlated single-photon counting system. The photoluminescence spectra and bang-edge transition of perovskite nanocrystal samples are characterized by using the steady-state fluorescence and UV-vis absorption spectroscopy techniques. The sample surface analysis and elemental mapping are performed using a scanning electron microscope and the energy-dispersive X-ray spectroscopy.

2.1 Chemicals and materials

The following commercially available chemicals and materials were used in the study; methylammonium bromide, MABr (TCI, >98.0%), lead (II) bromide, PbBr2 (Aldrich, ≥98.0%), methylammonium iodide, MAI (TCI, >98.0%), *N, N*-dimethylformamide, (DMF) (Wako), isopropyl alcohol, (IPA) (Wako), 1-hexadecene (Wako), gamma-butyrolactone, (GBL) (TCI), hexadecyl amine, (C16H35N) (TCI, >95.0%), oleic acid (C18H34O2) (TCI, >85.0%), n-butanol (Wako, >99%), dehydrated toluene (Wako, >99.5%), acetone (Wako), cover glass (Matsunami, 25 mm × 25 mm, thickness 0.13–0.17 mm), and silicone glue (ShinEtsu, KE42RTV). The precursors and solvents were used as received without any further purification.

2.2 Methods

2.2.1 Fabrication of sample chamber

The experiments were carried out in a hand-made silicone chamber prepared by the following procedure (figure 2.1). First, blocks of silicone sheet with 20 mm × 20 mm size were prepared by cutting a large silicone rubber sheet with 3 mm thickness. Holes with a diameter of 4 mm were created in the center part of these rubber blocks using a cork borer. Finally, these silicone blocks are attached to the cover glass using silicone glue to fabricate the silicone chamber.

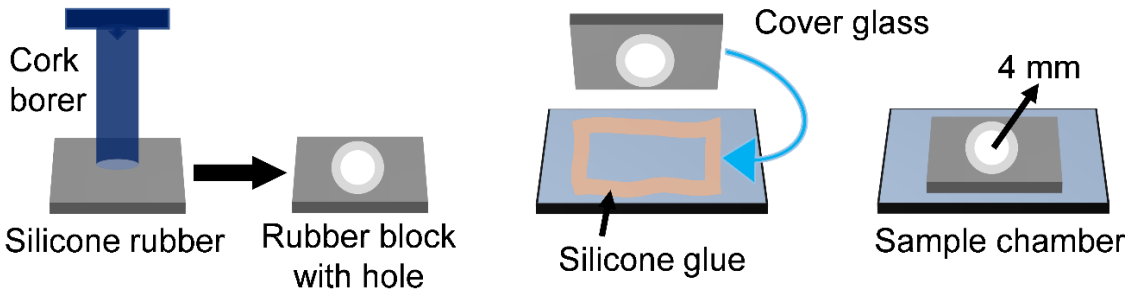

Fig 2.1: A scheme for the fabrication of sample chambers

2.2.2 Synthesis of perovskite microcrystals

The synthesis of $MAPbBr_3$ microcrystals were carried out by the spontaneous solvent evaporation method.[1–3] In the typical synthesis process, equimolar amount of precursor salts, MABr (112 mg, 1.3 mmol) and $PbBr_2$ (367 mg, 1.3 mmol), were first dissolved in 1

mL DMF solution at room temperature. The precursor salts were dissolved by stirring the mixture at 1000 rpm for 2 hours at room temperature to obtain a clear precursor solution. Surprisingly, the Br-based perovskites were reported to precipitate at elevated temperatures in DMF solution, which is termed as retrograde solubility behavior.[4] Because of the retrograde solubility characteristic, the precursor salts dissolved in DMF formed a supersaturated $MAPbBr_3$ precursor solution at room temperature. The precursor solution was then mixed with GBL solution in 1:1 (v:v) ratio to obtain an unsaturated solution. A microdroplet (ca. 1 µL) from the supernatant of the unsaturated solution was placed on the cover glass within the silicone chamber. After placing the solution on the cover glass, the microdroplet was observed under microscope. Within minutes the $MAPbBr_3$ microcrystals started growing inside the droplet through natural solvent evaporation. Microcrystals of different morphologies such as, microrods and microplates were observed to grow through the solvent evaporation. Also, samples with different sizes were obtained by varying the reaction time. For example, the small-sized microplates of 4-5 µm, which were studied in chapter 3, were obtained within 2-3 min. On the other hand, the large-sized microplates and microrods were obtained by through the same synthetic route but, with longer time. The microplates and microrods with large sizes were studied thoroughly in chapter 3, 4, and 5. However, after confirming the desired size of the crystals under optical microscope, remaining precursor solution was wiped out with filter paper to limit further growth of the crystals. Figure 2.2 represents a scheme for the preparation of microcrystals on the cover glass.

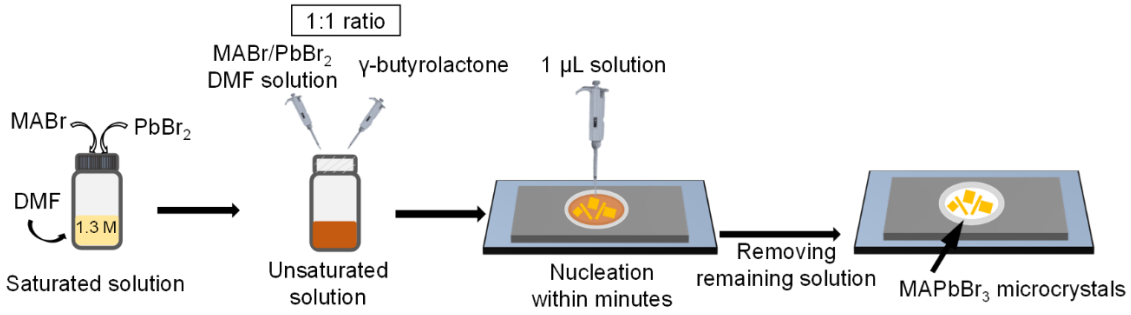

Fig 2.2: A scheme for the synthesis of $MAPbBr_3$ microcrystals

2.2.3 Synthesis of perovskite nanocrystals (PNCs)

$MAPbBr_3$ PNCs were synthesized by following the LARP method[5–7] (Figure 2.3) based on the reprecipitation technology utilizing the aggregation characteristics of perovskites in the presence of ligands.[8] During this synthesis process, precursor salts, CH_3NH_3Br (28 mg, 0.25 mmol), $PbBr_2$ (100 mg, 0.27 mmol) and ligands, oleic acid (80 µL, 0.25 mmol), and hexadecyl amine (46 mg, 0.19 mmol), were dissolved in 1 mL DMF by stirring on a hot plate. The temperature was set at 60 °C along with stirring for 30 minutes to obtain a clear precursor solution. The obtained precursor solution was then injected into 50 mL dehydrated toluene with vigorous stirring under an inert atmosphere. The solution immediately turned green, and with further mixing for 30 min, the green color gradually changed into an orange-yellow turbid solution. This color change indicates the precipitation of PNCs.

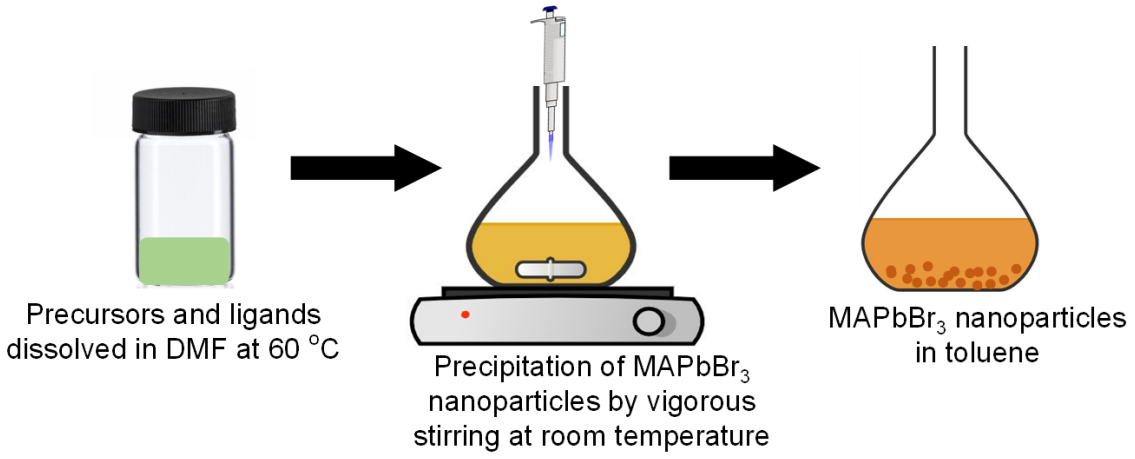

Fig 2.3: A scheme showing the synthesis of $MAPbBr_3$ nanocrystals by the LARP method.

The obtained solution was centrifuged at 10,000 rpm for 5 minutes, and the clear supernatant was discarded. The precipitate was collected and washed with 500 µL n-butanol to remove excess ligands. Finally, the solution was dispersed in toluene by sonication and centrifuged at 5000 rpm for 5 min to separate larger particles. I used the PNCs in the supernatant in my studies.

2.2.4 Preparation of perovskite nanoparticles and their films films

I prepared thin films of $MAPbBr_3$ nanoparticles by the simple drop-casting method.[7,9–11] This method involves drop-casting of $MAPbBr_3$ solution dispersed in toluene to the cover glass of the sample chamber followed by a short heating process at 60 °C to remove the solvent. Figure 2.4 shows a scheme for the preparation of thin films on the cover glass using this method.

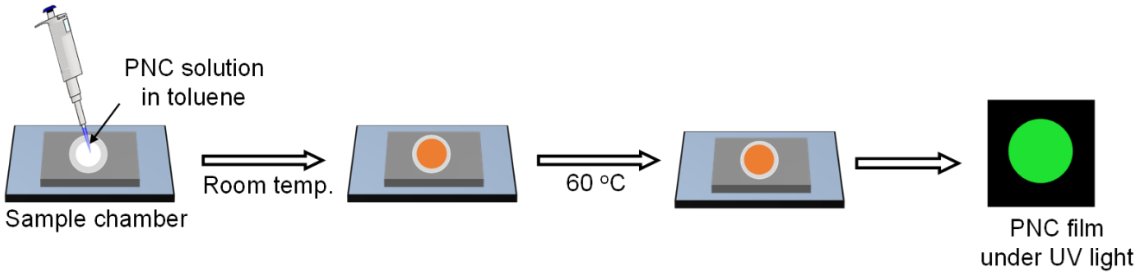

Fig. 2.4: A scheme of thin film deposition by the drop-casting method

Film thickness was controlled by the amount of the sample content in the solution. I prepared films with different thicknesses by depositing 2-10 µL of the nanoparticle solution, as necessary. Figure 2.4 shows a scheme for the preparation of thin films.

2.2.5 Preparation of reaction solutions

MABr and MAI reaction solution was prepared by dissolving MABr (8.40 mg, 0.025 mmol) and MAI (11.93 mg, 0.025 mmol) precursor salts in IPA solution. These precursor solutions were mixed with 1-hexadecene in 1:100 (v:v) ratio to prepare the final reaction solution before the reaction. The IPA solution was mixed with 1-hexadecene to prevent the perovskite sample degradation in a pure IPA solution.

2.3 Instrumentation

2.3.1 Optical setup for laser trapping

The optical system I used for the laser trapping experiments in this study consists of lasers, an inverted microscope, a charged coupled device (CCD) camera, and a spectrometer. The optical setup for laser trapping is shown schematically in figure 2.5. Each of the components used in this system is described briefly in the following section. Lasers used

in trapping experiments should have a good quality beam profile and stable output power to form the necessary intensity gradients for trapping.[12] In this study, a continuous wave

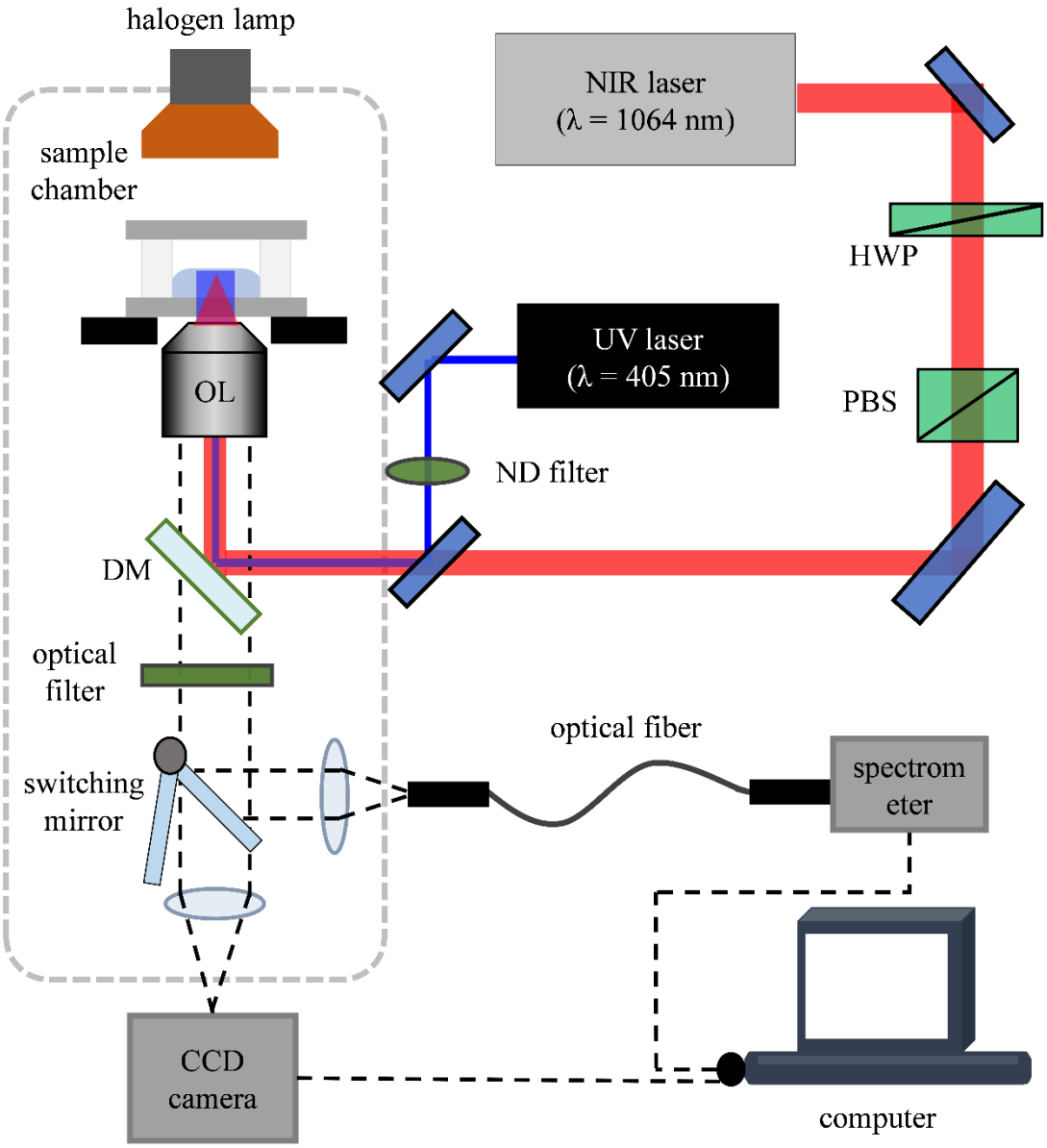

Fig. 2.5: A scheme of the optical system used for laser trapping and spectroscopic analysis.

near-infrared (NIR) Nd:YAG laser medium (Spectron laser system, λ= 1064 nm) was used as a laser source for laser trapping. A power supply system (cw 60 power supply) and a laser control system (LS101) were used for generating the NIR laser beam and controlling the laser power. Such a power control system is required because only a few milliwatts of power is required for optical trapping. Moreover, to fine-tune the optical trapping power, a polarizing beam splitter (PBS) and a half waveplate were placed in the optical path. A PBS

is used to split the monochromatic light field into two linearly polarized components in such a way where the horizontally polarized light is transmitted, and the vertically polarized one is reflected at the 90-degree angle. On the other hand, a half-wave plate was used to rotate the polarization direction of linear polarized light. The combination of PBS and half-wave plate thus enabled fine-tuning of the laser power. The NIR laser beam was then subjected to the inverted microscope (Olympus, IX71) and reflected with a dichromatic mirror. Selecting an appropriate dichroic mirror to direct the laser beam into the microscope was mandatory to have a high reflectivity at the trapping laser wavelength and transmit all other wavelengths. In this system, I used a mirror having high reflectance at 1064-nm for laser trapping and high transmittance in the visible light region. With an objective lens of 60 times magnification (Olympus, UPlan FLN) and 0.90 numerical aperture (NA), the reflected NIR laser beam was focused. The objective lens with high NA was used to minimize the focused laser spot size and to increase the electric field gradient. After passing through the objective lens, the NIR laser power was set between 0.5 to 1.0 w by rotating the half-wave plate. The power was measured directly by placing a power meter in front of the objective lens. High-quality microscope illumination is essential for obtaining images and videos with good resolutions. I used a digital camera coupled with a charge-coupled device (CCD) camera for imaging. A spectrometer (Ocean optics, Flame) connected with an optical fiber having 200 μm diameter was used for the spectroscopic analysis. While imaging and spectral recording, a band-pass filter placed below the dichromatic mirror, and before the camera removes the back-reflected laser light transmitted through the dichroic mirror.

For the wide-field illumination of the samples, an UV laser (Thorlabs, cps 405 λ=405 nm) was introduced to the microscope. The UV laser was also directed to the microscope through the same optical path as the NIR laser. The UV laser's maximum output power was measured at 4.5 mW which was 0.045 mW after passing through the objective lens because of the high transmittance of the UV laser at the dichroic mirror. The contrast of the image was adjusted using a variable reflective density filter. Objective lenses with different magnification 4x, 10x, 60x were used for the excitation as necessary.

2.3.2 Time-resolved PL analysis

Time-resolved PL analysis was carried out with a time-correlated single-photon counting (TCSPC) system (figure 2.6). TCSPC is a powerful analysis tool that records the time-

dependent intensity profile of the emitted light upon excitation by a laser pulse. This method is based on the repetitive, precisely timed registration of single photons of a fluorescence signal.[13] The TCSPC system I used in this study consists of three major parts: the excitation light, the microscope, and a photon-counting module. A picosecond pulsed laser (Advanced laser diode systems) of 465 nm wavelength and 1 MHz repetition rate was used as a source of excitation pulses. The laser diode box was connected to the laser head (Class 1 laser product, EN 60825) through a flexible wire. The laser beam was directed into the illuminator stage via some appropriate optics, e.g., lenses and mirrors, such that it passed through the objective lens (Olympus UPlan FLN, 100x magnification). An appropriate dichroic mirror was placed before the objective lens to transmit all other wavelengths beyond the excitation laser wavelength. A neutral density filter (Thorlabs, RA90/M) is used to control the light levels of the laser beam to maintain the single-photon

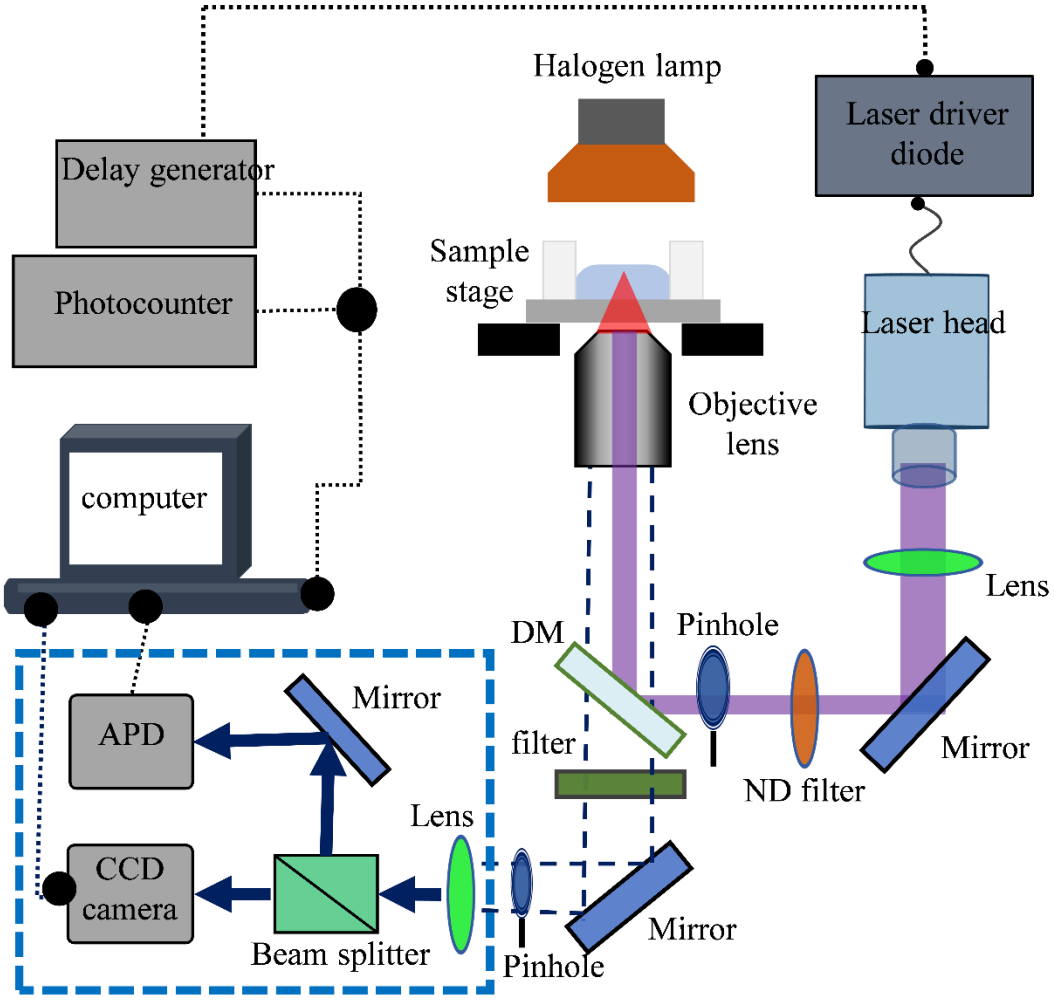

Fig. 2.6: A scheme of the optical setup used for time-resolved PL spectroscopy.

count rate to acceptable levels. The perovskite samples prepared on the coverslips were excited homogeneously or confocally upon placing on the sample stage. The emitted light was filtered out using an optical filter (OG 515 EM, XF0815) to block the scattered excitation light. Then it was directed to the photon detector placed inside a home-made black box via the lens.

I used an avalanche photodiode (APD) (PerkiElmer, SPCM-AQR 14) to detect the emitted photons from the perovskite samples. The APD was connected to a photon counting module (Becker and Hickl GmbH, SPC-830). The laser driver also provided the electronic sync signal needed for the photon arrival time measurement, which was observed by a digital delay/pulse generator (Stanford research systems, DG535). This signal was directed to the TCSPC control system via a standard coax system.

The PL decay profiles were fitted with the following tri-exponential equation,

$$y = y_0 + A1e^{-(t-t_0)/\tau_1} + A2e^{-(t-t_0)/\tau_2} + A3e^{-(t-t_0)/\tau_3}$$

Here, 't' is time, A_1, A_2, and A_3 are amplitudes and τ_1, τ_2, and τ_3 are the corresponding lifetimes of the three components.

2.3.3 UV-vis absorption spectroscopy

To examine the absorbencies of PNCs solutions, I used a UV-vis absorption spectrophotometer (Evolution 220, Thermo-Fischr scientific). A scheme for the instrumentation of the UV-vis spectroscopy is shown in Figure 2.7. The absorption spectrometer principally works on the Beer-Lambert-Bouguer law, which states, the absorbance (A) of the solution is proportional to the concentration (c) and the path length (l), that is, A=εcl, where, ε is the molar extinction coefficient (M^{-1} cm^{-1}).[14]

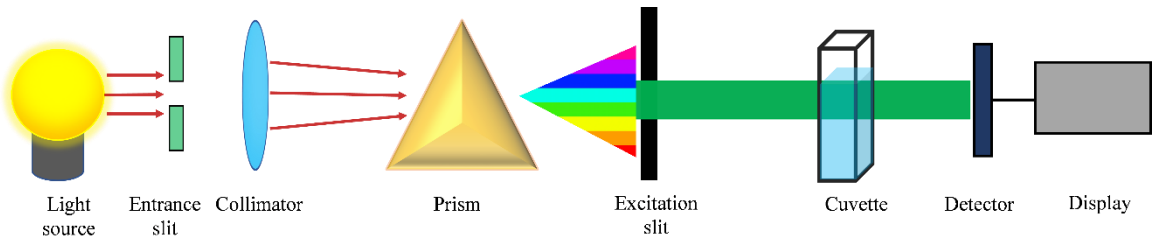

Fig. 2.7: A scheme showing the optical setup and working principle of a UV-vis spectrophotometer.

The basic construction of the spectrometer has four components, e.g., a light source, a monochromator, a sample holder, and a detector associated with the readout system. In the conventional spectrometer, a combination of a hydrogen or deuterium lamp and a tungsten filament was used as the light sources which cover the wavelength region from 190 to 900 nm. The radiation was separated according to its frequency/wavelength in the monochromator and passed through the narrow slit to a sample solution. A solution placed in a cuvette (1 cm) partly absorbs the incident light, and the transmitted light is recorded by the spectrometer. In this study, I measured the absorption spectra of the PNCs from 400 to 800 nm range by correcting the baseline with toluene and dispersing the PNC samples in toluene.

2.3.4 Steady-state fluorescence spectroscopy

The emission properties of the PNCs were studied here using a fluorescence spectrometer (F-4500, Hitachi). I used the fluorescence spectrometer to understand the relaxation process of the excitons from the excited states to the ground states. The basic working principle of a fluorescence spectrometer is schematically shown in Figure 2.8. The spectrometer contains a number of convenient optical features, which surrounds the sample holder.

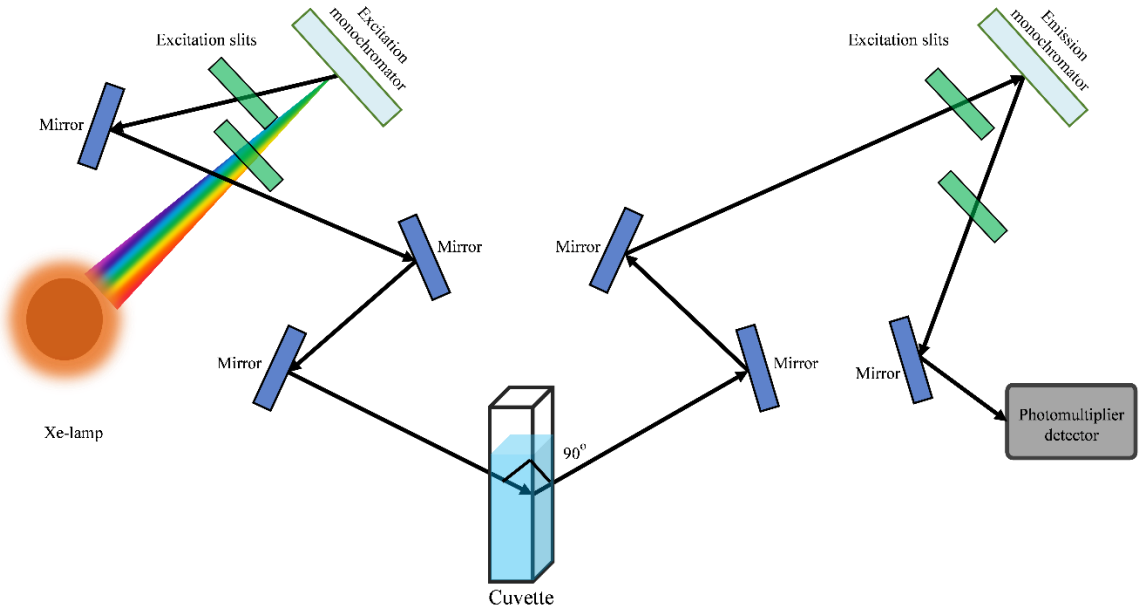

Fig. 2.8: A scheme of the steady-state fluorescence spectroscopy system.

A Xe-lamp was used as a source of exciting light, which can provide a wavelength-dependent continuous light output from the UV to the NIR range. A diffraction grating

monochromator was used to obtain maximum efficiency to detect low light levels for a selected wavelength. The excitation monochromator selectively passed the desired wavelength to the sample through an assembly of diffraction gratings and slits. The PNC solution taken in a quartz cuvette was placed inside the sample holder. The photoexcitation generated photons and the emitted photons were collected by the emission monochromator. Since the emitted photons has a higher energy than the excitation wavelength, the emission monochromator efficiently filters the excitation light. Also, the 90^{o} angle between the excitation and emission paths, created by placing the slits in appropriate positions, limited the excitation light to reach the emission monochromator. Finally, the emission was detected by the photomultiplier tube and recorded as spectrum. The PNC sample studied here was dispersed in toluene and a very dilute solution was used for the detection of emission.

2.3.5 Scanning Electron Microscope (SEM) and Energy dispersive x-ray (EDX) analysis

SEM images of the prepared perovskite samples were taken by (SEM, HITACHI, SU8230). After crystallization and drying-up of the crystals on ITO glass, the sample deposited on copper tape was pasted on the sample stage. The electron gun located at the top of the column generates a beam of electrons, which was guided down the column using the gun alignment control. The beam was condensed by lenses and focused on the sample using an objective lens. A magnetic field was created by energizing the scan coils to deflect the electron beam back and forth in a controlled pattern. When the beam touches a sample surface, it produces secondary electrons. These induced secondary electrons were collected by an appropriate detector and converted into a voltage signal. The varying voltage produced by the scan coils created the patterns on the surface of the sample, and the detected voltage signal from the sample was applied to the cathode ray tube, which createed the image on the screen.

EDX technique was used for the elemental analysis, which relies on the investigation of the interaction between x-rays and a sample. In this study, I used EDX (Bruker, QUANTAX EDS) coupled with the SEM instrument for the elemental analysis of the perovskite samples. SEM and EDX were operated at an acceleration voltage of 1 kV and 15 kV, respectively. Total collection time was set for 1 minute for the measurements.

2.4 References

(1) Nguyen, V.C.; Katsuki, H.; Sasaki, F.; Yanagi, H. Single-Crystal Perovskites Prepared by Simple Solution Process: Cast-Capping Method. *J. Cryst. Growth* **2017**, *468*, 796–799.

(2) Shahjahan, M.; Yuyama, K.; Okamoto, T.; Biju, V. Heterojunction Perovskite Microrods Prepared by Remote‐Controlled Vacancy Filling and Halide Exchange. *Adv. Mater. Technol.* **2021**, 6 (2), 2000934.

(3) Islam, M. J.; Shahjahan, M.; Yuyama, K. I.; Biju, V. Remote Tuning of Bandgap and Emission of Lead Perovskites by Spatially Controlled Halide Exchange Reactions. *ACS Mater. Lett.* **2020**, *2* (4), 403–408.

(4) Saidaminov, M. I.; Abdelhady, A. L.; Maculan, G.; Bakr, O. M. Retrograde Solubility of Formamidinium and Methylammonium Lead Halide Perovskites Enabling Rapid Single Crystal Growth. *Chem. Commun.* **2015**, *51* (100), 17658-17661.

(5) Sun, S.; Yuan, D.; Xu, Y.; Wang, A.; Deng, Z. Ligand-Mediated Synthesis of Shape-Controlled Cesium Lead Halide Perovskite Nanocrystals via Reprecipitation Process at Room Temperature. *ACS Nano* **2016**, *10* (3), 3648–3657.

(6) Schmidt, L. C.; Pertegás, A.; González-Carrero, S.; Malinkiewicz, O.; Agouram, S.; Mínguez Espallargas, G.; Bolink, H. J.; Galian, R. E.; Pérez-Prieto, J. Nontemplate Synthesis of $CH_3NH_3PbBr_3$ Perovskite Nanoparticles. *J. Am. Chem. Soc.* **2014**, *136* (3), 850–853.

(7) Ghimire, S.; Chouhan, L.; Takano, Y.; Takahashi, K.; Nakamura, T.; Yuyama, K.; Biju, V. Amplified and Multicolor Emission from Films and Interfacial Layers of Lead Halide Perovskite Nanocrystals. *ACS Energy Lett*. **2019**, *4* (1), 133–141.

(8) Zhang, F.; Zhong, H.; Chen, C.; Wu, X.; Hu, X.; Huang, H.; Han, J.; Zou, B.; Dong, Y. Brightly Luminescent and Color-Tunable Colloidal $CH_3NH_3PbX_3$ (X = Br, I, Cl) Quantum Dots: Potential Alternatives for Display Technology. *ACS Nano* **2015**, *9* (4), 4533–4542.

(9) Nie, W.; Tsai, H.; Asadpour, R.; Blancon, J.-C.; Neukirch, A. J.; Gupta, G.; Crochet, J. J.; Chhowalla, M.; Tretiak, S.; Alam, M. A.; Wang, H.-L.; Mohite, A. D. High-Efficiency

Solution-Processed Perovskite Solar Cells with Millimeter-Scale Grains. *Science* **2015**, *347* (6221), 522–525.

(10) Mei, A.; Li, X.; Liu, L.; Ku, Z.; Liu, T.; Rong, Y.; Xu, M.; Hu, M.; Chen, J.; Yang, Y.; Gratzel, M.; Han, H. A Hole-Conductor-Free, Fully Printable Mesoscopic Perovskite Solar Cell with High Stability. *Science* 2014, *345* (6194), 295–298.

(11) Hu, Y.; Si, S.; Mei, A.; Rong, Y.; Liu, H.; Li, X.; Han, H. Stable Large-Area (10 × 10 Cm^2) Printable Mesoscopic Perovskite Module Exceeding 10% Efficiency. *Sol. RRL* **2017**, *1* (2), 1600019.

(12) Liu, Z.; Wang, X.; Hang, K. Enhancement of Trapping Efficiency by Utilizing a Hollow Sinh-Gaussian Beam. *Sci. Rep*. **2019,** *9* (1), 10187.

(13) Becker, W.; Bergmann, A.; Koenig, K.; Tirlapur, U. Picosecond Fluorescence Lifetime Microscopy by TCSPC Imaging. In Multiphoton Microscopy in the Biomedical Sciences; Periasamy, *A., So, P. T. C.*, **2001**; *4262*, 414.

(14) Grinter, H. C.; Threlfall, T. L. UV-VIS Spectroscopy and Its Applications.

Chapter 3

Bandgap tuning of lead halide perovskite by site-specific halide exchange reaction under laser trapping

Halide perovskites, owing to their unique excitonic and charge carrier properties, become the most promising semiconductor materials for next generation optoelectronic devices. The optical and electronic properties of perovskites can be modified in the entire UV-visible to near infrared region by tuning the bandgaps. Halide exchange reaction is a post-synthesis approach for the bandgap tuning. Upon exposing a parent perovskite crystal to the reactant halide solutions, the bandgap is varied homogeneously in the entire region. Here, I demonstrate the site-specific halide exchange reaction in the halide perovskite microplates and microrods with the use of a focused near-infrared laser beam. Perovskite microcrystals and microrods are prepared by the simple solvent evaporation technique. To induce the site-specific halide exchange, a near-infrared laser beam was focused onto the surface of the perovskite crystals by immersing them in a reactive halide precursor solution. The local halide exchange reaction was induced in the entire region of the selected small microplates and also at the desired center part of the large microplates. To check the universality of the laser trapping initiated local halide exchange reaction, I further demonstrated the bandgap tuning at a specific part of the microrod crystals. Spatio-temporal changes in the photoluminescence emission and spectra are studied precisely under near-infrared laser irradiation and wide-field ultraviolet laser irradiation. I discuss the possible mechanism of the site-specific halide exchange reaction from the viewpoint of local concentration increase of the halide ions at the focal volume under laser trapping.

3.1 Introduction

Halide perovskites have emerged as a class of promising semiconductor materials and being studied intensively in the fabrication of next generation cost-effective photovoltaic and optoelectronic devices such as solar cells, light emitting diodes, detectors, displays, sensors and lasers.[1-9] These promising applications of perovskite materials depend on their outstanding optoelectronic properties, including strong light absorption, high photoluminescence (PL) quantum yield, small exciton binding energy, long charge carrier diffusion lengths and remarkable bandgap tunability.[10-15] The unique excitonic and charge carrier properties of the perovskites are undoubtedly dependent on the bandgap, which is the most critical parameter in the perovskite materials for almost all applications. In most cases, halide perovskites are direct-bandgap semiconductor materials with strong band-edge optical absorption and PL emission from ultraviolet to near-infrared (NIR) wavelength region.[16,17] A wide range of bandgaps have been achieved through different compositional engineering by varying the cations, metals, or anions of halide perovskites.[18-27] Since the valance band maximum of lead halide perovskites is mainly contributed by the *p*-orbitals of halogens, the crystal structure and bandgap of these materials are mostly dependent on the halide composition. Thus the halide exchange reaction provides a facile way for the bandgap tuning, which can be achieved by mixing different halide ions in proper ratios. Halide exchange reaction generally proceeds via the spontaneous diffusion of guest halide ions inside the parent crystal through the soft crystal lattice of perovskites. The large halide concentration gradient between the parent crystal and precursor solution allows the diffusion of halide ions from the precursor into the parent crystal and induce partial or complete substitution of the original halide ions.

Several research groups have demonstrated the post-synthetic halide exchange reaction in 0D, 1D, 2D, and 3D perovskite materials and studied the change in structures and properties of these materials.[28-36] For instance, Kovalenko group[30] demonstrated the postsynthetic chemical transformation of colloidal $CsPbX_3$ nanocrystals (NCs) through an anion exchange reaction. The highly mobile halide ions from the desired halide source resulted remarkably fast anion exchange and resulted the PL emission color and spectral tuning of the parent $CsPbX_3$ NCs. Similarly, Akkerman et al.[29] demonstrated the tuning of chemical composition and optical properties of the pre-synthesized colloidal $CsPbX_3$ NCs through postsynthetic anion exchange reactions using a range of different halide precursors. The anion exchange reaction proceeded without any significant change in the structure of

the initial NCs. Moreover, Jang et al.[28] showed the reversible halide exchange of plate-shaped $MAPbX_3$ NCs. They synthesized a series of mixed halide $MAPbBr_{3-x}Cl_x$ or $MAPbBr_{3-x}I_x$ nanocrystals from the as-grown $MAPbBr_3$ nanocrystals by treating them with MACl and MAI precursor solutions and achieved a full range bandgap tuning from 1.6 to 3.0 eV. Zhang et al.[34] reported the full range compositional tuning of 1D $CsPbBr_3$ nanowires from 409 to 680 nm spectral range via anion exchange reaction by reacting them with the new guest halide ions.

Beside these, halide exchange reaction has also been studied widely in bulk single crystals of perovskites. As an example, Karimata et al.[35] reported the halide exchange reaction of a single $MAPbBr_3$ crystal upon immersing the crystals in an MAI reaction solution and revealed the charge carrier dynamics during the exchange reaction. While these reports provided post-synthesis halide exchange reaction to alter the emission and bandgap homogeneously over the whole crystals, several groups also reported spatially-resolved halide exchange reaction. For example, Son et al.[33] demonstrated a photoinduced halide exchange reaction in the absence of any reacting anion source. The photoinduced electron transfer from $CsPbX_3$ NCs to a halogenated solvent induces the spatial exchange reaction. They also demonstrated patterning of $CsPbBr_3$ in a fluorescent thin film of $CsPbCl_3$ NCs by partially irradiating them. Yang and co-workers reported[36] precisely controlled anion exchange in single crystalline $CsPbX_3$ perovskites by combining the anion exchange reaction with the nanofabrication technique. A spatially resolved halide exchange reaction was induced in a specific uncovered area by dipping the crystals into an oleylammonium halide precursor. The other parts of the crystals were masked with a thin layer of poly (methyl methacrylate) to avoid the exchange reaction. These halide exchange reactions at a desired location proceed through very sophisticated techniques, which are at the same time costly and time consuming. Thus, flexible and facile method for spatially-resolved halide exchange reaction and bandgap engineering is yet to develop.

In this chapter, I introduced a new laser trapping based methodology to induce halide exchange reaction in microcrystals and microrods of lead halide perovskites in a temporally and spatially controlled manner. Laser based optical trapping was pioneered by Arthur Ashkin in the early 1970s.[37] A variety of novel techniques were developed based on laser trapping to manipulate microscopic objects by confining, organizing, assembling, or modifying them. For instance, Ashkin et al. utilized the optical tweezer system in a biological system to manipulate viruses, living cells and organelles.[38-40] The optical tweezer was also studied extensively in chemistry to grow or confine several molecules such as

proteins, amino acids, polymers, nanoparticles and quantum dots in the focal volume, where the assemblies were formed through trapping.[41-48] Hosokawa et al.[46] reported an increase in fluorescence intensity of polystyrene nanoparticles at the focal volume under laser trapping. The trapping mechanism was explained from the viewpoint of sequential gathering and gradual occupying of nanoparticles at the focal volume. Here, I demonstrated the laser trapping of reactive halide precursors at the surface of a perovskite crystal to control the exchange reaction in a specified domain through the local increase in the concentration of halide precursors.

3.2 Results and Discussions

3.2.1 Spatially controlled halide exchange

The halide exchange reaction on a selective $MAPbBr_3$ was carried out spatially by utilizing the laser trapping technique. Micrometer-sized $MAPbBr_3$ crystals were prepared on a clean cover glass inside a hand-made silicone chamber by spontaneous solvent evaporation method. First, the $MAPbBr_3$ precursor solution (1.3 M) was prepared by dissolving MABr and $PbBr_2$ salts in DMF and mixed with GBL in a 1:1 (v:v) ratio to obtain an unsaturated solution. A droplet (ca. 1 μL) of the solution was then placed on the cover glass, where the crystallization took place within minutes through spontaneous solvent evaporation. After confirming the growth of the crystals on the cover glass with an optical microscope remaining solution was wiped out with filter paper. Figure 3.01a represents an optical image of four $MAPbBr_3$ microcrystals prepared from the precursor solution. The square-shaped crystals were observed with a size varying from 4-5 μm. Prior to the exchange reaction, all the four crystals showed intense green emission under a 405 nm wide-field excitation laser illumination (Figure 3.01b). This green emission from the crystals is due to the band-to-band transition, which is characteristic of $MAPbBr_3$ crystals. After preparing, the crystals were immersed in a reaction solution of MAI to induce the halide exchange reaction. The MAI reaction solution was prepared by dissolving MAI precursor salts in isopropyl alcohol followed by mixing with 1-hexadecene. A freshly prepared MAI reaction solution was added inside the sample chamber. The final concentration and amount of the reaction solution I used was 125 μM and 50 μL respectively. A low concentration of MAI reaction solution is required in the laser induced halide exchange reaction because the exchange reaction is strongly dependent on the concentration of the reaction solution. Spontaneous halide exchange reaction proceeds at a negligibly small rate when the

concentration of the MAI solution was 125 μM, while a higher concentration than this can accelerate the spontaneous

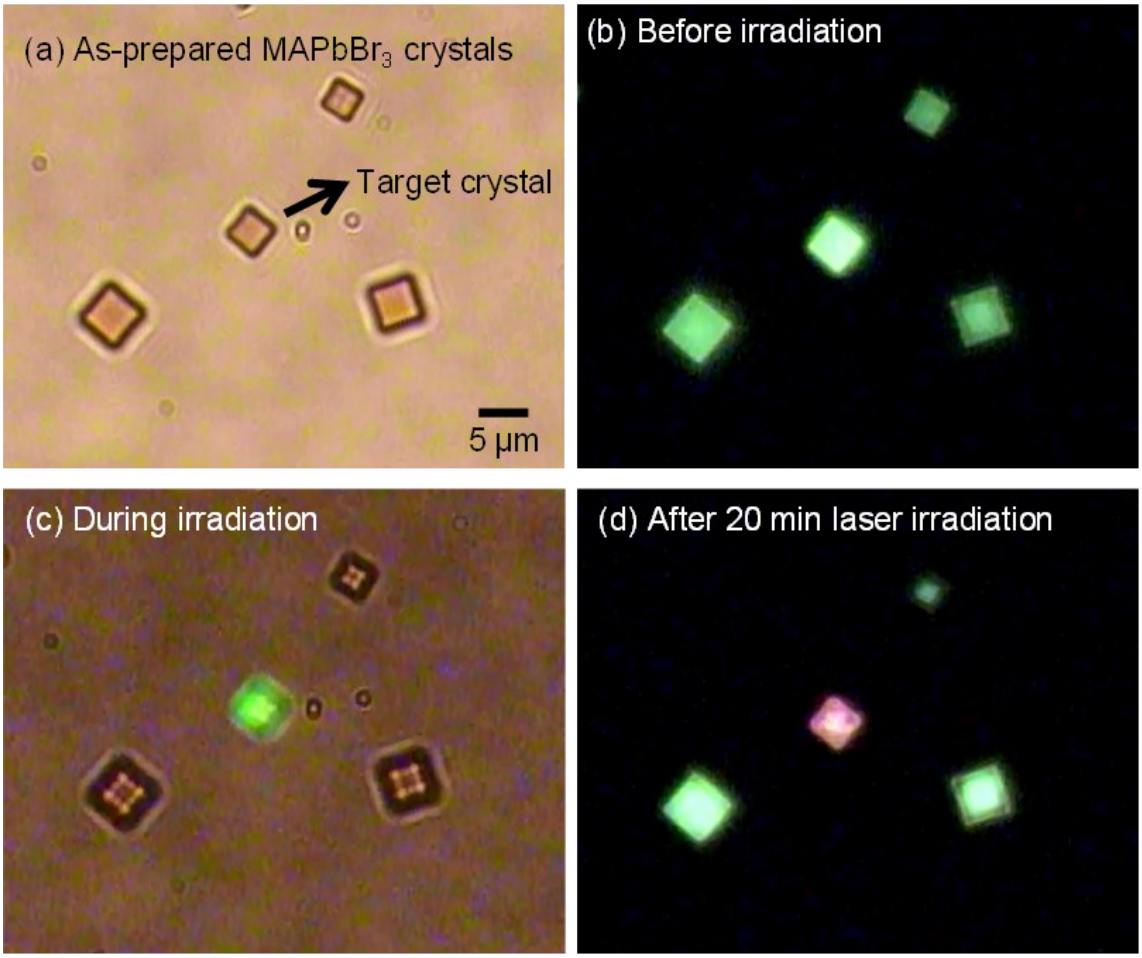

Figure 3.01: (a) An optical transmission micrograph of as-prepared $MAPbBr_3$ crystals in the sample chamber. (b) PL images of the crystals under UV laser irradiation before the exchange reaction. (c) A combined transmission and PL image during laser irradiation using a NIR laser. (d) PL images of the crystals under UV laser irradiation after the halide exchange reaction.

exchange reaction dramatically. However, after immersing the crystals in an MAI solution the NIR laser beam was tightly focused on a selected crystal (Figure 3.01c) and irradiated for 20 min. Interestingly, after the laser irradiation, only the irradiated crystal showed a change in emission color. The initial green emission of the selected crystal changed to red after the irradiation while the neighbouring crystals remained green emissive under wide-field excitation with 405 nm laser (Figure 3.01d). These results indicate that the focused laser irradiation induced the halide exchange reaction, which results in bandgap tuning in a spatially selective manner.

Furthermore, I observed the progress of the halide exchange reaction of the selected crystal with time and recorded the PL spectra (Figure 3.02). At the beginning of the reaction, the crystal showed green emission under

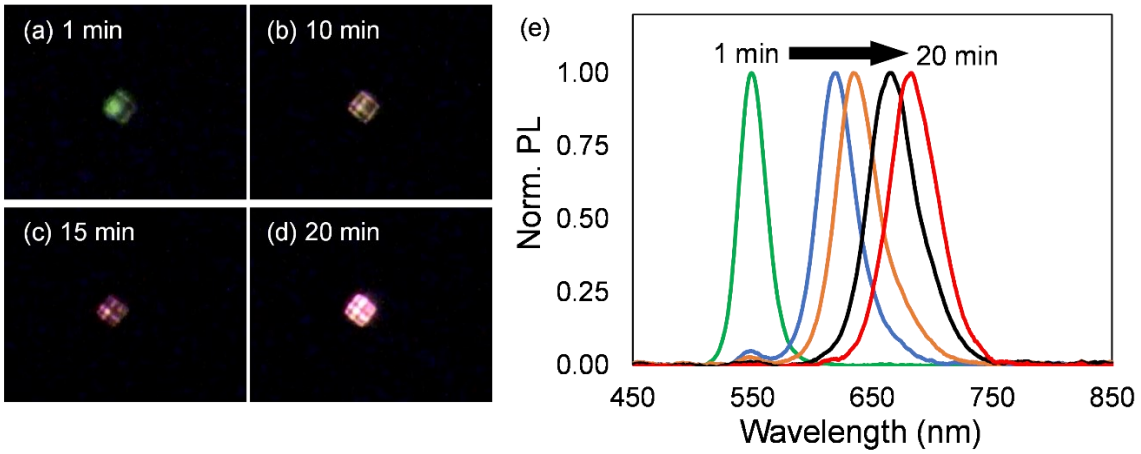

Figure 3.02: (a-d) Temporal changes in PL images of the target crystal under NIR laser irradiation at (a) 1min, (b) 10 min, (c) 15 min and (d) 20 min. (e) PL spectral change of the $MAPbBr_3$ crystal under laser trapping

the irradiation with NIR laser. As the reaction proceeded, the green emission of the crystal gradually changed into first orange-yellowish and finally red (Figure 3.02a-d). Along with the color change, the PL intensity also increased during the irradiation and finally a bright red PL was observed at 20 min. To understand the exchange reaction quantitatively, PL spectral changes were also recorded under the NIR laser irradiation (Figure 3.02e). The initial crystal showed PL spectral maxima at 545 nm. After 5-min of laser irradiation, a new red-shifted emission band appears at 615 nm which continuously shifted to a low energy emission band and finally reached upto 677 nm after 20 min. The PL peak at 677 nm indicated that the as-prepared $MAPbBr_3$ crystal was changed to $MAPbBr_nI_{3-n}$ which further confirmed the halide exchange reaction of the selected crystal.

3.2.2 Spatially controlled halide exchange in single microplate crystals:

The 1064 nm NIR laser was then utilized to perform the halide exchange reaction in a selected part of a large $MAPbBr_3$ crystal. For this experiment, a large-sized $MAPbBr_3$ crystal was prepared following a similar synthetic route. In this case, after placing the microdroplet of the precursor solution on the cover glass, the solution was kept for a long time to obtain large crystals. The growth of the crystals was observed under the microscope and the remaining precursor solution was removed after confirming the

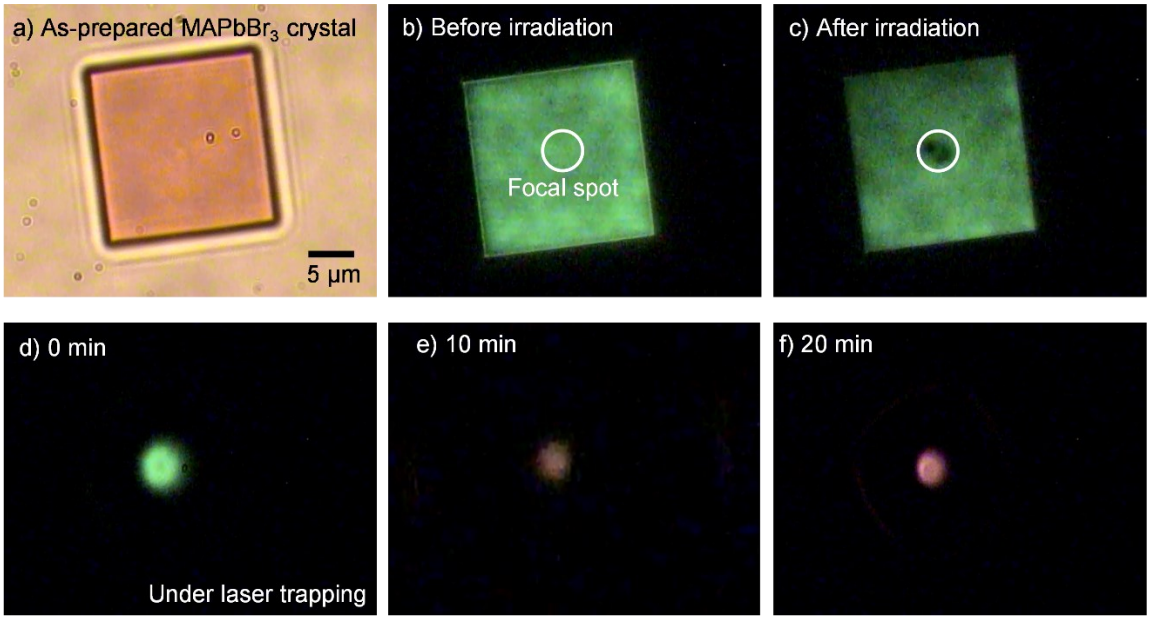

Figure 3.03: (a) An optical transmission micrograph of the as-prepared $MAPbBr_3$ crystal in the sample chamber. (b) PL image of the crystal under UV laser irradiation before the exchange reaction. (c) PL images of the crystals under UV laser irradiation after the halide exchange reaction. (d) Temporal changes in PL images at the focal volume under NIR laser irradiation at (a) 0 min, (b) 10 min, (c) 15 min, and (d) 20 min.

crystallization of the $MAPbBr_3$ crystals. Figure 3.03a represents an optical micrograph of an as-prepared $MAPbBr_3$ crystal with a size of 50×40 μm^2. The as-prepared crystal showed green emission from the entire region under wide-field excitation with 405 nm laser which is one of the characteristic features of a $MAPbBr_3$ crystal (Figure 3.03b). Then, the reaction solution MAI of concentration 125 μM was put in the sample chamber. Immediately after immersing the crystal with the reaction solution, the laser beam from the NIR laser was focused on the center part of the crystal. Under the laser irradiation, an intense green emission from the focal spot was observed at the beginning of the reaction. The laser irradiation was continued for 20 min. With time, a change in the emission color from the focal spot was observed. The initial green emission first changed into orange-yellowish and finally became red within 20 min (Figure 3.03d-f). This emission color change at the irradiated part allowed us to consider that the halide exchange reaction at the focal spot had taken place under laser trapping. I assumed that the exchange reaction taken place only at the irradiated part covered by the focal volume of the laser, whereas the other parts of the crystal will remain unchanged. To validate the assumption, the whole crystal was excited homogeneously with a 405 nm laser, but a nonluminescent black spot at the irradiated part

of the crystal was observed, while the other parts remain green emissive as the initial crystal (Figure 3.03c). This phenomenon is due to the thickness of the as-prepared crystal. The halide exchange reaction at the center part of the crystal was induced by focusing the NIR laser beam on the upper surface of the crystal. On the other hand, the 405 nm laser can excite the crystal up to a certain limit from the lower part because of its limited excitation depth. The excitation depth of laser in materials can be determined by Beer-Lambert law. According to this law,[49] the intensity of laser radiation falls off exponentially from the surface of a material as,

$I = I0e^{-\alpha x}$

Where, α is absorption coefficient (m^{-1}), I_0 is incident light intensity, I is transmitted light intensity, and x is optical path length (m). α is dependent on the materials and wavelength of the incident light. In case of $MAPbBr_3$, the absorption coefficient at 400 nm is in the scale of 10^5 cm^{-1} (= 0.01 nm^{-1}). Thus, the excitation depth was calculated 500 nm.

To validate this phenomenon, I measured the thickness of the microcrystals using themathematically optimized *Sellmeier dispersion formula*:

$$\eta^2=A+B/(\lambda^2-c)-D\lambda^2$$

where, η is the refractive index, λ is the wavelength in micrometres and A, B, C, D are constant values. All these parameters were obtained by least-squares fitting and the values are listed in Table 1[50]

Table 3.1: The fitted parameters of the $MAPbBr_3$ single crystals in the Sellmeier dispersion equation

Crystal	A	B	C	D
$MAPbBr_3$	3.565	0.253	0.135	-0.118

Using the above listed values for every wavelength (λ) the refractive index (η) values were determined and then by using these η values the intensity (I) was calculated by the following equation:

$$I \propto \left(1 + cos\frac{4n\pi d}{\lambda}\right)^2 + sin^2\left(\frac{4n\pi d}{\lambda}\right)$$

Here, *d* is the thickness of the crystal. Comparing this calculated value with the measured reflectance value, I determined the thickness of the crystal. For this representative microcrystal, the thickness was measured 2123.96 nm from the fitted curve.

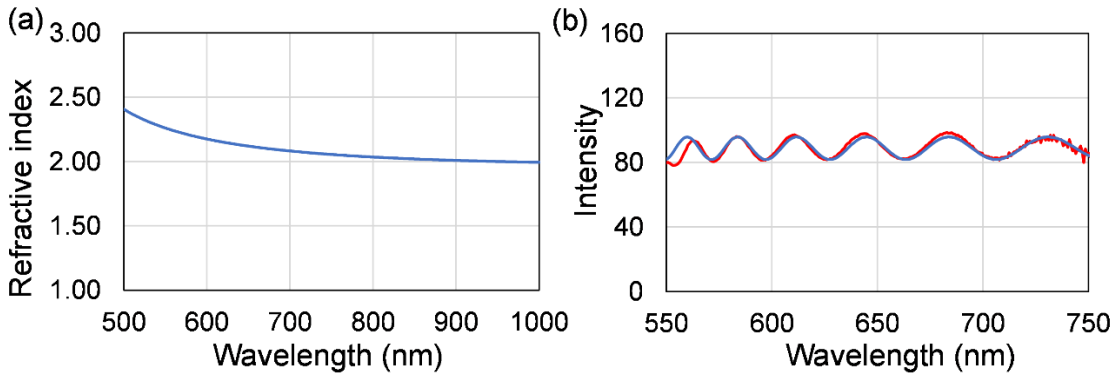

Figure 3.04: (a) Refrective index value measured as a function of wavelength value (b) Fitted curve to determine the crystal thickness by camparing calculated and measured intensity value

However, to observe the upper surface of the crystal the sample chamber was flipped and again observed under the 405 nm laser. Interestingly, after flipping the coverslip when the same crystal was excited using 405 nm laser, the exchanged part was visible with a red emission from the center part of the crystal (Figure 3.05a,b). At the same time remaining part of the crystal was unchanged, which confirmed the halide exchange reaction selectively at the irradiated center part.

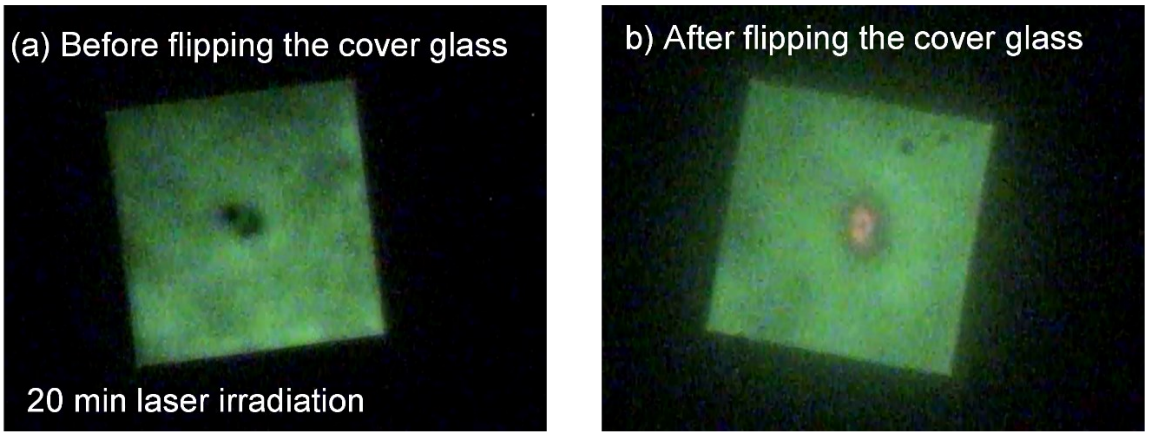

Figure 3.05: PL images of the crystal after the halide exchange reaction by NIR laser irradiation (a) before flipping the cover glass, (b) after flipping the cover glass to observe the upper surface.

The halide exchange reaction at the center part of the crystal was further confirmed by PL spectroscopic analysis under laser trapping. At the beginning of the exchange reaction, the center part of the crystal showed an emission peak at 545 nm which is characteristic of a $MAPbBr_3$ crystal. With time, the emission peak continuously

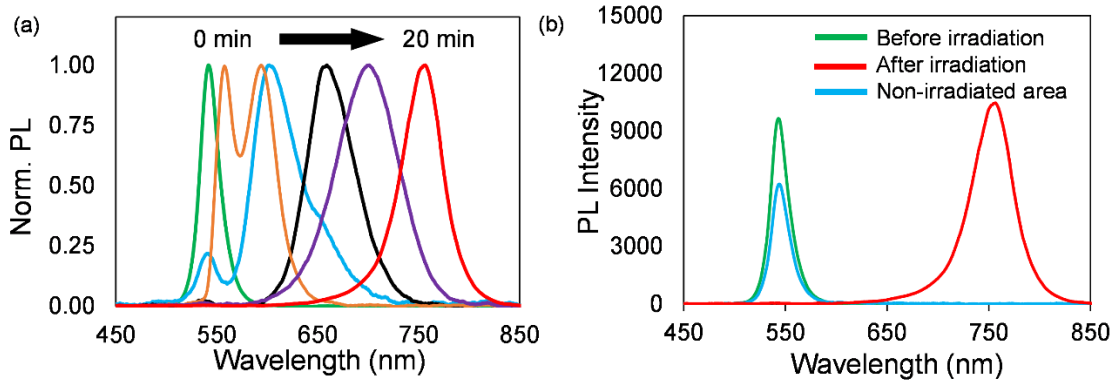

Figure 3.06: (a) PL spectral change of the $MAPbBr_3$ crystal under laser trapping. (b) PL spectra of the crystal in an MAI reaction solution at the irradiated and nonirradiated areas.

red-shifted under the NIR laser irradiation. After 20 min of laser irradiation, an emission peak at 750 nm was observed from the focal spot along with the change of emission color (Figure 3.06a). After the exchange reaction, PL emission from the non-irradiated parts of the crystal was also measured (Figure 3.06b). The emission peak wavelength at the non-irradiated parts was the same as the prepared crystal while the emission peak at the irradiated part shifted to 750 nm. Although the emission peak was kept constant, the PL intensity decreased compared to the initial value. However, the decrease in PL intensity can be discussed from the following band energy alignments.[53] The low PL intensity during the reaction was resulted from the generation of low iodide composed $MAPb(Br.I)_3$ from pristine $MAPbBr_3$ crystal. When a $MAPbBr_3$ crystal is partly replaced by a small amount of iodide ions ($0 < x < 1$ in $MAPbBr_{3-x}I_x$), the energy difference between the conduction bands of $MAPbBr_{3-x}I_x$ and $MAPbBr_3$ become comparable to the room temperature thermal energy which is 0.025 eV. Contrarily, the large valance band energy gaps between them occupy the photogenerated holes in the iodide rich domain. These unique band structures allow the photogenerated electrons to be delocalized between the conduction bands of $MAPbBr_{3-x}I_x$ and $MAPbBr_3$ regions and limits the recombination with the trapped holes localized in $MAPbBr_{3-x}I_x$ domains. Thus, the crystal structure with smaller x values prevent the radiative recombination and quench the PL emission. In addition, the photogenerated holes from $MAPbBr_3$ crystals are readily captured by the adsorbed iodide ions at the surface

which also possess the PL quenching. As the result, the emission from the non-irradiated parts was quenched and the PL intensity of $MAPbBr_3$ was decreased without emission from $MAPbBr_nI_{3-n}$.

To avoid the observation problem with microplate-shaped crystals after the exchange reaction, I further investigated the halide exchange reaction in microrod-shaped $MAPbBr_3$ crystals. The crystals were prepared following the same synthetic route via natural solvent evaporation technique. Along with the growth of large microplates inside the precursor droplet, microrods of different size were also found (Figure 3.07).

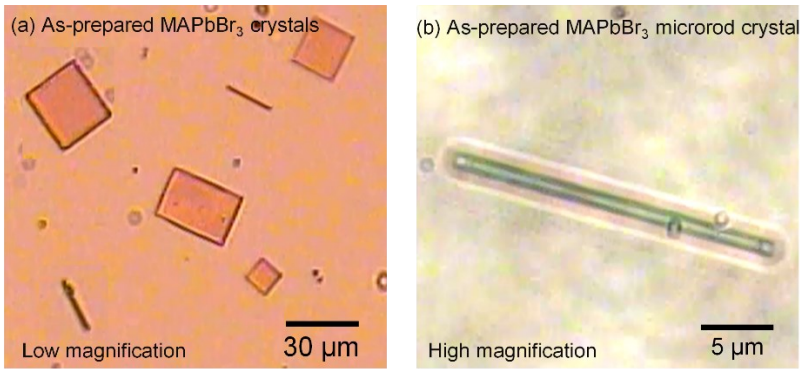

Figure 3.07: Optical micrographs of the as-grown microplate and microrod shaped crystals under (a) low magnification. (b) high magnification.

3.2.3 Spatially controlled halide exchange in single microrod crystals:

Halide exchange reaction at the desired location of microrod-shaped $MAPbBr_3$ crystals was carried out by locally irradiating them with the NIR laser beam. After preparing $MAPbBr_3$ microrods in a sample chamber, a freshly prepared reaction solution of MAI (125 µM) was added to the sample chamber. Subsequently, the center area of the microrods were irradiated by a tightly focused NIR laser beam to induce the halide exchange reaction. Also, a high concentration of reaction solution was avoided to suppress the spontaneous exchange reaction during the laser-induced exchange reaction. Figure 3.08a shows a PL image of the as-prepared $MAPbBr_3$ microrod which was green emissive in the whole area when illuminated by a 405 nm laser. After immersing the microrod in a MAI reaction solution, the center area of the microrod was irradiated with an NIR laser beam. Under laser irradiation, the irradiated center part showed an intense green emission at the focal spot.

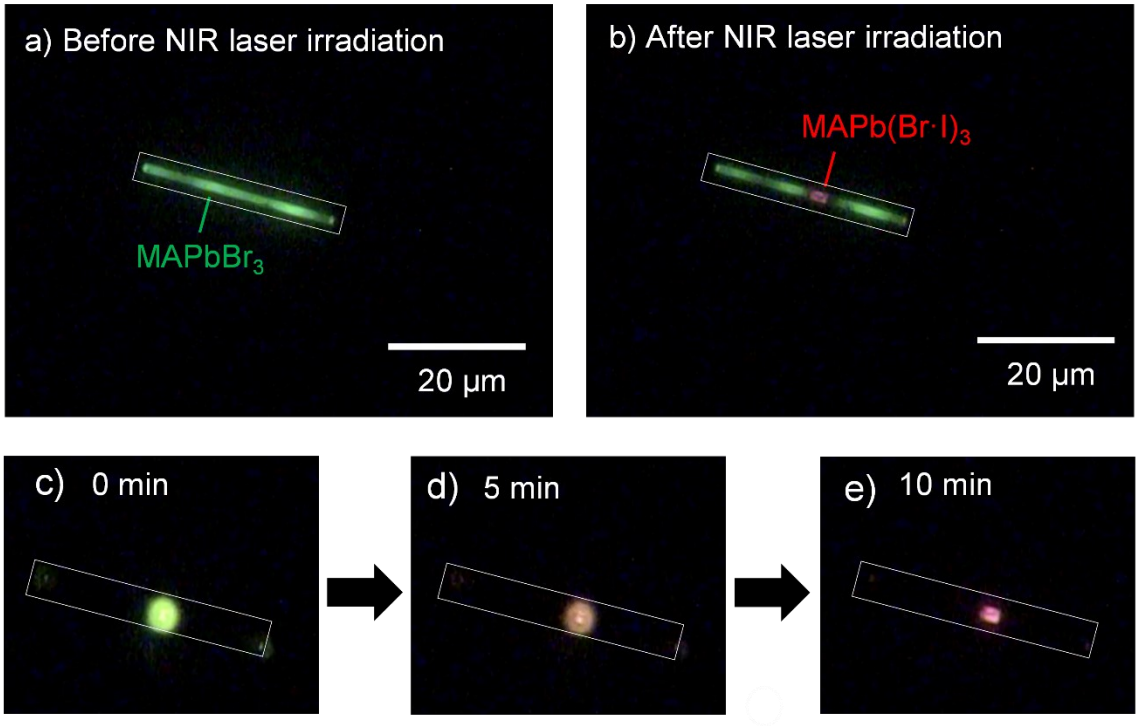

Figure 3.08: (a) PL image of the microrod crystal under UV laser irradiation before the exchange reaction. (b) PL image of the microrod crystal under UV laser irradiation after the halide exchange reaction. (c-e) Temporal changes in PL images at the focal volume under NIR laser irradiation at (c) 0 min, (d) 5 min, (e) 10 min.

As the reaction continued, the emission color of the irradiated part started changing. After 5 min of irradiation, I observed an orange-yellowish emission color from the focal spot. With further irradiation for 10 min, the emission color changed to red. After observing the red emission, the NIR laser was turned off and the crystal was illuminated again with a 405 nm laser. Under uniform illumination, it was observed that the laser-irradiated center part exclusively showed red emission while the two ends of the microrod retain their initial green emission. I consider that the focused laser irradiation induced bromide-to-iodide exchange reaction by increasing the local concentration of precursor solution and tuned the emission color selectively at the irradiated part of the microrod.

For quantitative analysis of the spatially-controlled halide exchange reaction under NIR laser irradiation, PL spectra from the irradiated center part were recorded at equal time intervals. I recorded the PL spectra after every 2 min (Figure 3.09). The initial PL maximum at the beginning of the reaction was measured at 545 nm. As the halide exchange reaction proceeds, the PL spectra also shifted towards a higher wavelength. This red shifted PL spectra continuously shifted upon the NIR laser irradiation. Finally, the PL maxima was

measured at 755 nm after 10 min. These changes of emission color and spectra allowed to consider that the laser-irradiated part of the initial $MAPbBr_3$ microrod changed to $MAPbBr_nI_{3-n}$ without any significant changes at the non-irradiated parts.

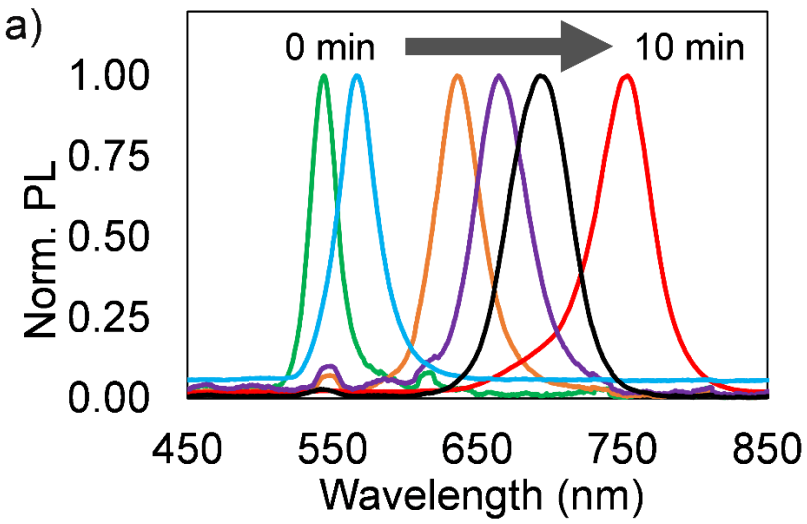

Figure 3.09: PL spectral change of the $MAPbBr_3$ microrod crystal under laser trapping.

3.2.4 The mechanism of the halide exchange reactions by laser trapping

The possible mechanism of the halide exchange reaction of the $MAPbBr_3$ microplates and microrods immersed in a MAI reaction solution is proposed here. I consider that due to the focused NIR laser irradiation the local concentration of the MAI reaction solution increases at the focal volume through laser trapping. Since the gradient force for an inhomogeneous electric field is proportional to the gradient of intensity and acts along the intensity gradient, the generated gradient force can be utilized to trap the MAI molecules in the direction of the light gradient. The applied optical force upon focused laser irradiation on a nanometre-sized object is expressed by the following equation[51]

$$\mathbf{F}(\mathbf{r}) = \frac{2\pi n_2 a^3}{c}\left\{\frac{\left(\frac{n_1}{n_2}\right)^2 - 1}{\left(\frac{n_1}{n_2}\right)^2 + 2}\right\}\nabla I(\mathbf{r})$$

where n_1 denotes refractive index of the target particle and n_2 is the refractive index of the surrounding medium, a is the particle radius, c is speed of the light in vacuum, and I is intensity of the laser.

The potential energy of the gradient force generated at the at the focus for a stable trapping is expressed as[51]

$$U = -\frac{2\pi n_2 a^3}{c}\left\{\frac{\left(\frac{n_1}{n_2}\right)^2 - 1}{\left(\frac{n_1}{n_2}\right)^2 + 2}\right\}\frac{2P}{\pi w_0^2}$$

where P is the power of the laser beam and w_0 is radius at the beam waist position. Here, the relationship between the applied optical force and the generated gradient force at the focal volume is considered as $\mathbf{F}(\mathbf{r}) = -\nabla U(\mathbf{r})$. A fundamental requirement for stable trapping of a particle is that the optical potential well of the generated gradient force should be sufficiently larger to suppress the Brownian motion of the object with the kinetic energy, k_BT, where k_B is the Boltzmann constant and T is the temperature of the surrounding medium. The optimum condition for stable trapping of a single object in the solution is $|U| \geq 10k_BT$. In the calculation, I used 1.531 as n_1 which was referred from the refractive index of methyl iodide and 0.5 nm as a which is the effective ionic radii of methylammonium ion[53] and iodide ion. From the experimental condition, I estimated, n_2 as 1.436, which was the refractive index of the medium,[52] laser power, P was 0.5 W, and w_0 = 375 nm. The calculation led to the relation $U \approx 0.0001k_BT$, which suggests the presence of MAI molecule clusters in the focal volume of the NIR laser.

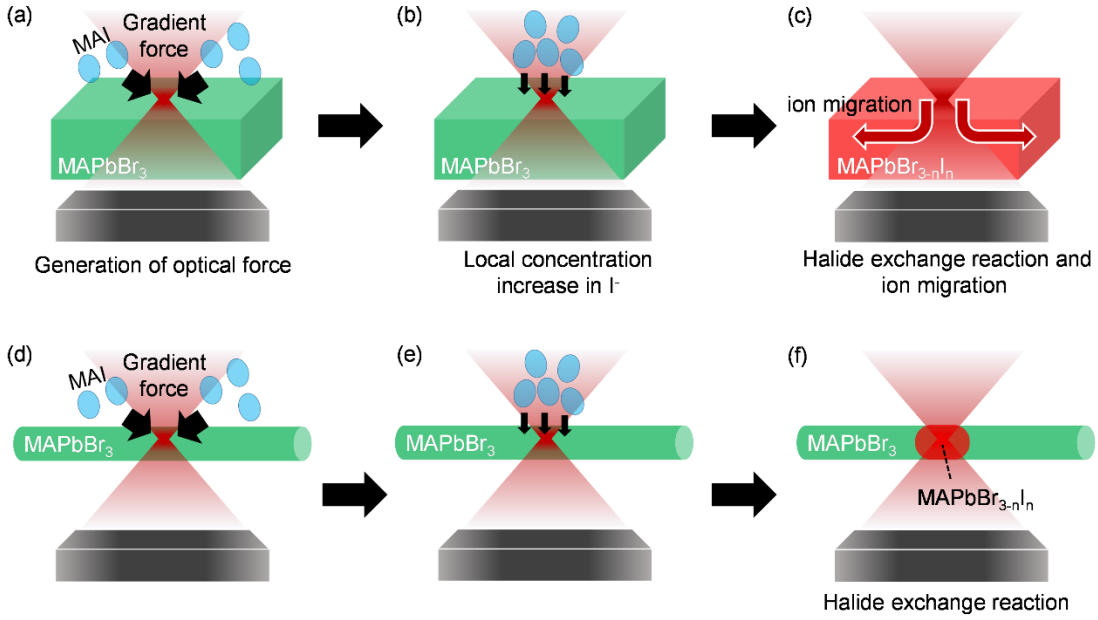

Figure 3.10: Mechanism of local halide exchange reaction by a focused laser beam. The local concentration of iodide ions is increased by optical force, and bromide to iodide exchange reaction is caused on (a–c) a microcrystal or (d, e) a microrod of $MAPbBr_3$. The bromide-to-iodide exchange reaction accompanies PL change from green to red for (c) the entire microcrystal or (f) the irradiated part of the large microplate or microrod.

Based on the above calculation it is considered that during laser trapping more than one MAI molecule comes to the focal spot through Brownian motion and remains there for a longer time. Compared to the isolated MAI molecule, a stronger optical force generated by the focused laser beam is applied to the groups of MAI molecule. Thus, the local concentration of MAI increases, and the halide exchange reaction takes place at the focal volume. The exchanged iodide ions can migrate inside the crystals via vacancy assisted diffusion mechanism due to the higher concentration of halide vacancies in the crystals. This halide diffusion also allows propagation of the exchange reaction from the surface to the bulk of the crystals along with the surroundings of the focal spot to some extent.

3.2.5 Photoinduced halide exchange in a $MAPbBr_3$ microrod crystal

The photoexcitation effect on halide exchange reaction was investigated by exciting the as-prepared microrod crystals with one-photon excitation. The exchange reaction was investigated under a low concentration of an MAI reaction (125 µM) solution used for the previous laser trapping experiments. I used a confocal laser beam from a 532 nm continuous-wave laser to irradiate the crystals. Figure 3.11a shows the PL image of the as-prepared $MAPbBr_3$ microrod crystal. Prior to the reaction, the as-prepared $MAPbBr_3$ microrod showed green emission from the whole area. Subsequently, the crystal was immersed in the MAI reaction solution and the center part of the crystal was irradiated for 10 min (Figure 3.11b). After the irradiation, the whole crystal was observed under 532 nm laser again. The irradiated

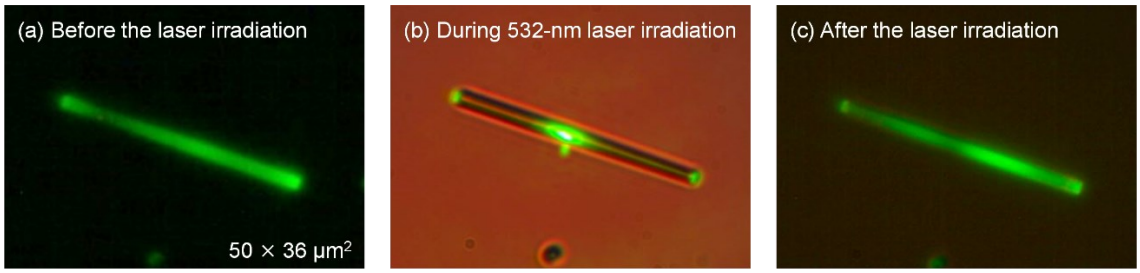

Figure 3.11: PL image of a $MAPbBr_3$ microrod under 532 nm UV laser irradiation (a) before the exchange reaction. (b) during the exchange reaction and (c) after the exchange reaction.

part of the crystal showed green emission as the initial crystal without any change in PL emission (Figure 3.11c). Under the current experimental conditions, photoinduced halide exchange by one-photon excitation is negligibly slow. Thus, without local concentration

increase in halide concentration by laser trapping any spatially-controlled exchange reaction is difficult to execute.

3.2.6 Stability of the halide exchanged part

The stability of the laser-induced halide exchanged part was observed under ambient condition. Following the same laser trapping technique center part of an as-synthesized $MAPbBr_3$ microrod was changed into iodide rich $MAPb(Br_n.I_{3-n})$ region (Figure 3.12a,b). After the exchange reaction, the microrod was excited with 405 nm laser at a different time interval to examine changes in the halide exchanged part. With time the PL images showed a gradual change in emission color at the exchanged part (Figure 3.12c-h). The intense red emission from the irradiated part gradually decreased and changed into a nonluminescent site after 150 min of irradiation which remain non-emitting even after 24 hours.

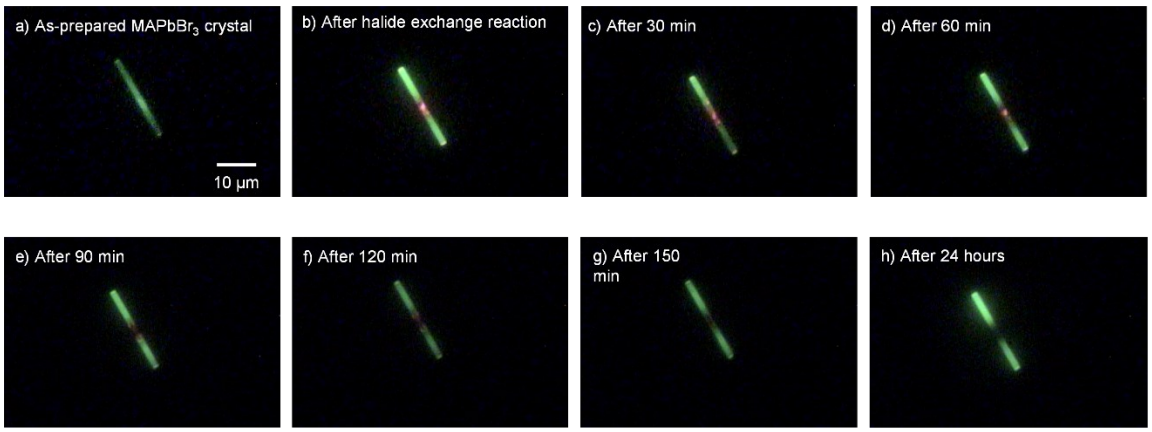

Figure 3.12: PL images of the microrod crystal under UV laser irradiation (a) before the exchange reaction. (b) after the halide exchange reaction. (c-h) Changes in PL emission of the exchanged part at different time intervals.

This phenomenon can be discussed from the viewpoint of halide diffusion in perovskite materials.[54] Here, the bromide-iodide halide interdiffusion facilitated the mixing of two distinct phases across the bandgap gradient heterostructure region. Thus, the subsequent mixing of two phases occurred through vacancy mediated diffusion mechanism. Also, the previous studies demonstrated the absence of PL emission in a certain wavelength range from a mixed halide perovskite composition. Due to the formation of such amorphous states via the mixing of halide ions, the laser-irradiated exchanged part may show no PL emission after a certain period.

3.3 Conclusions

In summary, I successfully demonstrated site-specific emission and bandgap tuning of the $MAPbBr_3$ microplate and microrod-shaped crystals. The changes of the emission color and spectra at the desired part was confirmed in a spatio-temporal manner under laser irradiation. The exchange reaction at the irradiated part suggests the proceedings of the reaction through local concentration increase induced by optical force. I excluded the possibility of photoinduced exchange reaction by irradiating the crystals with a confocal one-photon excitation. Also, subsequent mixing of the irradiated part and non-irradiated part was discussed through halide interdiffusion. Thus, the innovative laser-based halide exchange reaction offers new methodology for spatially-resolved bandgap tuning and enable control of the properties of perovskite materials by fabricating heterojunctions in perovskite materials.

3.4 References

1) Petrus, M. L.; Bein, T.; Dingemans, T. J.; Docampo, P. A Low Cost Azomethine-Based Hole Transporting Material for Perovskite Photovoltaics. *J. Mater. Chem. A* **2015**, 3, 12159–12162.

2) Saliba M., Matsui T., Seo J.-Y., Domanski K., Correa-Baena J.-P., Nazeeruddin M. K., Zakeeruddin S.M., Tress W., Abate A., Hagfeldt A., Grätzel M. Cesium containing triple cation perovskite solar cells: improved stability, reproducibility and high efficiency. Energy & Environmental *Science* **2016**, 9, 1989–1997.

3) Bertolazzi, S.; Krasnozhon, D.; Kis, A. Nonvolatile memory cells based on MoS2/graphene heterostructures. *ACS Nano* **2013**, 7, 3246−3252.

4) Gardner, N.; Müller, G.; Shen, Y.; Chen, G.; Watanabe, S.; Götz, W.; Krames, M. Blue-emitting InGaN−GaN double-heterostructure light-emitting diodes reaching maximum quantum efficiency above 200 A/ cm^2. *Appl. Phys. Lett*. **2007**, 91, 243506.

5) Kroemer, H. Heterostructure bipolar transistors and integrated circuits. *Proc. IEEE* **1982**, 70, 13−25.

6) Li, X.; Chen, W.; Zhang, S.; Wu, Z.; Wang, P.; Xu, Z.; Chen, H.; Yin, W.; Zhong, H.; Lin, S. 18.5% efficient graphene/GaAs van der Waals heterostructure solar cell. *Nano Energy* **2015**, 16, 310−319

7) Ko Y.-H., Jalalah M., Lee S.-J., Park J.-G. Super ultra-high-resolution liquid- crystal-display using perovskite quantum-dot functional color-filters. *Scientific Reports* **2018**, 8, 12881

8) Fang Y., Dong Q., Shao Y., Yuan Y., Huang, J. Highly narrowband perovskite single-crystal photodetectors enabled by surface-charge recombination. *Nature Photonics* **2015**, 9, 679–686.

9) Huang L., Gao Q., Sun L.-D., Dong H., Shi S., Cai T., Liao Q., Yan C.-H.

Composition-graded cesium lead halide perovskite nanowires with tunable dual color

lasing performance. *Advanced Materials* **2018**, 30, 1800596.

10) Dong Q., Fang Y., Shao Y., Mulligan P., Qiu J., Cao L., Huang J. Electron-hole diffusion lengths > 175 μm in solution-grown CH3NH3PbI3 single crystals. *Science* **2015**, 347, 967–970.

11) Chen D., Chen X. Luminescent perovskite quantum dots: synthesis, microstructures, optical properties, and applications. *Journal of Materials Chemistry C* **2019**, 7, 1413–1446.

12) Miyata A., Mitioglu A., Plochocka P., Portugall O., Wang J. T.-W., Stranks S. D., Snaith H. J., Nicholas R. J. Direct measurement of the exciton binding energy and effective masses for charge carriers in organic–inorganic tri-halide perovskites. *Nature Physics* **2015**, 11, 582–587.

13) Dequilettes D. W., Koch S., Burke S., Paranji R. K., Shropshire A. J., Ziffer M. E., Ginger D. S. Photoluminescence lifetimes exceeding 8 μs and quantum yields exceeding 30% in hybrid perovskite thin films by ligand passivation. *ACS Energy Letters* **2016**, 1, 438–444.

14) Wehrenfennig, C.; Eperon, G. E.; Johnston, M. B.; Snaith, H. J.; Herz, L. M. High charge carrier mobilities and lifetimes in organolead trihalide perovskites. *Adv. Mater.* **2014**, 26, 1584–1589.

15) Liu, F.; Zhang, Y.; Ding, C.; Kobayashi, S.; Izuishi, T.; Nakazawa, N.; Toyoda, T.; Ohta, T.; Hayase, S.; Minemoto, T.; Yoshino, K.; Dai, S.; Shen, Q. Highly luminescent phase-stable CsPbI3 perovskite quantum dots achieving near 100% absolute photoluminescence quantum yield. *ACS Nano* **2017**, 11, 10373–10383.

16) Castelli, I. E.; García-Lastra, J. M.; Thygesen, K. S.; Jacobsen, K. W. Bandgap Calculations and Trends of Organometal Halide Perovskites. *APL Mater*. **2014**, 2, 81514.

17) Wang, L.; Yuan, G. D.; Duan, R. F.; Huang, F.; Wei, T. B.; Liu, Z. Q.; Wang, J. X.; Li, J. M. Tunable Bandgap in Hybrid Perovskite CH3NH3Pb(Br3-yXy) Single Crystals and Photodetector Applications. *AIP Adv*. **2016**, 6, 45115.

18) Saliba, M.; Matsui, T.; Domanski, K.; Seo, J. Y.; Ummadisingu, A.; Zakeeruddin, S. M.; Correa-Baena, J. P.; Tress, W. R.; Abate, A.; Hagfeldt, A. Incorporation of Rubidium

Cations into Perovskite Solar Cells Improves Photovoltaic Performance. *Science* **2016**, 354, 206−209.

19) Saliba, M.; Matsui, T.; Seo, J. Y.; Domanski, K.; Correa-Baena, J. P.; Nazeeruddin, M. K.; Zakeeruddin, S. M.; Tress, W.; Abate, A.; Hagfeldt, A. Cesium-Containing Triple Cation Perovskite Solar Cells: Improved Stability, Reproducibility and High Efficiency. *Energy Environ. Sci*. **2016**, 9, 1989−1997.

20) Matsui, T.; Yokoyama, T.; Negami, T.; Sekiguchi, T.; Saliba, M.; Gratzel, M.; Segawa, H. Effect of Rubidium for Thermal Stability of¨Triple-Cation Perovskite Solar Cells. *Chem. Lett*. **2018**, 47, 814−816.

21) Choi H, Jeong J, Kim H-B, Kim S, Walker B, Kim G-H, Cesium-doped methylammonium lead iodide perovskite light absorber for hybrid solar cells. *Nano Energy* **2014**, 7:80–5.

22) Albadri A, Yadav P, Alotaibi M, Arora N, Alyamani A, Albrithen H, et al. Unravelling the impact of rubidium incorporation on the transport-recombination mechanisms in highly efficient perovskite solar cells by small-perturbation techniques. *J Phys Chem C* **2017**, 121, 24903–8

23) Kamat PV, Bisquert J, Buriak J. Lead-free perovskite solar cells. *ACS Energy Lett* **2017**, 2:904–5.

24) Jacobsson TJ, Pazoki M, Hagfeldt A, Edvinsson T. Goldschmidt's rules and strontium replacement in lead halogen perovskite solar cells: theory and preliminary experiments on $CH_3NH_3SrI_3$. *J Phys Chem C* **2015**, 119:25673–83.

25) Hebig J-C, Kühn I, Flohre J, Kirchartz T. Optoelectronic properties of $(CH_3NH_3)3Sb_2I_9$ thin films for photovoltaic applications. *ACS Energy Lett* **2016**, 1:309–14.

26) Saparov B, Hong F, Sun J-P, Duan H-S, Meng W, Cameron S, et al. Thin-film preparation and characterization of $Cs_3Sb_2I_9$: a lead-free layered perovskite semiconductor. *Chem Mater* **2015**, 27:5622–32.

27) Park B-W, Philippe B, Zhang X, Rensmo H, Boschloo G, Johansson EMJ. Bismuth based hybrid perovskites $A_3Bi_2I_9$ (A: methylammonium or cesium) for solar

cell application. *Adv Mater* **2015**, 27:6806–13.

28) Jang D. M., Park K., Kim D. H., Park J., Shojaei F., Kang H. S., Ahn J. P., Lee J. W., Song J. K. Reversible halide exchange reaction of organometal trihalide perovskite colloidal nanocrystals for full-range band gap tuning. *Nano Lett.* **2015**, 15, 5191–5199.

29) Akkerman Q. A., D'Innocenzo V., Accornero S., Scarpellini A.Petrozza, A., Prato M., Manna L. Tuning the optical properties of cesium lead halide perovskite nanocrystals by anion exchange reactions. *J. Am. Chem. Soc*. **2015**, 137, 10276−10281.

30) Nedelcu G., Protesescu L., Yakunin S., Bodnarchuk M. I., Grotevent M. J., Kovalenko M. V. Fast anion-exchange in highly luminescent nanocrystals of cesium lead halide perovskites ($CsPbX_3$, X = Cl, Br, I). *Nano Letters* **2015**, 15, 5635–5640.

31) Levchuk I., Osvet A., Tang X., Brandl M., Perea J. D., Hoegl F., Matt G. J., Hock R., Batentschuk M., Brabec C. J. Brightly luminescent and color-tunable formamidinium lead halide perovskite $FAPbX_3$ (X = Cl, Br, I) colloidal nanocrystals. *Nano Lett.* **2017**,*17*,2765–2770

32) Zhang F., Zhong H., Chen C., Wu X.-g., Hu X., Huang H., Han J., Zou B., Dong Y. Brightly luminescent and color-tunable colloidal $CH_3NH_3PbX_3$ (X = Br, I, Cl) quantum dots: potential alternatives for display technology. *ACS Nano* **2015**, 9 , 4533− 4542

33) Parobek D., Dong Y., Qiao T., Rossi D., Son D. H. Photoinduced anion exchange in cesium lead halide perovskite nanocrystals. *J. Am. Chem. Soc*. **2017**, 139, 4358–4361.

34) Zhang D., Yang Y., Bekenstein Y., Yu Y., Gibson N. A., Wong A. B., Eaton S. W., Kornienko N., Kong Q., Lai M., Alivisatos A. P., Leone S. R., Yang P. Synthesis of composition tunable and highly luminescent cesium lead halide nanowires through anion-exchange reactions. *J. Am. Chem. Soc*. **2016**, 138, 7236–7239.

35) Karimata I., Kobori Y., Tachikawa T. Direct observation of charge collection at nanometer-scale iodide-rich perovskites during halide exchange reaction on $CH_3NH_3PbBr_3$. *The Journal of Physical Chemistry Letters* **2017**, 8, 1724–1728

36) Dou L., Lai M., Kley C. S., Yang Y., Bischak C. G., Zhang D., Eaton S. W.,Ginsberg N. S., Yang P. Spatially resolved multicolor $CsPbX_3$ nanowire heterojunctions via anion exchange. *PNAS*, **2017**, 114, 7216–7221.

37) Ashkin A. Acceleration and trapping of particles by radiation pressure. *Physical Review Letters* **1970**, 24, 156–159.

38) Ashkin A., Dziedzic J. M. Optical trapping and manipulation of viruses and bacteria. *Science* **1987**, 235, 1517–1520.

39) Ashkin A., Dziedzic J. M., Yamane T. Optical trapping and manipulation of single cells using infrared laser beams. *Nature* **1987**, 330, 769–771.

40) Ashkin A., Schütze K., Dziedzic J. M., Euteneuer U., Schliwa M. Force generation of organelle transport measured in vivo by an infrared laser trap. *Nature* **1990**, 348, 346–348.

41) Ito S., Yoshikawa H., Masuhara H. Laser manipulation and fixation of single gold nanoparticles in solution at room temperature. *Applied Physics Letters* **2002**, 80, 482–484.

42) Pan L., Ishikawa A., Tamai N. Detection of optical trapping of CdTe quantum dots by two-photon-induced luminescence. *Physical Review B* **2007**, 75, 161305.

43) Singer W., Nieminen T. A., Heckenberg N. R., Rubinsztein-Dunlop H. Collecting single molecules with conventional optical tweezers. *Physical Review E* **2007**, 75, 011916.

44) Tsuboi Y., Shoji T., Nishino M., Masuda S., Ishimori K., Kitamura N. Optical manipulation of proteins in aqueous solution. *Applied Surface Science* **2009**, 255, 9906–9908.

45) Tsuboi Y., Shoji T., Kitamura N. Optical trapping of amino acids in aqueous solutions. *The Jounral of Physical Chemistry C* **2010**, 114, 5589–5593.

46) Hosokawa C., Yoshikawa H., Masuhara H. Optical assembling dynamics of individual polymer nanospheres investigated by single-particle fluorescence detection. *Physical Review E* **2004**, 70, 061410.

47) Yoshikawa H., Matsui T., Masuhara H. Reversible assembly of gold nanoparticles confined in an optical microcage. *Physical Review E* **2004**, 70, 061406.

48) Sugiyama T., Adachi T., Masuhara H. Crystallization of glycine by photon pressure of a focused CW laser beam. *Chemistry Letters* **2007**, 36, 1480–1481.

49) Sugioka K., Brown M. S., Arnold C.B. Laser Precision Microfabrication *Springer Series in Materials Science* **2010**, 135.

50) He C., Zha G., Deng C., An Y., Mao R., Liu Y., Lu Y., Chen Z., Refractive index dispersion of organic−inorganic hybrid halide perovskite $CH_3NH_3PbX_3$ (X = Cl, Br, I) single crystals. Cryst. *Res. Technol*. **2019**, 54, 1900011

51) Harada Y., Asakura T., Radiation Forces on a Dielectric Sphere in the Rayleigh Scattering Regime. *Opt. Commun.* **1996**, 124, 529−541.

52) Camin D. L., Forziati A. F., Rossini F. D. Physical Properties of n-Hexadecane, n-Decylcyclopentane, n-Decylcyclohexane, 1-Hexadecene and n-Decylbenzene. J. *Phys. Chem.* **1954**, 58, 440−442.

53) Park N.-G., Perovskite Solar Cells: An Emerging Photovoltaic Technology. *Mater. Today* **2015**, 18, 65−72.

54) Lai M., Obliger A., Lu D. Kley C. S., Bischak C. G., Kong Q., Lei T., Dou L., Ginsberg N. S., Limmer D. T., Yang P. Intrinsic anion diffusivity in lead halide perovskites is facilitated by a soft lattice *PNAS* **2018**, 115, 11929–11934.

Chapter 4

Optically controlled site-specific halide vacancy filling in perovskite microcrystals

The remarkable optoelectronic properties of halide perovskite materials made them promising for the next generation optoelectronic and photovoltaic devices. The wide-bandgap perovskite materials are being readily used in solar cells, LEDs, and lasers because of their facile tunability. However, the stability and performance of these solution-processed perovskite materials is firmly governed by the density of defects such as halide vacancies. On the other hand, the bandgap of these materials is tuned by post-synthesis halide exchange reaction which proceeds through the vacancy-assisted diffusion mechanism. This chapter discusses the suppression of halide exchange reaction by optically-controlled site-specific halide vacancy filling of the $MAPbBr_3$ microcrystals. The spontaneous halide exchange reaction of an as-grown $MAPbBr_3$ crystal in an MAI reaction solution occurs homogeneously in the entire region, which can be suppressed by treating the crystals with a MABr reaction solution. The MABr treatment reduces the halide vacancies of the initial crystals and inhibit the halide exchange reaction in the entire region. I also demonstrated such halide exchange suppression at specific sites of the microrod crystals through vacancy filling using a NIR laser beam. The NIR laser irradiation fills the halide vacancies exclusively at the irradiated part, while the characteristic features of the nonirradiated parts remain unchanged. The corresponding photoluminescence spectra, scanning electron microscope images, and energy dispersive x-ray mapping confirm the halide vacancy filling of the $MAPbBr_3$ microcrystals. Furthermore, an increase in the PL lifetime at the irradiated part suggests the suppression of nonradiative recombination through vacancy filling.

4.1 Introduction

Lead halide perovskites have achieved revolutionary success in the present decade towards the fabrication of next-generation photovoltaic and optoelectronic devices such as solar cells, light emitting diodes, lasers, and sensors.[1-10] The remarkable progress of these materials benefits from the superior optoelectronic properties such as high absorption coefficient, long carrier diffusion length, high defect tolerance, the generation of free charges by photoexcitation, and high electron and hole mobilities.[11-18] Moreover, the synthesis of perovskite materials using abundant precursors and solution-based processability under low temperatures offers low-cost fabrication.[19,20] However, the solution-processed halide perovskites are of low quality due to an abundance of crystal defects which put a roadblock toward the improvement of device efficiency.[21-23] Various unpremeditated defects, including point defects, Schottky and Frenkel defects, grain boundaries, and dislocations can be originated during the crystallization of perovskite materials via precursor routes in a solution-cast process.[23-28] These defects serve as trap sites in these materials for both photogenerated electrons and holes, which finally induce nonradiative recombination. The nonradiative recombination creates a passage for combining the excess free carriers and shortens the steady-state charge carrier density. This unexpected route of recombination generated by defects limits the power conversion efficiency of perovskite solar cells to reach the predicted theoretical limit. Hence, a detailed study for understanding and characterizing these defects is essential to attain high performance and stability from the perovskite materials.

A considerable number of reports provided various theoretical and experimental techniques to calculate the formation energy and transition energy level of the defect densities and their effect on optoelectronic properties. The theoretical studies of defect states mainly stand on first-principle density functional theory (DFT) calculations.[29-34] For example, the most extensively studied lead halide-based perovskite material regarding defect physics is methylammonium lead iodide ($MAPbI_3$) because of its superior electronic structure. Various DFT approaches like hybrid-functional, exchange-correlation function or semilocal functional calculation revealed the energy levels of structural defects made up of MA^+ and I^- vacancies in the $MAPbI_3$ material.[31] On the other hand, several experimental strategies such as space-charge limited current (SCLC), time-resolved photoluminescence spectroscopy (TRPS), confocal fluorescence microscopy (CFM), thermal admittance spectroscopy (TAS), photothermal deflection spectroscopy (PDS), and atomic force

microscopy (AFM) based scanning probe techniques have been employed to study the defect concentration and defect distribution in perovskites.[36-40] SCLC method is one of the straightforward methods to measure the defect density where the filled traps are estimated as a function of applied voltage. An approximate value of defect density 10^{17}-10^{19} m^{-3} was measured by this technique in a polycrystalline perovskite thin film.[38] TRPS and CFM are also often used methods to determine the defects as these PL measurements have a strong interdependence with the nonradiative trap states. A steady-state PL intensity increase or decrease mostly depends on the density of defects which results from the reduction or enhancement of trap states. Also, the PL mapping of a particular domain by CFM can probe the defects. For example, Dequiletters et al.[39] used the CFM technique and observed an increase in PL intensity and lifetime in $MAPbI_3$ films under continuous light illumination. Furthermore, different electronic states in the defects arise variations in the local conductivity which is recognized through conductive-AFM. Also, Yun et al.[36] reported a local contact potential difference map under an applied bias using the kelvin-AFM technique to explore the surface and grain boundary defects. Moreover, low temperature STM was conducted by Ohmann et al.[37] on the $MAPbBr_3$ crystals which estimated 10 defects/100 nm^2. Such high defect density underscores the importance of defect passivation in perovskite materials to enhance the stability and performance of perovskite-based devices.

To overcome the limitations of perovskite materials on device performance and enhance the radiative recombination rates originated by defects, many thriving attempts have been taken to defect engineering by removing or filling trap states in perovskite materials. Different defect passivation strategies, including stoichiometry control, lewis acids, and bases, cations, and anions are reported to passivate the defects of perovskite materials.[41-46] For example, Cho et al.[41] fabricated the $MAPbBr_3$ films with an excess amount of MABr (MABr: $PbBr_2$= 1.05:1) which gives an increased PL intensity and photoluminescence quantum yield (PLQY) than those prepared by the stoichiometric reaction. Similarly, a $CsPbBr_3$ film prepared with higher CsBr ratio exhibited an improved PL intensity and PLQY by decreasing the Br vacancies. Lewis bases such as carbonyl, hydroxyl, carboxyl, and amine derivatives are frequently used to passivate the defects by donating electrons. For example, amine derivatives were used by Lee et al.[42] for filling the Br vacancies of $MAPbBr_3$ film surface and improving the optical properties. Also, Fullerene derivatives are found to be the potential Lewis acids for passivating the electron-

rich defects. Shao et al.[44] first utilized the fullerene functionalized phenyl butyric acid methyl ester to lessen both the deep and shallow traps. Moreover, several cationic and anionic species have been involved in passivating the defects of perovskite materials.[47-49] For example, metal ion NA+ was found to passivate the MA vacancies by diffusing into the grain boundaries.[47] Similarly, Abdi-Jelebi et al.[49] used potassium iodide as a passivating material in a mixed halide perovskite precursor and found an improved PLQY upto 95%. Besides the cationic passivating materials, anions in the form of $PbCl_2$, MAI, FACl, MABr and MACl have been reported to compensate the halide vacancies of perovskite materials. As an example, Saidaminov et al.[48] successfully incorporated Cl^- ion into a $CsMAFAPbI_{2.55}Br_{0.45}$ perovskite film and observed a superoxide generation and increased stability, which confirms the reduced defect density by Cl^- incorporation.

In general, the halide exchange reaction is induced by exposing perovskite crystals to the solution containing reactant halide ions, and the bandgap is homogeneously varied in the crystal which proceeds by the migration of halides through halide vacancies. In this chapter, I demonstrated the suppressions of halide exchange reaction by filling the halide vacancies via optically-controlled reaction. The spontaneous halide exchange reaction of the $MAPbBr_3$ crystals was homogeneously induced in the reaction solution of MAI. Chemically, the reaction was suppressed by filling the halide vacancies of the as-grown $MAPbBr_3$ crystals with a MABr solution before the addition of an MAI solution. On the other hand, these halide vacancies were filled at a specific site of the $MAPbBr_3$ crystals by optical trapping with the use of a focused near-infrared (NIR) laser beam.

4.2 Results and discussions

4.2.1 Chemically controlled halide vacancy filling

A facile experimental procedure was developed for the spontaneous halide exchange reaction and the suppression of halide exchange through vacancy filling on the as-prepared $MAPbBr_3$ microrods as illustrated schematically in figure 4.01. Microcrystals (plate and rod-shaped) of $MAPbBr_3$ were prepared by spontaneous solvent evaporation technique in the following process.[50,51] For preparing the plate and rod-shaped $MAPbBr_3$ crystals, solid precursor salts MABr and $PbBr_2$ were dissolved in DMF solution in a 1:1 stoichiometric ratio. The concentration of the precursor solution was 1.3 M which was mixed with a GBL solution in 1:1 ratio to attain an unsaturated solution. Subsequently, 1 μL of the supernatant from the mixed solution was taken on a clean coverslip inside a home-built silicone chamber. Spontaneous crystallization of the $MAPbBr_3$ crystals with different sizes and

shapes started growing inside the solution droplet. Through natural solvent evaporation, the crystals further grow. After confirming the desired size under a microscope, the remaining solution was removed by wiping with filter paper to limit the growth of crystals.

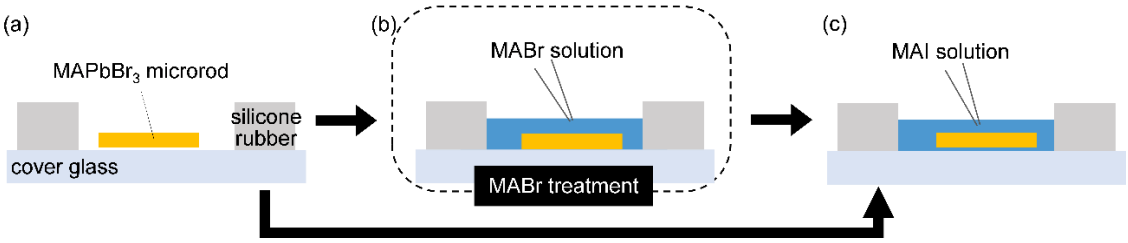

Figure 4.01: A scheme of the experimental procedures for spontaneous halide exchange reaction and suppression of exchange reaction by halide vacancy filling.

However, after the synthesis, the as-prepared crystals were immersed in a reaction solution of MAI (375 µM) to induce bromide-to-iodide exchange reaction (Figure 4.01a,c). Again, the spontaneous exchange reaction was suppressed homogeneously in the whole crystal by treating the prepared crystals with a MABr reaction solution (375 µM) and then immersed in an MAI solution (Figure 4.01a-c) to examine the halide exchange reaction. The MABr and MAI reaction solutions were prepared by dissolving MABr and MAI precursor salts in isopropyl alcohol followed by mixing with 1-hexadecene in a 1:100 ratio to obtain the final concentration.

The spontaneous halide exchange reaction was observed by illuminating the as-grown $MAPbBr_3$ microrod crystals with a 405 nm laser. The PL images of the crystals were recorded before and after immersing the microrods in an MAI solution. Prior to the exchange reaction, upon wide-field excitation, an as-prepared $MAPbBr_3$ microrod showed bright green emission from the whole area of the crystal (Figure 4.02a). This green emission is one of the characteristic features of the $MAPbBr_3$ crystals, which results from the band-to-band transition. After that, the reaction solution MAI was added to the sample chamber to initiate the halide exchange reaction. In the MAI solution, the green emission of the $MAPbBr_3$ microrod started changing within minutes and gradually changed fully to red emission within 5 min. (Figure 4.02b). The change in emission color is due to the formation of resultant $MAPb(Br.I)_3$, which occurred by the halide exchange reaction between the iodide ions in the solution and bromide ions in the crystal.

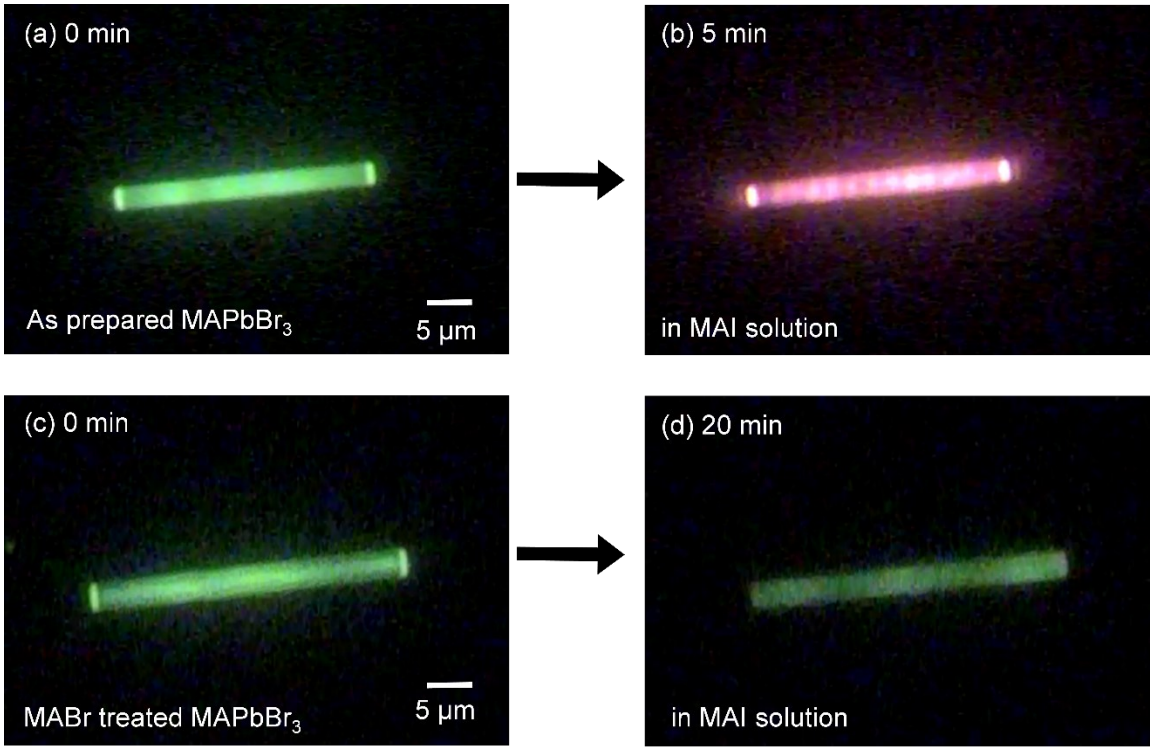

Figure 4.02: PL images of (a) an as-prepared $MAPbBr_3$ microrod before the halide exchange reaction, (b) the microrod in an MAI reaction solution after the halide exchange reaction, (c) a MABr treated $MAPbBr_3$ microrod before immersing in MAI reaction solution, and (d) the microrod in an MAI reaction solution after 20 min of incubation.

The role of halide vacancies on the exchange reaction was evaluated by treating the as-prepared crystals with MABr reaction solution. An as-prepared crystal was immersed in 40 μL of MABr solution for 5 min to fill the Br vacancies, and then the MABr solution was removed. Figure 4.02c represents a MABr treated $MAPbBr_3$ microrod crystal. Consequently, the microrod was immersed in a MAI solution to examine the spontaneous exchange reaction. In case of Figure 4.02a,b the microrod changed its initial green emission completely into red, but interestingly, the green emissive MABr treated microrod remained green emissive in the MAI solution (Figure 4.02d). Moreover, the MABr treated microrod was investigated for 20 min, but no change in emission color was observed.

To evaluate the role of halide vacancies on the spontaneous exchange reaction quantitatively, I measured the PL spectra of the microrods before and after incubating it in the constituent halide precursors. In case of the spontaneous halide exchange reaction, the $MAPbBr_3$ microrod showed an emission peak at 545 nm (Figure 4.03a) which agrees well with the reported value.[52] After the halide exchange reaction in an MAI reaction solution,

a redshifted PL maximum was found at 740 nm (Figure 4.03a). The formation of $MAPb(Br.I)_3$ with different halide ion compositions from $MAPbBr_3$ microrod is responsible for the broad PL spectrum. Thus, the PL spectral measurement along with the emission color change confirms the spontaneous halide exchange reaction. Again, the PL spectral measurements were also performed during the suppression of the exchange reaction. First, The PL spectra was measured before and after treating the microrod with MABr reaction solution (Figure 4.03b). The initial PL

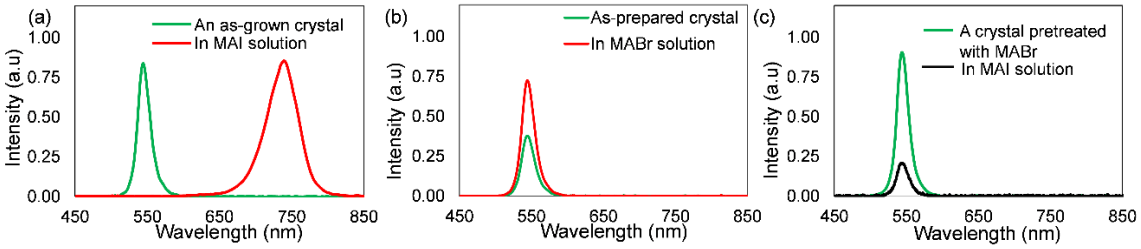

Figure 4.03: PL spectra of (a) an as-prepared $MAPbBr_3$ microrod before the halide exchange reaction and the microrod in an MAI reaction solution after the halide exchange reaction, (b) an initial $MAPbBr_3$ microrod and after treating with MABr reaction solution, and (c) a crystal pretreated with MABr solution and in an MAI reaction solution after 20 min of incubation.

intensity of the as-prepared microrod increased after the MABr treatment which is due to the decrease in trap sites through halide vacancy filling. After treating, the microrod was immersed in MAI for 20 min where I didn't observe any spectral change except a decrease in PL intensity (Figure 4.03c). These spectroscopic analyses and intact emission color imply the suppression of spontaneous halide exchange reactions by vacancy filling. However, the decrease in PL intensity can be discussed from the following band energy alignments.[53] The low PL intensity during the reaction resulted from the generation of low iodide composed $MAPb(Br.I)_3$ from pristine $MAPbBr_3$ crystal. When a $MAPbBr_3$ crystal is partly replaced by a small amount of iodide ions ($0 < x < 1$ in $MAPbBr_{3-x}I_x$), the energy difference between the conduction bands of $MAPbBr_{3-x}I_x$ and $MAPbBr_3$ become comparable to the room-temperature thermal energy which is 0.025 eV. Contrarily, the large valance band energy gaps between them occupy the photogenerated holes in the iodide-rich domain. These unique band structures allow the photogenerated electrons to be delocalized between the conduction bands of $MAPbBr_{3-x}I_x$ and $MAPbBr_3$ regions and limit the recombination with the trapped holes localized in $MAPbBr_{3-x}I_x$ domains. Thus, the

crystal structure with smaller x values prevents the radiative recombination and quenches the PL emission. In addition, the photogenerated holes from $MAPbBr_3$ crystals are readily captured by the adsorbed iodide ions at the surface, which also possess the PL quenching.

I also recorded the scanning electron microscopy (SEM) images and energy dispersive X-ray (EDX) images to examine the vacancy filling of the prepared crystals by bromide ions. First, the SEM and EDX images of an as-prepared microrod was measured. Figure 4.04a-c shows the SEM image and the corresponding EDX elemental map of an as-prepared $MAPbBr_3$ microrod. The EDX elemental mapping shows the distribution of Br and Pb elements of the prepared microrod. Later, the microrod was treated with MABr by immersing it in a MABr reaction solution of the same concentration used for the aforementioned vacancy filling experiment.

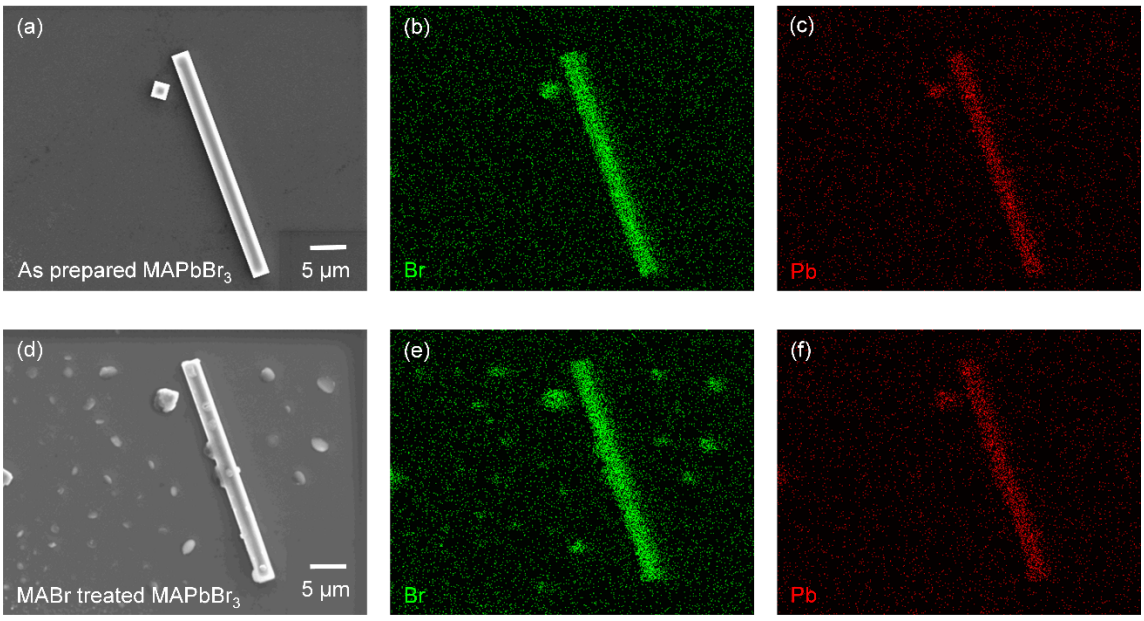

Figure 4.04: SEM images of the as-grown $MAPbBr_3$ microrod (a) before and (d) after treating with a MABr solution. EDX elemental mapping of Br and Pb composition (b,c) before and (e,f) after treating with the MABr solution.

After treating the microrod with MABr, again, the SEM and EDX micrograph was taken. Figure 4.04d-f shows the SEM image and corresponding EDX elemental mapping of the $MAPbBr_3$ microrod after treating with MABr. The EDX images clearly show an increase in Br composition after the vacancy filling. The Br composition of the microrod increased by 9% after immersing in the MABr reaction solution, which also confirms the vacancy filling. An unusual deformation of the microrod was observed from the SEM image after

the vacancy filling reaction, which may result because of drying up the crystal after MABr treatment.

I further investigated the suppression of the spontaneous halide exchange reaction of the plate-shaped $MAPbBr_3$ crystals. Following the same experimental route, the $MAPbBr_3$ microplates were also immersed in an MAI reaction solution to induce the Br-to-I exchange reaction. Similar to the microrod crystals, the microplate crystals also showed spontaneous exchange reaction, and the initial green emission color of the crystal gradually changed to red emission after 10 minutes (Figure 4.05a,b).

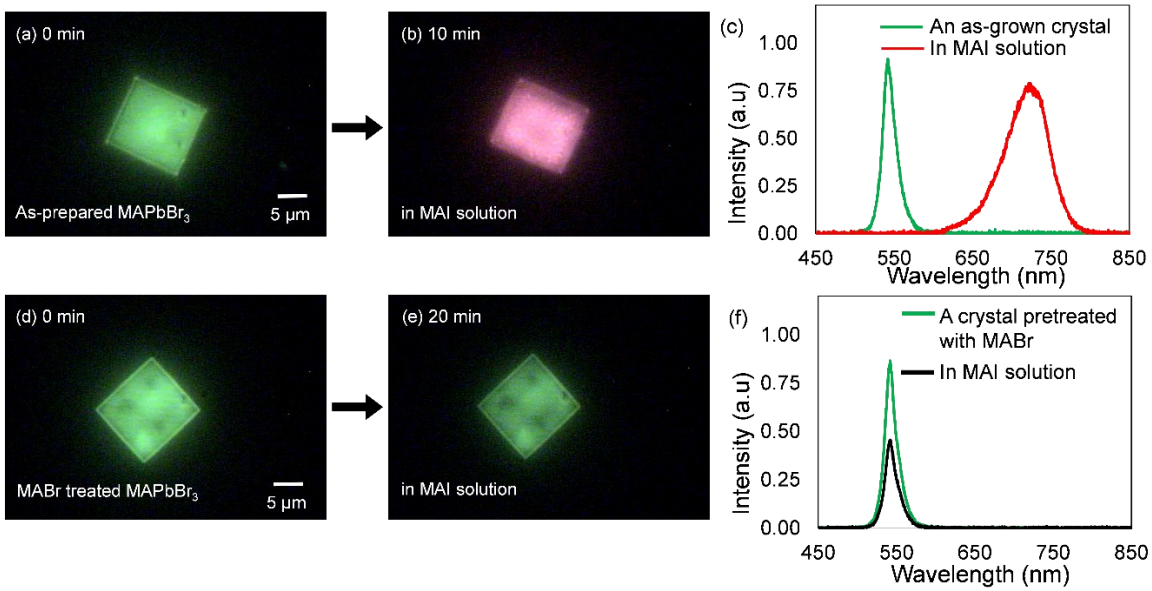

Figure 4.05: PL images and PL spectra of (a,c) an as-prepared $MAPbBr_3$ microplate before the halide exchange reaction, (b,c) the microplate in an MAI reaction solution after the halide exchange reaction, (d,f) a MABr treated $MAPbBr_3$ microplate before immersing in an MAI reaction solution, and (e,f) the microplate in an MAI reaction solution after 20 min of incubation.

Different from the case of microrods, microplate crystals took a longer time for the complete exchange. This phenomenon can be discussed from the viewpoint of crystal thickness. It is reported that the anion exchange reaction of different thickness crystals follows a similar tendency of reaction propagation pathway but with different rates.[54] Thus, depending on the crystal thickness, the time required for the halide exchange reaction vary from crystal to crystal. Along with the emission color change a redshifted PL spectrum from 545 nm to 735 nm also confirms the spontaneous halide exchange reaction (Figure

4.05c). However, to suppress the exchange reaction through vacancy filling, the microplate crystals were also pretreated with a MABr solution before immersing in the MAI solution. The emission color and spectrum of the MABr treated decrease in bandgap (Figure 4.05d-f). The above PL images, PL spectra and EDX mapping clearly confirm the inhibition of spontaneous halide exchange reaction of the rod and plate-shaped $MAPbBr_3$ crystals by Br vacancy filling when they are treated with a MABr reaction solution.

4.2.2 Optically controlled site-specific halide vacancy filling

The optically controlled halide vacancy filling at a specific position of the $MAPbBr_3$ crystals was performed by irradiating a tightly focused 1064 nm NIR laser beam. Similar to the halide exchange reaction at the specific sites through local concentration increase of precursor solution discussed in chapter 3, halide vacancy filling is also expected to take place at the irradiated sites through local concentration increase under NIR laser irradiation.[51] For this purpose, I prepared the $MAPbBr_3$ microrod in the silicone chamber and immersed it in a MABr reaction solution of 250 µM (Figure 4.06a (i, ii)). A lower concentration of a MABr reaction solution was selected to avoid the spontaneous halide vacancy filling by the higher concentration reaction solution. Immediately, after immersing the microrod in the reaction solution, the center part of the $MAPbBr_3$ microrod was irradiated by the focused laser beam. The center part was irradiated for 20 min, and then the laser was turned off. Afterward, the MABr solution was removed from the chamber, and finally, the crystal was immersed with an MAI reaction solution of 375 µM to investigate the Br-to-I halide exchange reaction(Figure 4.06a(iii)).

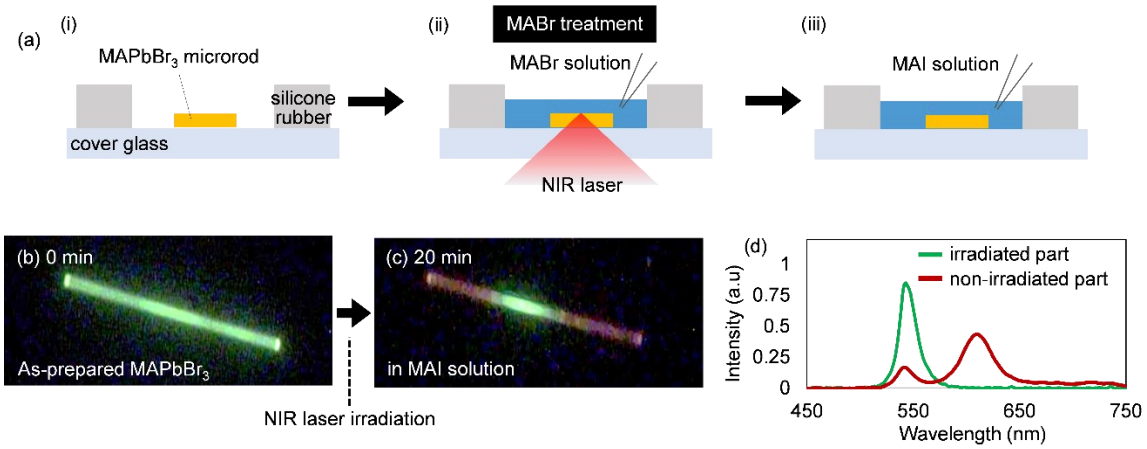

Figure 4.06: (a) A scheme for the laser induced vacancy filling experiment of a $MAPbBr_3$ microrod in a solution. PL images of (b) an as-prepared $MAPbBr_3$ microrod before starting

the exchange reaction, (c) the microrod in an MAI solution after irradiating the center area with the 1064 nm laser in the MABr solution, and (d) PL spectra from the irradiated area and nonirradiated area of the crystal incubated in an MAI reaction solution.

I recorded the PL images of the as-prepared $MAPbBr_3$ microrod before starting the reaction and after immersing in the MAI reaction solution. Figure 4.06b shows the PL micrograph of the initial microrod, which was green emissive in the whole area. After the laser irradiation, when the crystal was immersed in an MAI solution, it shows an exclusive green emission only at the central irradiated part. The emission color of the nonirradiated parts gradually changed into the red from its initial green emission(Figure 4.06c). The red emission from the nonirradiated parts was due to the halide exchange reaction which took place between the Br ions of the crystal and I ions from the reaction solution. However, the irradiated center part remained green emissive in the MAI solution because of the suppression of halide exchange by Br vacancy filling through laser irradiation. I also verified the role of halide vacancy filling by measuring the PL spectra from the laser-irradiated part and nonirradiated parts after the exchange reaction (Figure 4.06d). The irradiated center area showed one emission peak at 545 nm, which is same the as the as-prepared $MAPbBr_3$ crystals. On the other hand, the nonirradiated parts showed two distinct peaks at 545 nm and 615 nm. During the laser irradiation process, the spontaneous halide vacancy filling at the nonirradiated parts also occurred inevitably to some extent and formed mixed halide composition $MAPb(Br.I)_3$, which is responsible for such a bimodal emission spectrum. Thus, I consider that in the MABr solution, the focused laser irradiation fills the halide vacancies of the $MAPbBr_3$ crystal at the irradiated area and hinders the halide exchange reaction when immersed in an MAI solution.

To understand the site-specific vacancy filling reaction, I captured the of the two-photon excited PL images while irradiating with the focused laser beam. At the beginning of the reaction, the crystal showed a green emission of low intensity from the focal spot of the NIR laser. With time, the green emission from the focal spot gradually increased and reached to a highest after 20 min. (Figure 4.07a-c). To understand the vacancy filling reaction quantitatively, PL spectral changes were also recorded every 2 min under the two-photon excited irradiation. The initial PL maximum of the microrod was observed at 545 nm. As the reaction proceeds, the PL intensity also increased and became saturated within 20 min without any shifting of the PL maximum (Figure 4.07d). As the PL maximum was

observed at 545 nm, I plotted the PL intensity values at 545 nm as a function of time to show the increase in PL intensities during laser irradiation (Figure 4.07e).

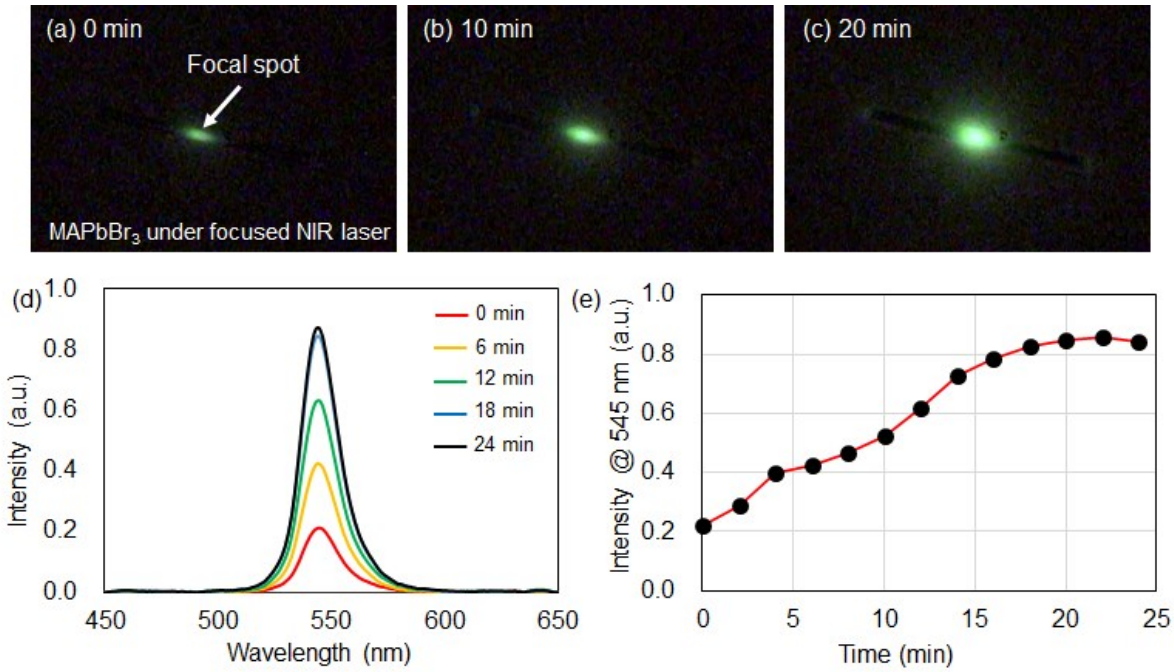

Figure 4.07: (a-c) PL emission images of the irradiated area under two-photon excitation at (a) 0 min, (b) 10 min, and (c) 20 min. (d) Two-photon excited PL spectra from the irradiated area at different times. (e) Increase of PL intensity at 545 nm as a function of equal time intervals.

For the representative microrod showed in Figure 4.07a the saturation point was achieved at around 20 min, which may differ from crystal to crystal depending on the defect densities in them.

Also, to examine the NIR laser irradiation effect on the crystals, I conducted the experiment under the same experimental condition using a pure solvent of 1-hexadecene/isopropyl alcohol (100:1) without any MABr solvent. In the case of the laser irradiation without any MABr there was no change in the PL intensity (Figure 4.08a). The PL intensity of the laser-irradiated part remains almost unchanged compared to the initial PL intensity. Moreover, after the laser irradiation with MABr reaction solution, the PL intensity from the nonirradiated part was also investigated. While the PL intensity of the

laser-irradiated part increased more than four times after irradiation, the PL intensity of the nonirradiated parts remains similar to the as-prepared crystal (Figure 4.08b).

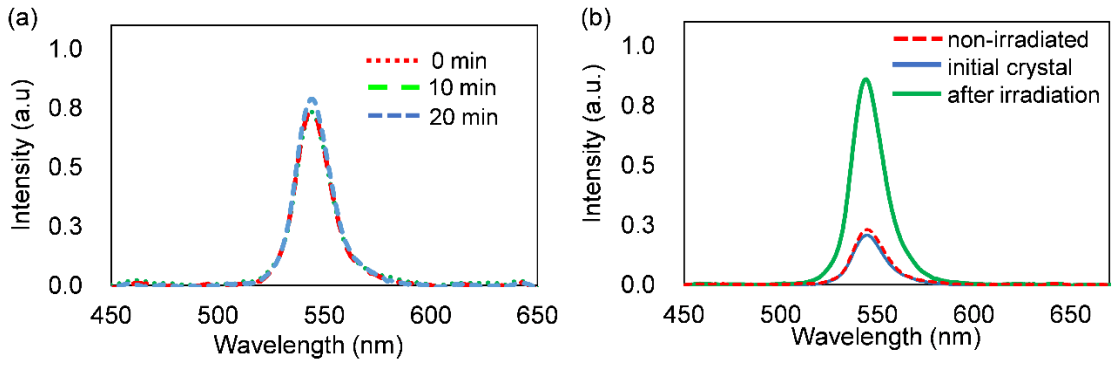

Figure 4.08: (a) PL spectra from the laser-irradiated area of a microrod without any MABr solution. (b) PL spectra from the irradiated area before, after the NIR laser irradiation and nonirradiated area

The time-resolved PL properties of the microrods were recorded before and after the MABr treatment to understand the relationship between the site-specific halide vacancy filling and nonradiative charge carrier recombination. The PL lifetimes of the microrods were studied from the laser-irradiated part and nonirradiated parts. The decay profile of the microrod showed different lifetime values from the irradiated and nonirradiated parts after the NIR laser irradiation. The average lifetime value of the laser-irradiated part increased to 23 ns while the PL lifetime was calculated 15 ns from the nonirradiated parts (Figure 4.09).

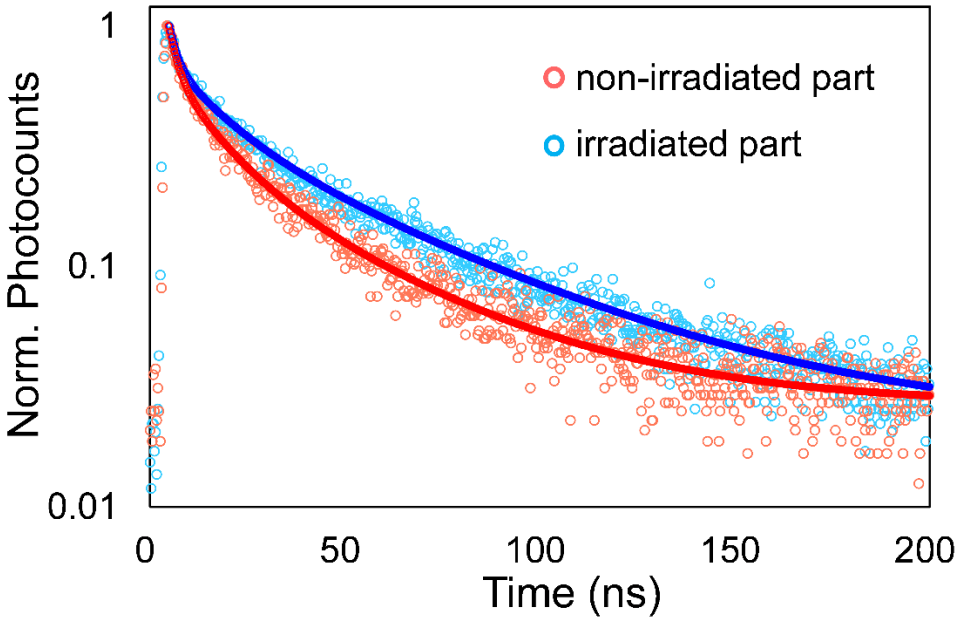

Figure 4.09: PL decay profiles of the $MAPbBr_3$ microrod measured from (a) the irradiated, and (b) a nonirradiated part.

However, the lifetime values were found different among rods both from the irradiated and nonirradiated parts. This difference in lifetime values attributes from the initial crystal quality where the defect concentrations are different among the crystals. Although the PL lifetime varied from crystal to crystal, I always found an increased lifetime value from the laser-irradiated parts compared to the nonirradiated parts. These results indicated that the density of halide vacancies was decreased at the irradiated part of the microrods and minimized the nonradiative charge carrier recombination, which results in the inhibition of halide exchange reaction in a spatially controlled manner.

4.2.3 The mechanism of the halide vacancy filling

Here, I summarized the underlying mechanism of the suppression dynamics of halide exchange reaction of the $MAPbBr_3$ microrod crystals. Generally, a solution-processed $MAPbBr_3$ microrod consists of a lot of halide vacancies. Upon excitation, these halide vacancies act as the trap sites for the photogenerated electrons and recombine nonradiatively. On the other hand, when the microrod is immersed in an MAI reaction solution, a spontaneous Br-to-I halide exchange reaction takes place. (Figure 4.10a) The halide exchange reaction first takes place rapidly at the crystal surface and then diffuses inside the crystal via the halide vacancy-assisted diffusion mechanism.[55,56] Again, when the

$MAPbBr_3$ microrod is treated with a MABr solution, the halide vacancies are filled with the bromide ions and increases the crystal quality.

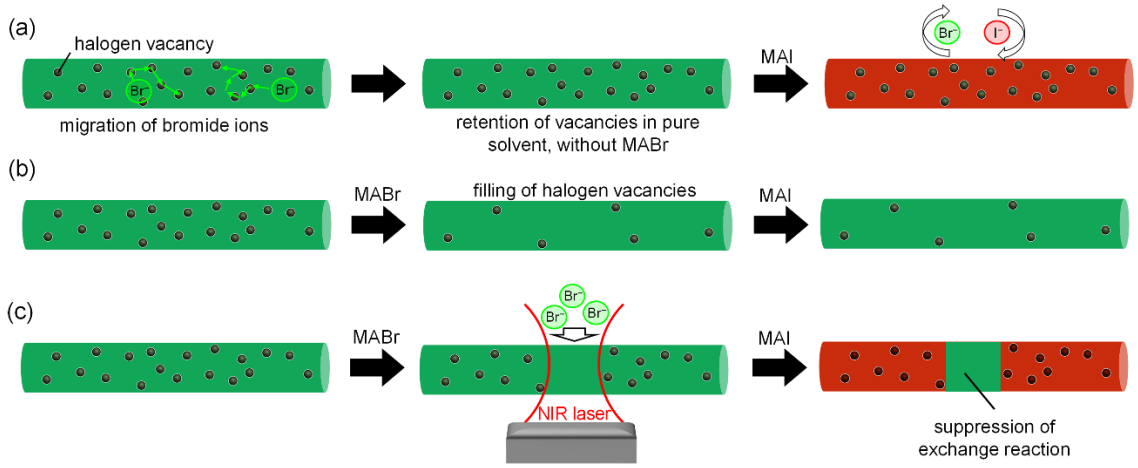

Figure 4.10: Schematic representation of the chemically and optically controlled halide exchange suppression by vacancy filling in $MAPbBr_3$ microrods. (a) An as-prepared microrod immersed in pure solvent without MABr and then in MAI. (b) A microrod immersed in MABr and then in MAI solution. (c) A microrod irradiated at the center in MABr solution and then immersed in MAI solution

Thus, after the MABr treatment, the PL intensity is enhanced, and PL lifetime becomes longer. The halide vacancy filling also limits the diffusion of ions inside the bulk of the crystal, which results in suppression of halide exchange reaction upon incubating in MAI solution (Figure 4.10b). Such vacancy filling is optically controlled at a specific site of the $MAPbBr_3$ microrods using a focused NIR laser beam. The bromide vacancy filling is induced only at the irradiated part in a MABr solution and inhibits the Br-to-I exchange reaction while the nonirradiated parts change through halide exchange reaction (Figure 4.10c). In the previous chapter, I discussed the NIR laser-induced halide exchange reaction at a specific site of the crystals through the local concentration increase of the reactive precursors.[51] Similarly, I consider that the focused NIR laser irradiation efficiently fills the bromide vacancies in the irradiated part by concentrating the precursor solution at the focal volume. Since the inception of laser trapping using a gradient force by Ashkin et al[57], this universal trapping tool is being widely used in the field of chemistry for nanoparticles patterning, compounds crystallization, and controlling phase transition or separation spatiotemporally.[58-62] I consider that the strong optical force generated by the NIR laser beam concentrates a group of precursors at the focal spot, which remains there and fills the

halide vacancies. The halide vacancy filling thus leads to the inhibition of exchange reaction spatially at the irradiated part.

4.3 Conclusions

In summary, I studied the role of halide vacancies on the halide exchange reaction of $MAPbBr_3$ microrod and microplate-shaped crystals. In the beginning, I demonstrated the spontaneous halide exchange reaction of a $MAPbBr_3$ microrod which progresses through a vacancy-assisted diffusion mechanism upon exposure to a reactive reaction solution. The spontaneous halide exchange reaction was suppressed homogeneously in the whole crystal by treating the as-prepared $MAPbBr_3$ microrod with a MABr solution. The PL emission and spectral change confirmed the suppression of halide exchange reaction through the chemical process. Also, the SEM images and elemental mapping by EDX further confirmed the halide vacancy filling of the $MAPbBr_3$ microrods. I further extended the vacancy filling study in the plate-shaped $MAPbBr_3$ crystals, which followed a similar trend of changes as microrod crystals. Furthermore, I successfully controlled the halide exchange reaction at a specific area of the microrods through vacancy filling using a NIR laser beam. I investigated the reaction progress under the two-photon excitation by measuring the PL spectra, which revealed the suppression of halide exchange reaction only at the irradiated part. I examined the PL decay profiles of the $MAPbBr_3$ microrods after the filling of halide vacancies which suggested the decrease of the nonradiative recombination at the laser-irradiated part and showed enhanced PL lifetime values. Thus, these results offer a new window for site-selective defect passivation and improving the optoelectronic properties of perovskite materials toward the construction of high-quality perovskite-based heterojunction devices.

4.4 References

1) Li, X.; Chen, W.; Zhang, S.; Wu, Z.; Wang, P.; Xu, Z.; Chen, H.; Yin, W.; Zhong, H.; Lin, S. 18.5% efficient graphene/GaAs van der Waals heterostructure solar cell. *Nano Energy* **2015**, 16, 310−319

2) Saliba M., Matsui T., Seo J.-Y., Domanski K., Correa-Baena J.-P., Nazeeruddin M. K., Zakeeruddin S.M., Tress W., Abate A., Hagfeldt A., Grätzel M. Cesium containing triple cation perovskite solar cells: improved stability, reproducibility and high efficiency. Energy & Environmental *Science* **2016**, 9, 1989–1997.

3) Dou, L.; Yang, Y. M.; You, J.; Hong, Z.; Chang, W. H.; Li, G.; Yang, Y. Solution-Processed Hybrid Perovskite Photodetectors with High Detectivity. *Nat. Commun*. **2014,** *5*, 5404.

4) Fang Y., Dong Q., Shao Y., Yuan Y., Huang, J. Highly narrowband perovskite single-crystal photodetectors enabled by surface-charge recombination. *Nature Photonics* **2015**, 9, 679–686.

5) Saidaminov, M. I.; Adinolfi, V.; Comin, R.; Abdelhady, A. L.; Peng, W.; Dursun, I.; Yuan, M.; Hoogland, S.; Sargent, E. H.; Bakr, O M. Planar-Integrated Single-Crystalline Perovskite Photodetectors *Nat. Commun*. **2015**, *6,* 8724.

6) Wang, N.; Cheng, L.; Ge, R.; Zhang, S.; Miao, Y.; Zou, W.; Yi, C.; Sun, Y.; Cao, Y.; Yang, R.; Wei, Y. Perovskite Light-Emitting Diodes Based on Solution-Processed Self-Organized Multiple Quantum Wells. *Nat. Photonics* **2016**, *10*, 699−704.

7) Mei, S.; Liu, X.; Zhang, W.; Liu, R.; Zheng, L.; Guo, R.; Tian, P. High-Bandwidth White-Light System Combining a Micro-LED with Perovskite Quantum Dots for Visible Light Communication. *ACS Appl. Mater. Interfaces* **2018**, *10*, 5641−5648.

8) Chen, S.; Roh, K.; Lee, J.; Chong, W. K.; Lu, Y.; Mathews, N.; Sum, T. C.; Nurmikko, A. A Photonic Crystal Laser from Solution Based Organo-Lead Iodide Perovskite Thin Films. *ACS Nano* **2016**, *10*, 3959−3967.

9) Bertolazzi, S.; Krasnozhon, D.; Kis, A. Nonvolatile memory cells based on MoS_2/graphene heterostructures. *ACS Nano* **2013**, *7*, 3246−3252.

10) Huang L., Gao Q., Sun L.-D., Dong H., Shi S., Cai T., Liao Q., Yan C.-H. Composition-graded cesium lead halide perovskite nanowires with tunable dual color lasing performance. *Advanced Materials* **2018**, *30*, 1800596.

11). Kim H.-S., Lee C.-R., Im J.-H., Lee K.-B., Moehl T., Marchioro A, Moon S.-J., Humphry-Baker R., Yum J.-H, Moser J. E., Gratzel M., Park N.-G, Lead iodide perovskite sensitized all-solid-state submicron thin film mesoscopic solar cell with efficiency exceeding 9%. *Sci. Rep.* **2012**, *2*, 591.

12) S. De Wolf, J. Holovsky, S.-J. Moon, P. Loper, B. Niesen, M. Ledinsky, F.-J. Haug, J.-H. Yum, C. Ballif, Organometallic halide perovskites: sharp optical absorption edge and its relation to photovoltaic performance. *J. Phys. Chem. Lett.* **2014**, *5*, 1035.

(13) Shi, D.; Adinolfi, V.; Comin, R.; Yuan, M.; Alarousu, E.; Buin, A.; Chen, Y.; Hoogland, S.; Rothenberger, A.; Katsiev, K.; Losovyj, Y. Low Trap-State density and long carrier diffusion in organolead Trihalide Perovskite Single Crystals. Science **2015**, *347*, 519−522.

14) Dong Q., Fang Y., Shao Y., Mulligan P., Qiu J., Cao L., Huang J. Electron-hole diffusion lengths > 175 μm in solution-grown $CH_3NH_3PbI_3$ single crystals. *Science* **2015**, *347*, 967–970.

15) Miyata A., Mitioglu A., Plochocka P., Portugall O., Wang J. T.-W., Stranks S. D., Snaith H. J., Nicholas R. J. Direct measurement of the exciton binding energy and effective masses for charge carriers in organic–inorganic tri-halide perovskites. *Nature Physics* **2015**, *11*, 582–587.

16) Chen D., Chen X. Luminescent perovskite quantum dots: synthesis, microstructures, optical properties, and applications. *Journal of Materials Chemistry C* **2019**, *7*, 1413–1446.

17) Dequilettes D. W., Koch S., Burke S., Paranji R. K., Shropshire A. J., Ziffer M. E., Ginger D. S. Photoluminescence lifetimes exceeding 8 μs and quantum yields exceeding 30% in hybrid perovskite thin films by ligand passivation. *ACS Energy Letters* **2016**, *1*, 438–444.

18) Wehrenfennig, C.; Eperon, G. E.; Johnston, M. B.; Snaith, H. J.; Herz, L. M. High charge carrier mobilities and lifetimes in organolead trihalide perovskites. *Adv. Mater.* **2014**, *26*, 1584–1589.

19) Wolf C., Kim J.-S., Lee T.-W., Structural and Thermal Disorder of Solution-Processed $CH_3NH_3PbBr_3$ Hybrid Perovskite Thin Films. *ACS Appl. Mater. Interfaces* **2017**, *9*, 10344.

20) Tan Z.-K., Moghaddam R. S., Lai M. L., Docampo P., Higler R., Deschler F., Price M., Sadhanala A., Pazos L. M., Credgington D., Hanusch F., Bein T., Snaith H. J., Friend R. H., Bright light-emitting diodes based on organometal halide perovskite. *Nat. Nanotechnol.* **2014**, *9*, 687.

21). Kalam A., Al-Sehemi A. G., Mahapatra A., Verma D., Trivedi S., Pandey M. K., Identification of defects and defect energy distribution in the perovskite layer of $MAPbI_{3-x}Cl_x$ perovskite solar cell *Mater.Res. Express* **2019**, *6*, 105510.

22) Dunfield S. P, Bliss L., Zhang F., Luther J. M., Zhu K., Hest M. V., Reese M. O., Berry J. J., From defects to degradation: a mechanistic understanding of degradation in perovskite solar cell devices and modules *Adv. Energy Mater*. **2020**, *10*, 1904054.

23) Yin W. J., Shi T. T., Yan Y. F., Unusual defect physics in $CH_3NH_3PbI_3$ perovskite solar cell absorber *Appl. Phys. Lett*. **2014**, *104*, 063903.

24) Kim J., Lee S. H., Lee J. H., Hong K. H., The role of intrinsic defects in methylammonium lead iodide perovskite *J. Phys. Chem. Lett.* **2014**, *5*, 1312.

25) Agiorgousis M. L., Sun Y., Zeng H., Zhang S., Strong covalency-induced recombination centers in perovskite solar cell material $CH_3NH_3PbI_3$ *J. Am. Chem. Soc.* **2014**, *136*, 14570.

26) Walsh A., Scanlon D. O., Chen S., Gong X. G., Wei S. H., Self-regulation mechanism for charged point defects in hybrid halide perovskites *Angew. Chem., Int. Ed.* **2015**, *54*, 1791.

27) Buin A., Pietsch P., Xu J., Voznyy O., Ip A. H., Comin R., Sargent E. H., Materials processing routes to trap-free halide perovskites *Nano Lett.* **2014**, *14*, 6281.

28) Buin A., Comin R., Xu J., Ip A. H., Sargent E. H., Halide-dependent electronic structure of organolead perovskite materials *Chem. Mater.* **2015**, *27*, 4405.

29) Azpiroz, J.M.; Mosconi, E.; Bisquert, J.; De Angelis, F. Defect migration in methylammonium lead iodide and its role in perovskite solar cell operation. *Energy Environ. Sci*. **2015**, *8*, 2118–2127.

30) Haruyama, J.; Sodeyama, K.; Han, L.; Tateyama, Y. First-Principles Study of Ion Diffusion in Perovskite Solar Cell Sensitizers. *J. Am. Chem. Soc.* **2015**, *137*, 10048–10051.

31) Yin,W.-J.; Shi, T.; Yan, Y. Unique Properties of Halide Perovskites as Possible Origins of the Superior Solar Cell Performance. *Adv. Mater.* **2014**, *26*, 4653–4658.

32) Kim, J.; Lee, S.-H.; Lee, J.H.; Hong, K.-H. The Role of Intrinsic Defects in Methylammonium Lead Iodide Perovskite. *J. Phys. Chem. Lett*. **2014**, *5*, 1312–1317.

33) Walsh, A.; Scanlon, D.O.; Chen, S.; Gong, X.G.; Wei, S.-H. Self-Regulation Mechanism for Charged Point Defects in Hybrid Halide Perovskites. *Angew. Chem. Int. Ed*. **2014**, *54*, 1791–1794.

34) Du M.H. Density Functional Calculations of Native Defects in $CH_3NH_3PbI_3$: Effects of Spin–Orbit Coupling and Self-Interaction Error. *J. Phys. Chem. Lett*. **2015**, *6*, 1461–1466.

35) Meggiolaro D., Motti, S.G.; Mosconi, E.; Barker, A.J.; Ball, J.; Perini, C.A.R.; Deschler, F.; Petrozza, A. De Angelis, F. Iodine chemistry determines the defect tolerance of lead-halide perovskites. *Energy Environ. Sci*. **2018**, *11*, 702–713.

36) J. S. Yun, J. Seidel, J. Kim, A. M. Soufiani, S. Huang, J. Lau, N. J. Jeon, S. I. Seok, M. A. Green, A. Ho-Baillie, Critical role of grain boundaries for ion migration in formamidinium and methylammonium lead halide perovskite solar cells *Adv. Energy Mater.* **2016**, *6*, 1600330.

37) R. Ohmann, L. K. Ono, H.-S. Kim, H. Lin, M. V. Lee, Y. Li, N.-G. Park, Y. Qi, Real-space imaging of the atomic structure of organic–inorganic perovskite *J. Am. Chem. Soc.* **2015**, *137*, 16049.

38) X. P. Zheng, B. Chen, J. Dai, Y. J. Fang, Y. Bai, Y. Z. Lin, H. T. Wei, X. C. Zeng, J. S. Huang, Defect passivation in hybrid perovskite solar cells using quaternary ammonium halide anions and cations *Nat. Energy* **2017**, *2*, 17102.

39) D. W. Dequilettes, W. Zhang, V. M. Burlakov, D. J. Graham,T. Leijtens, A. Osherov, V. Bulovic, H. J. Snaith, D. S. Ginger,S. D. Stranks, Photo-induced halide redistribution in organic–inorganic perovskite films *Nat. Commun.* **2016**, *7*, 11683.

40) B. H. Wang, K. Y. Wong, S. F. Yang, T. Chen, Crystallinity and defect state engineering in organo-lead halide perovskite for high-efficiency solar cells *J. Mater. Chem. A* **2016**, *4*, 3806.

41) H. Cho, S.-H. Jeong, M.-H. Park, Y.-H. Kim, C. Wolf, C.-L. Lee, J. H. Heo, A. Sadhanala, N. Myoung, S. Yoo, S. H. Im, R. H. Friend, T.-W. Lee, Overcoming the electroluminescence efficiency limitations of perovskite light-emitting diodes *Science,* **2015**, *350*, 1222.

42) S. Lee, J. H. Park, B. R. Lee, E. D. Jung, J. C. Yu, D. Di Nuzzo, R. H. Friend, M. H. Song, Amine-based passivating materials for enhanced optical properties and performance of organic–inorganic perovskites in light-emitting diodes *J. Phys. Chem. Lett.* **2017**, *8*, 1784.

43) A. Abate, M. Saliba, D. J. Hollman, S. D. Stranks, K. Wojciechowski, R. Avolio, G. Grancini, A. Petrozza and H. J. Snaith, *Nano Lett*., Supramolecular halogen bond passivation of organic–inorganic halide perovskite solar cells **2014**, *14*, 3247–3254.

44) Y. Shao, Z. Xiao, C. Bi, Y. Yuan and J. Huang, origin and elimination of photocurrent hysteresis by fullerene passivation in $CH_3NH_3PbI_3$ planar heterojunction solar cells *Nat. Commun.*, **2014**, *5*, 5784.

45) R. J. Stewart, C. Grieco, A. V. Larsen, J. J. Maier, J. B. Asbury, Approaching bulk carrier dynamics in organo-halide perovskite nanocrystalline films by surface passivation *J. Phys. Chem. Lett*. **2016**, *7*, 1148.

46) N. K. Noel, A. Abate, S. D. Stranks, E. S. Parrott, V. M. Burlakov, A. Goriely, H. J. Snaith, Enhanced Photoluminescence and Solar Cell Performance via Lewis Base Passivation of Organic–Inorganic Lead Halide Perovskites *ACS Nano* **2014**, *8*, 9815.

47) C. Bi, X. Zheng, B. Chen, H. Wei and J. Huang, Spontaneous passivation of hybrid perovskite by sodium ions from glass substrates: mysterious enhancement of device efficiency revealed *ACS Energy Lett.*, **2017**, *2*, 1400–1406.

48) Saidaminov, M.I.; Kim, J.; Jain, A.; Quintero-Bermudez, R.; Tan, H.; Long, G.; Tan, F.; Johnston, A.; Zhao, Y.; Voznyy, O.; et al. Suppression of atomic vacancies via incorporation of isovalent small ions to increase the stability of halide perovskite solar cells in ambient air. *Nat. Energy* **2018**, *3*, 648–654.

49) M. Abdi-Jalebi, Z. Andaji-Garmaroudi, S. Cacovich, C. Stavrakas, B. Philippe, J. M. Richter, M. Alsari, E. P. Booker, E. M. Hutter, A. J. Pearson, S. Lilliu, T. J. Savenije, H. Rensmo, G. Divitini, C. Ducati, R. H. Friend and S. D. Stranks, Maximizing and stabilizing luminescence from halide perovskites with potassium passivation *Nature*, **2018**, *555*, 497–501.

50) Nguyen, V.C.; Katsuki, H.; Sasaki, F.; Yanagi, H. Single-Crystal Perovskites Prepared by Simple Solution Process: Cast-Capping Method. *J. Cryst. Growth* **2017**, *468*, 796–799

51) Islam, M. J.; Shahjahan, M.; Yuyama, K. I.; Biju, V. Remote Tuning of Bandgap and Emission of Lead Perovskites by Spatially Controlled Halide Exchange Reactions. *ACS Mater. Lett.* **2020**, *2*, 403–408.

52) K. H. Wang, L. C. Li, M. Shellaiah, K. W. Sun, Structural and photophysical properties of methylammonium lead tribromide ($MAPbBr_3$) single crystals *Sci. Rep*. **2017**, *7*, 13643.

53) Karimata I., Kobori Y., Tachikawa T. Direct Observation of Charge Collection at Nanometer-Scale Iodide-Rich Perovskites during Halide Exchange Reaction on $CH_3NH_3PbBr_3$. *J. Phys. Chem. Lett*. **2017**, *8*, 1724−1728.

54) Zhang Y., Gao M. L., Lai M, Lin J., Lei T., Lin Z., Quan L. N., Yang P. Quantitative imaging of anion exchange kinetics in halide perovskites *Proceedings of the National Academy of Sciences* **2019**, *116* 12648-12653.

55) Mizusaki J., Arai K., Fueki K., Ionic conduction of the perovskite-type halides. *Solid state ion*., **1983**, 11 203–211.

56). Wu X, Trinh M. T., Niesner D., Zhu H., Norman Z., Owen J. S., Yaffe O., Kudisch B. J., Eames C., Frost J. M., Barnes P. R. F., O'Regan B. C., Walsh A., Islam M. S., Ionic transport in hybrid lead iodide perovskite solar cells *Nat. Commun*. **2015**, *6*, 7497.

57) Ashkin, A., Dziedzic, J. M., Bjorkholm J. E., Chu S. Observation of a single-beam gradient force optical trap for dielectric particles *Opt. Lett.* **1986**, *11*, 288−290.

58) Ito S., Yoshikawa H., Masuhara H., Optical patterning and photochemical fixation of polymer nanoparticles on glass substrates *Appl. Phys. Lett.* **2001**, *78*, 2566-2568.

(59) Guffey M. J., Scherer N. F., All-Optical Patterning of Au Nanoparticles on Surfaces Using Optical Traps. *Nano Lett*. **2010**, *10*, 4302−4308.

(60) Hofkens J., Hotta J., Sasaki K., Masuhara H., Iwai K. Molecular Assembling by the Radiation Pressure of a Focused Laser Beam: Poly(N-isopropylacrylamide) in Aqueous Solution. *Langmuir* **1997**, *13*, 414−419.

61) Mukai S., Magome N., Kitahata H., Yoshikawa K., Liquid/ liquid Dynamic Phase Separation Induced by a Focused Laser. *Appl. Phys. Lett.* **2003**, *83*, 2557−2559.

62) Yuyama K., Islam Md J., Takahashi K., Nakamura T., Biju V. Crystallization of Methylammonium Lead Halide Perovskites by Optical Trapping. *Angew. Chem. Int. Ed*. **2018**, *57*, 13424−13428.

Chapter 5

Spatially controlled charge carrier transport and collection in heterojunction halide perovskite single crystals and nanocrystal films

Halide perovskites have emerged as a class of promising semiconductor materials for next-generation optoelectronic devices due to their unique excitonic and charge carrier properties. Also, architecting perovskite heterostructures with distinguishing halide composition becomes promising for the generation and transport of charge carriers in solar cells. A facile way to achieve such wide compositional and optically tuneable heterostructure in halide perovskites is halide exchange reactions by replacing the halide ions in a parent crystal. However, precise control of the heterostructure domain size through spatial halide exchange reaction by delivering the guest precursors at a desired location is still challenging. Instead of the time consuming and sophisticated methods, here, we utilize a tightly focused near-infrared laser beam to prepare bandgap engineered perovskite heterojunction at desired locations as well as control the transport and accumulation of charge carriers across the heterojunction in methylammonium lead bromide ($MAPbBr_3$) microcrystals or nanocrystal films. The site-specific halide exchange reaction allows us to fabricate microscopic heterojunctions with two distinct bandgap-gradient iodide-rich and bromide-rich regions. The built-in halide gradient structures also enable the efficient accumulation of charge carriers in the narrow-bandgap iodide-rich region. Photogenerated excitons/charge carriers are transported from the surrounding wide-bandgap bromide-rich regions to the narrow-bandgap iodide-rich region. This investigation provides a convenient method for designing heterostructure-based optoelectronic devices where long-distance directional carrier funnelling is required.

5.1 Introduction

In recent years, lead halide perovskites have been realized promising for light-harvesting and light-emitting applications.[1-5] The success of these materials is attributed to their superior optoelectronic properties, including high charge carrier mobilities, long charge carrier lifetimes, high absorption coefficients, and facile bandgap tunability in the whole visible to near infrared (NIR) region.[6-9] In addition, perovskite heterostructures are essential building blocks for expanding the application of perovskite-based electronic and optoelectronic devices. Perovskite heterostructures are generally constructed through bandgap engineering by varying the halide compositions of these materials.[10-13] The soft crystal lattice structures of perovskites facilitate the diffusion of guest ions inside the parent crystals, and bandgap tuning at the exposed regions toward the fabrication of heterostructures.[14-16] For instance, Dou et al.[16] revealed the formation of $CsPbBr_3$-$CsPbCl_3$ perovskite heterostructure through the anion exchange method. In brief, they combined the anion exchange with electron-beam lithography and masked an individual nanowire with a thin layer of poly(methyl methacrylate). The nanowire was immersed in an oleylammonium halide solution to induce the halide exchange reaction at the uncovered area. This polymer mask-assisted exchange reaction enabled the formation of two-segment or multiple spatially resolved perovskite heterostructures in a single nanowire. The facile halide exchange reaction at solid-solid, solid-liquid, or solid-gas interfaces also facilitates the formation of the perovskite heterostructures through halide interdiffusion. Following the halide interdiffusion mechanism, Pan et al.[31] fabricated a halide gradient $CsPbBr_{3-x}I_x$ heterostructure by stacking the microplates of $CsPbCl_3$ on $CsPbBr_3$ nanowires. Due to the solid-state Br-Cl interdiffusion, the Cl in the upper $CsPbCl_3$ microplate gradually replaced Br in the lower $CsPbBr_3$ nanowire, which resulted the heterostructure formation.

Moreover, the charge carrier diffusion dynamics in perovskite semiconductors play a crucial role in terms of device stability and performance. To achieve highly efficient, and long-term stable perovskite devices, diffusion engineering of the photogenerated charge carriers is mandatory. Tian et al.[32] studied the carrier diffusion dynamics of individual $MAPbX_3$ (X = Br, I) nanowires, and nanoplates. They measured the carrier diffusion length, carrier mobility, and carrier lifetime values of the individual crystals using time-resolved and PL-scanned imaging microscopy. Although the long-range carrier migration is advantageous for perovskite devices, the carriers can be lost radiatively or nonradiatively during long-range migration or their energy can be lost. Thus, the construction of

composition-graded heterojunction is promising for trapping the carriers in a controlled way.[17] The flexible crystal lattice and abundant halide vacancies of perovskite materials enable facile switching of the halide sites in a spatially controlled manner and transfer the photogenerated carriers from a wide-bandgap region to narrow-bandgap region, which can help highly efficiency energy funneling in such halide-gradient heterostructures.[14,18] For example, Tian et al.[19] reported the fabrication of a halide-gradient nanowire heterostructure by contacting a $MAPbBr_3$ single crystal with a $MAPbI_3$ nanowire at one end. The solid-to-solid halide exchange reaction between the large $MAPbBr_3$ single crystal and $MAPbI_3$ nanowire resulted the formation of $MAPbBr_xI_{3-x}$ heterostructure. The resulted nanowire heterostructure formed an energy funnel and transported the charge carriers over a few micrometers from the wide-bandgap region to the narrow-bandgap region. Such carrier funneling is believed to facilitate carrier extraction at perovskite/electrode interfaces when applied in perovskite solar cells. However, despite these rapid progresses, the halide-gradient domain size, exciton/charge carrier transport dynamics and carrier accumulation at a desired location in the heterostructures are yet to be optimized.

Here, we report the construction of the narrow-bandgap iodide-rich domains in the wide-bandgap bromide microcrystals or nanocrystal films in a spatially resolved manner at the focal point of a NIR laser beam. Heterostructures are generated by inducing the halide exchange reaction at the desired location of the as-grown $MAPbBr_3$ microrods, microplates or nanocrystal films using the laser trapping technique.[20,21] In addition, we studied the charge carrier dynamics in the prepared heterostructures and revealed the transportation and accumulation of the photogenerated charge carriers in the narrow-bandgap iodide-rich region from the wide-bandgap bromide rich regions. These findings provide us a new way to locally engineer perovskite structures and optimize the optoelectronic charge carrier and bandgap properties of halide perovskites at a desired location.

5.2 Results and discussions

5.2.1 Preparation of heterojunctions at one end of microrod crystals

Figure 1a shows the experimental setup for constructing the heterojunctions in the as-prepared $MAPbBr_3$ microrods through laser trapping. Rod- and plate-shaped $MAPbBr_3$ microcrystals were prepared by the spontaneous solvent evaporation technique in the following process.[22,23] The precursor solution of $MAPbBr_3$ with 1.3 M concentration was prepared by dissolving the precursor salts (MABr and $PbBr_2$) in the 1:1 ratio in *N,N*-

dimethylformamide (DMF). Subsequently, the precursor solution was mixed with GBL solution in the 1:1 ratio (v: v) to form an unsaturated solution. 1 µL of the supernatant from the mixed solution was placed on a coverslip inside a homemade silicone chamber. Spontaneous crystallization of the $MAPbBr_3$ crystals with different sizes and shapes started growing inside the precursor solution through natural solvent evaporation. The crystals further grew with time, and after confirming the desired size under a microscope the remaining solution was removed by wiping with a filter paper to arrest the crystal growth. After the synthesis, the as-prepared $MAPbBr_3$ rods and microplates were immersed in a reaction solution of MAI (125 µM) prepared in a mixture (1:100, v/v) of isopropanol and 1-hexadecene to induce bromide-to-iodide exchange reaction at the laser focal point.

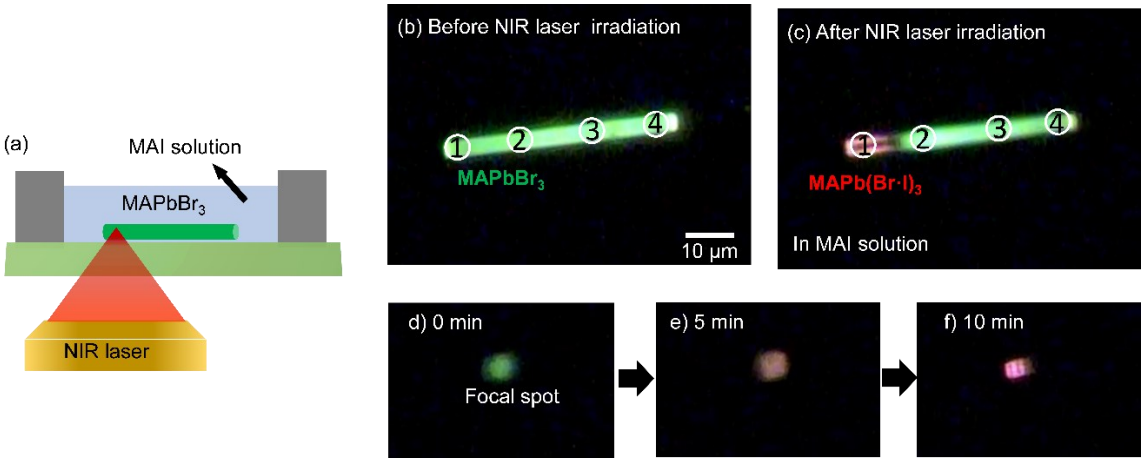

Figure 5.01: (a) A scheme of the laser trapping technique for spatially controlled halide exchange reaction. (b,c) PL images of the $MAPbBr_3$ microrods (b) before and (c) after the halide exchange reaction in an MAI solution. (d-f) Confocal two-photon excited fluorescence images of the NIR laser irradiated part showing temporal changes in PL images at (d) 0 min, (e) 5 min, and (f) 10 min.

Figure 1b shows a PL image of the as-prepared $MAPbBr_3$ microrod under a 405 nm wide-field laser illumination. This $MAPbBr_3$ microrod shows intense green emission due to the characteristic band-to-band transition. To prepare the bromide-iodide heterojunctions with the crystal, the microrod was immersed in a MAI reaction solution and the NIR laser beam was focused at one end of the microrod to induce the Br-to-I exchange reaction (Figure 1a). At the beginning of the NIR laser irradiation (Figure 1d), the irradiated part showed green emission at the focal volume under two-photon excitation. As the reaction proceeded, the

PL emission of the irradiated part changed from green-to-orange yellowish-to-red within 10 min of irradiation (Figure 1d-f). The change in the PL color indicates the halide exchange reaction by replacing the Br^- ions with I^- ions at the focal volume. As-shown in Figure 1c, after the laser irradiation the microrod showed red emission exclusively at the irradiated part while the other parts remained green emissive under wide-field illumination. These results indicate that the focused laser irradiation induced exchange reaction from $MAPbBr_3$ to $MAPbBr_{3-x}I_x$ selectively at the irradiated part and fabricated halide composition graded heterojunction in the same microrod.

For quantitative analysis of the heterojunction formation, the PL spectra were also measured during the spatial halide exchange reaction. Prior to the reaction, the PL spectrum of the as-prepared $MAPbBr_3$ microrod was measured by excitation with a 1064 nm NIR laser and the crystal showed the emission maximum at 545 nm. This PL maximum is comparable to the reported value of the $MAPbBr_3$ single crystals.[24] Next, we recorded PL spectra from the irradiated area at every 2 min intervals. As shown in Figure 2a, with time, the PL spectra continuously shifted towards the higher wavelength region upon the NIR laser irradiation. Finally, the PL maximum was at 715 nm after 10 min. Moreover, after the laser irradiation for 10 min the PL spectra was also measured from the nonirradiated parts of the crystal. Figure 2b shows. the PL maxima remained unchanged at the nonirradiated parts. The continuous PL shift of the irradiated area, while maintaining the characteristic green (λ_{max} = 545 nm) emission of the bromide perovskite throughout the nonirradiated parts allow us to consider that the laser-irradiated part selectively changed into $MAPbBr_{3-x}I_x$, creating a donor (bromide part) – acceptor (iodide-rich part) heterostructure in the microrod. In short, by the spatially controlled halide exchange, we prepared a heterojunction perovskite single crystal with donor-acceptor band structure.

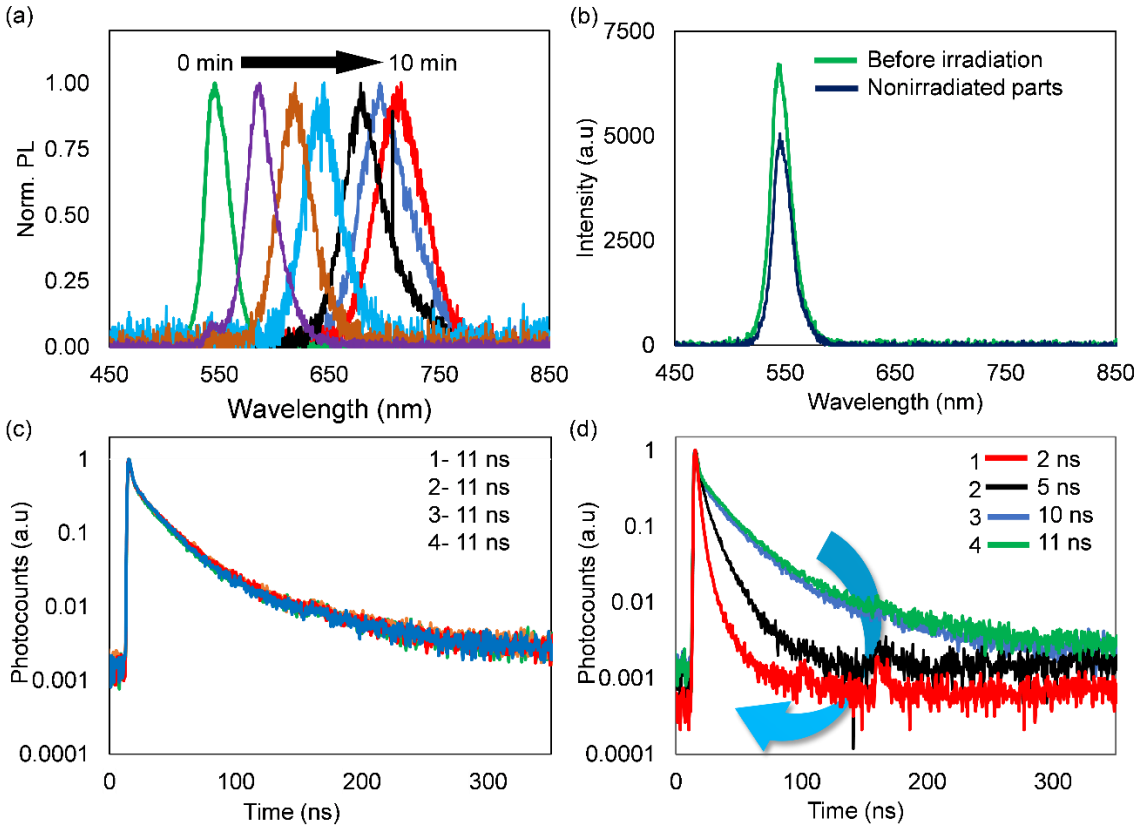

Figure 5.02: (a) PL spectral changes at the two-photon irradiation area for a $MAPbBr_3$ microrod immersed in an MAI solution, (b) PL spectra of the $MAPbBr_3$ microrod before irradiation and from the nonirradiated parts after irradiation, (c, d) PL decay profiles from (c) different parts of the $MAPbBr_3$ microrod measured before the laser irradiation and (d) the laser irradiated part and nonirradiated parts after the laser irradiation.

To analyze the transfer of photogenerated electrons and holes from the parent bromide perovskite to the newly formed iodide-rich part, we studied the charge carrier dynamics of the microrod crystals before and after the laser irradiation. We find a direct correlation between the charge carrier/exciton recombination rates along the microrod before and after the exchange reaction. Before the exchange reaction, we recorded the PL decays from four different positions of the microrod. The decay profiles are shown in Figure 2c. We fitted the decays with 3rd exponential equation and the PL lifetimes were estimated at 11 ns for the positions 1 to 4 marked in Figure 1b. The constant PL lifetime indicates a uniform distribution of bandgap and charge carriers in the whole microrod. Depending on the nucleation-growth process, the lifetime values differ from crystal to crystal because of the crystal quality or the difference in the halide vacancy densities. After the laser irradiation, the PL lifetime decreased while moving from the nonirradiated part to the irradiated part.

The initial value of 11 ns before halide exchange reaction decreased to 2 ns after laser irradiation at position 1. Interestingly, the lifetime value gradually increased as the measurement point was shifted to the nonirradiated part (Figure 1c). The lifetime values are 5 ns, 10 ns, 11 ns respectively at positions 2, 3, and 4 (Figure 2d). Conversely, as we created exciton/charge carriers closer and closer to the narrow bandgap region formed by the exchange reaction, the rate of exciton/carrier recombination increased by 5-fold. This increase in the rate is attributed to three factors: (i) the intrinsically short PL lifetime of the iodide-rich region, (ii) an increased nonradiative rate of exciton/carrier recombination due to the formation of vacancies during the two-photon irradiation, and (iii) the interface between the bromide and iodide rich region where fast nonradiative recombination is promoted by the indirect bandgap nature of the mixed halide region. Nonetheless, the bright red emission from the exchanged part suggests a small extent nonradiative recombination. In other words, the short PL lifetime of the iodide-rich part and decrease of PL lifetime while moving from part 4 to part 1 suggest the intrinsically fast radiative recombination of the iodide-rich part.

5.2.2 Preparation of heterojunctions at one half of microrod crystals

To further confirm the accumulation of charge carriers at the laser irradiated part, we moved the two-photon excitation center gradually from one end to the other and performed the halide exchange reaction in a larger area of the microrod. As shown in Figure 3a, the as-prepared $MAPbBr_3$ microrod showed green emission in the entire region. To induce the halide exchange reaction in a larger area, first the NIR laser beam was focused on position 1 in Figure 3b while immersing the microrod in an MAI reaction solution. The initial green emission was changed into red within 10 min which confirmed the halide exchange reaction at the irradiated part. After tuning the emission color at position 1, the NIR laser beam was moved to position 2 and the halide exchange reaction was induced similarly. Under the wide field illumination with 405 nm laser, the microrod showed two distinct parts with red and green emission (Figure 3b) and confirmed the bromide-iodide heterostructure. To examine the exchange reaction, we continuously recorded the PL spectra from the irradiated parts. As shown in Figure 3c the spectral change from green to red during the laser irradiation further confirmed the halide exchange reaction. The initial PL maximum was measured at 545 nm which gradually shifted to 740 nm after 10 min of laser irradiation at parts 1 and 2. After confirming the large area heterostructure fabrication, the PL lifetime was measured at the marked positions in Figure 3b. Interestingly, the PL lifetimes of part

1 and 2 was 1 ns, whereas as we moved to the bromide-rich portion, the lifetime increased to 4 ns at part 3 and 6 ns at part 4. The PL lifetimes of the green-emitting regions were much smaller (4 or 6 ns) than (11 ns) the as-synthesized $MAPbBr_3$ crystal. The short lifetimes of the green-emitting part suggest the formation of a small amount of mixed halide perovskites throughout the crystal, which is attributed to the migration of iodide from the I-rich to the Br-rich portion

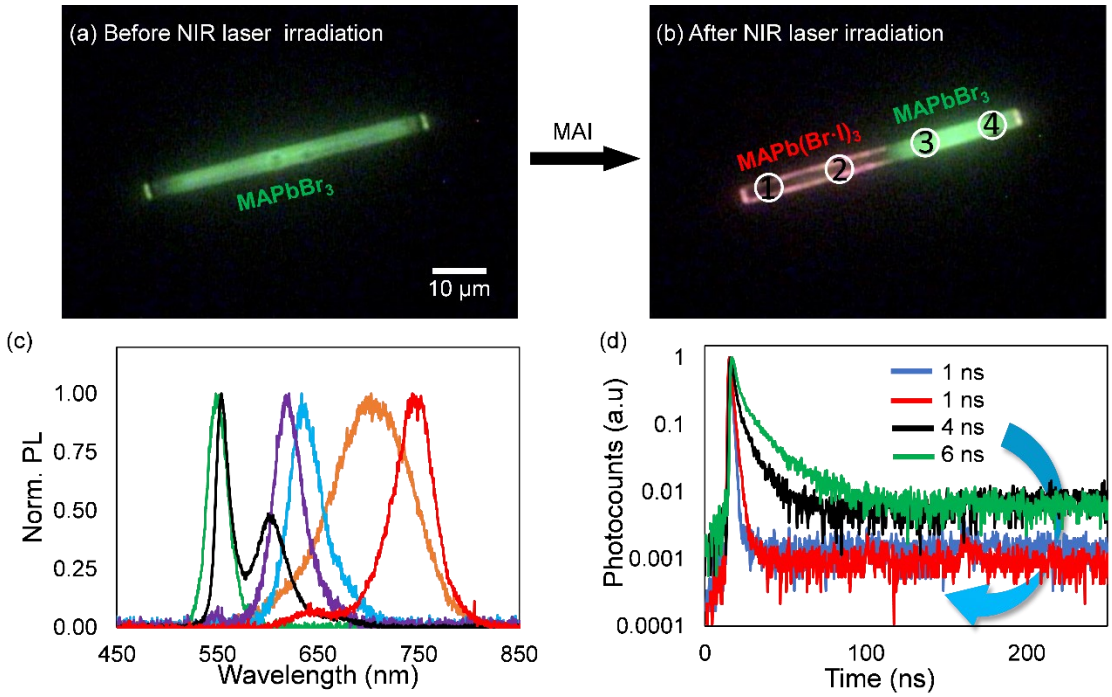

Figure 5.03: PL emission images of the $MAPbBr_3$ microrod (a) before the halide exchange reaction, (b) after the halide exchange reaction at one half of the microrod, (c) PL spectral change during the halide exchange reaction under NIR laser irradiation, (d) PL decay profiles from the laser irradiated and nonirradiated parts of the $MAPbBr_3$ microrod measured after the laser irradiation.

and vice versa or the long time (20 min or more) incubation of the crystal in the MAI solution leading to partial spontaneous exchange. However, we rule out the later based on a control experiment in which an $MAPbBr_3$ rod was immersed in an equivalent MAI solution, but without any two-photon excitation. In this case, the PL lifetime of the crystal was not decreased over 20 min. Thus, the reduced PL lifetime values (4 and 6 ns) of parts 3 and 4 in Figure 3b suggest iodide ion migration within the crystal from the I-rich domains (parts 1 and 2) to the Br-rich domains (parts 3 and 4). Similarly, bromide ions migrate from

parts 3 and 4 to parts 1 and 2. Since such halide ion migration through halide vacancies creates mixed halide perovskites to a small extend, which increase with time , the red-emitting portion is iodide rich with some contribution of the bromide ions, which are quickly exchanged during the laser trapping. However, the iodide ions migrating from parts 1 and 2 to parts 3 and 4 increase with time, producing more and more mixed halides, where the charge carriers segregate between the iodide conduction band (electron) and the bromide valance band (holes) leading to nonradiative recombination and short PL lifetimes.

5.2.3 Preparation of heterojunctions at the center of microcrystals

The 1064 nm NIR laser was then utilized for constructing the heterostructure in a selected part of a plate-shaped $MAPbBr_3$ crystal. For this experiment, the plate-shaped $MAPbBr_3$ crystals were prepared following the similar solvent evaporation synthetic route. The as-prepared crystal showed green emission from the entire region under wide-field excitation with 405 nm laser which is one of the characteristic features of a $MAPbBr_3$ crystal (Figure 4a).

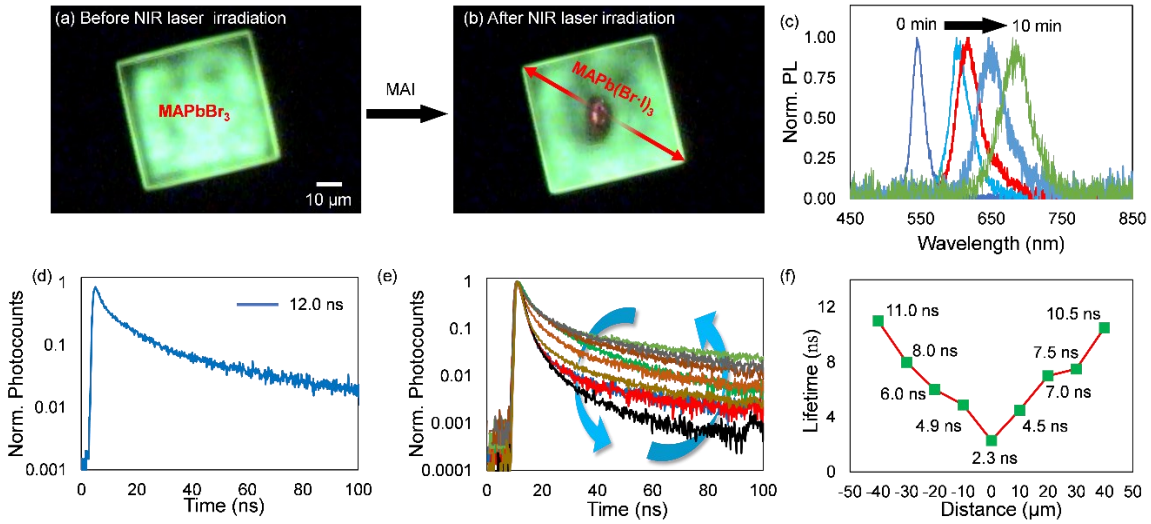

Figure 5.04: PL images of (a) an as-prepared $MAPbBr_3$ microcrystal before starting the exchange reaction, (b) the microcrystal in an MAI solution after irradiating the center area with the 1064 nm laser, (c) PL spectra from the irradiated area of the crystal during the exchange reaction, (d) PL decay profile of the $MAPbBr_3$ microrod measured before the laser irradiation, (e) PL decay profiles of the laser irradiated part and nonirradiated parts measured from different distances, (f) the calculated lifetime values as a function of distance measured at every 10 μm distances from the irradiated part

Then, the reaction solution MAI of concentration 125 μM was put in the sample chamber. Immediately after immersing the crystal with the reaction solution, the laser beam from the NIR laser was focused on the center part of the crystal. Under the laser irradiation, the center part of the crystal gradually changed its emission color from green to red within 10 min. Under wide-field illumination, the Figure 4b shows the PL image of the microcrystal after laser irradiation where a clear distinction between the laser irradiated part and nonirradiated part is observed. The center part of the crystal showed red emission while the surrounding nonirradiated parts remain green emissive. Also, the initial PL maximum of the as-prepared crystal showed a gradual redshift under laser irradiation. The PL spectra of the irradiated center part shifted from 545 nm to around 700 nm after the laser irradiation (Figure 4c). The change of the emission color and PL spectral shift at the focal volume of the laser confirms the halide exchange reaction exclusively at the center part of the crystal towards the fabrication of heterostructure. Furthermore, a distance dependent charge carrier recombination process was studied from the irradiated part to the nonirradiated parts of the heterostructure to reveal the directional diffusion of charge carriers into the iodide rich narrow-bandgap region from the bromide rich higher bandgap region. Figure 4d shows a representative PL lifetime decay curve of the as-prepared crystal before immersing in the MAI reaction solution. The average lifetime of the initial crystal was calculated around 12 ns from different parts of the crystal. However, after the formation of heterostructure the PL decays were recorded from the exchanged central part and the unchanged parts at every 10 μm distance along the arrow shown in Figure 4b. Figure 4e shows the lifetime values of the crystal measured at different distances from the laser irradiated part. We found the shortest PL lifetime for the central iodide-rich region and a gradual increase of lifetime values apart from the exchanged part. From both the measured sides the lifetime values were almost similar at same distances. The PL lifetime of the iodide-rich part was calculated 2.3 ns. Finally, the lifetime value reached upto 11 ns and 10.5 ns respectively at the two ends of bromide-rich region which is 40 μm away from the exchanged part (Figure 4f). The lifetime values from different parts of the heterostructure further confirm the diffusion of charge carriers from the wide-bandgap bromide-rich region to the narrow-bandgap iodide-rich region.

5.2.4 Preparation of heterojunctions at specific parts of the nanocrystal films

To evaluate the universality of the carrier accumulation in the laser induced exchanged part, we also demonstrated the fabrication of heterostructure in a desired position of the $MAPbBr_3$ nanocrystal thin films. The $MAPbBr_3$ nanocrystals were synthesized by the ligand-assisted reprecipitation method and deposited on the cover glass following one-step drop-casting deposition technique.[25-28]

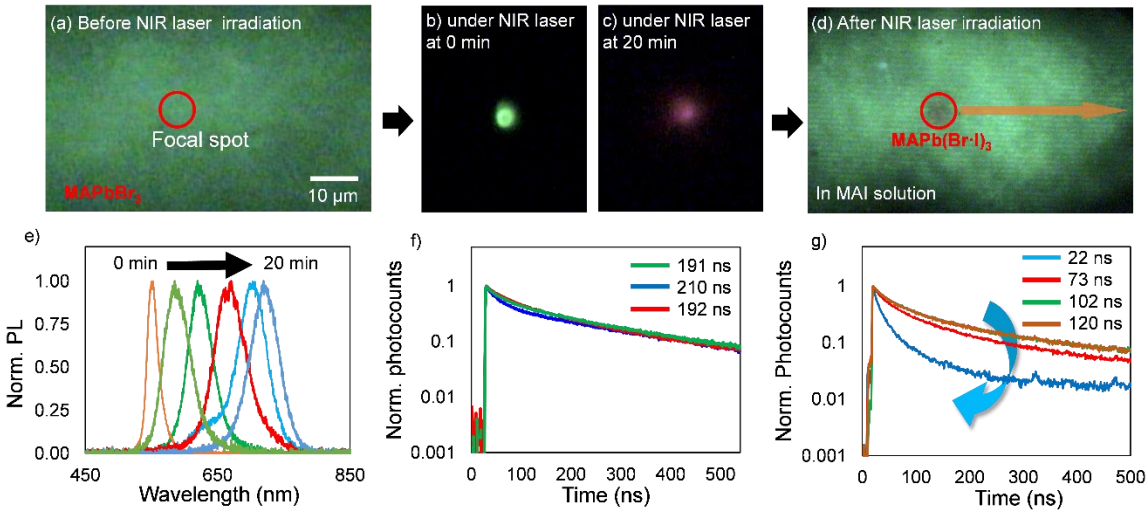

Figure 5.05: PL images of the $MAPbBr_3$ thin film under wide-field excitation (a) before the halide exchange reaction, (d) in an MAI solution after the halide exchange reaction, PL images from the focal volume of the NIR laser (b) at the beginning of the exchange reaction, (c) after 20 min of laser irradiation, (e) PL spectral changes during the two-photon excited exchange reaction, PL decay profiles from (f) different parts of the $MAPbBr_3$ nanocrystal thin film measured before the laser irradiation and (g) the laser irradiated part and nonirradiated parts after the laser irradiation.

Figure 5a shows the PL image of an as-prepared thin film prepared by depositing the $MAPbBr_3$ nanocrystals. After preparing the thin film, a reaction solution of MAI was put inside the sample chamber and subsequently, the NIR laser beam was focused on the air/solution surface of the thin film to induce the site-specific halide exchange reaction. As shown in Figure 5b in the beginning of the exchange reaction an intense green emission was observed from the focal volume of the laser beam. This PL emission of the focal spot gradually changed to red within 20 min which confirm the halide exchange reaction (Figure 5c). After the NIR laser irradiation, upon wide-field excitation the laser irradiated part

showed red emission from the irradiated part while the other parts remain green emissive as the beginning of the reaction (Figure 5d). Also, the PL spectra were measured under laser irradiation which further confirmed the exchange reaction quantitatively. The initial PL maximum was found at 545 nm which gradually changed as the reaction proceeded and finally redshifted to 725 nm after 20 min of laser irradiation (Figure 5e). The PL emission color and spectral changes allowed us to consider the formation of the heterostructure in the thin films of a $MAPbBr_3$ nanocrystal. Furthermore, the PL lifetime was also studied along the prepared heterostructure to understand the charge carrier dynamics. Before the NIR laser irradiation, the PL lifetime was measured from three different parts of the thin films and the lifetime values were measured 191 ns, 210 ns and 192 ns, respectively (Figure 5f). A longer lifetime of the as-prepared thin films is attributed to the long-range charge carrier migration and photon recycling process of the photogenerated excitons or free charge carriers. However, after the exchange reaction the PL lifetime was measured again from the iodide -rich exchanged part and after every 10 μm from the bromide-rich region. The lifetime values were measured from the three parts of the bromide-rich region along the arrow shown in Figure 5d. The lifetime value was calculated 22 ns from the exchanged part of the thin film. An increase in the lifetime values were found apart from the exchanged part similar to the microrods and plate-shaped microcrystals. The lifetime values at 10 μm, 20 μm, 30 μm distances were found 73 ns, 102 ns, 120 ns respectively from the three measured areas (Figure 5g). These distinct PL lifetime values further confirm the transportation of charge carriers from the higher bandgap bromide-rich region to the lower bandgap iodide-rich region and accumulation of these charge carriers in the laser induced exchanged part.

5.3 The mechanism of the laser induced charge carrier accumulation

Here, we summarize the dynamics of charge carrier accumulation in the laser induced halide exchanged part of the $MAPbBr_3$ crystals. When an as-prepared $MAPbBr_3$ crystal is excited, the photogenerated carriers are homogeneously distributed over the whole crystal and follow similar recombination pathway (Figure 6a). The pure as-prepared $MAPbBr_3$ crystals thus exhibit uniform distribution of local PL dynamics and give almost similar PL lifetime values from the whole crystal. Moreover, in our previous studies we demonstrated that the strong optical force generated by the focused NIR laser beam can increase the local concentration of reactive perovskite precursors and induce halide exchange reaction at the focal volume.[29,30]

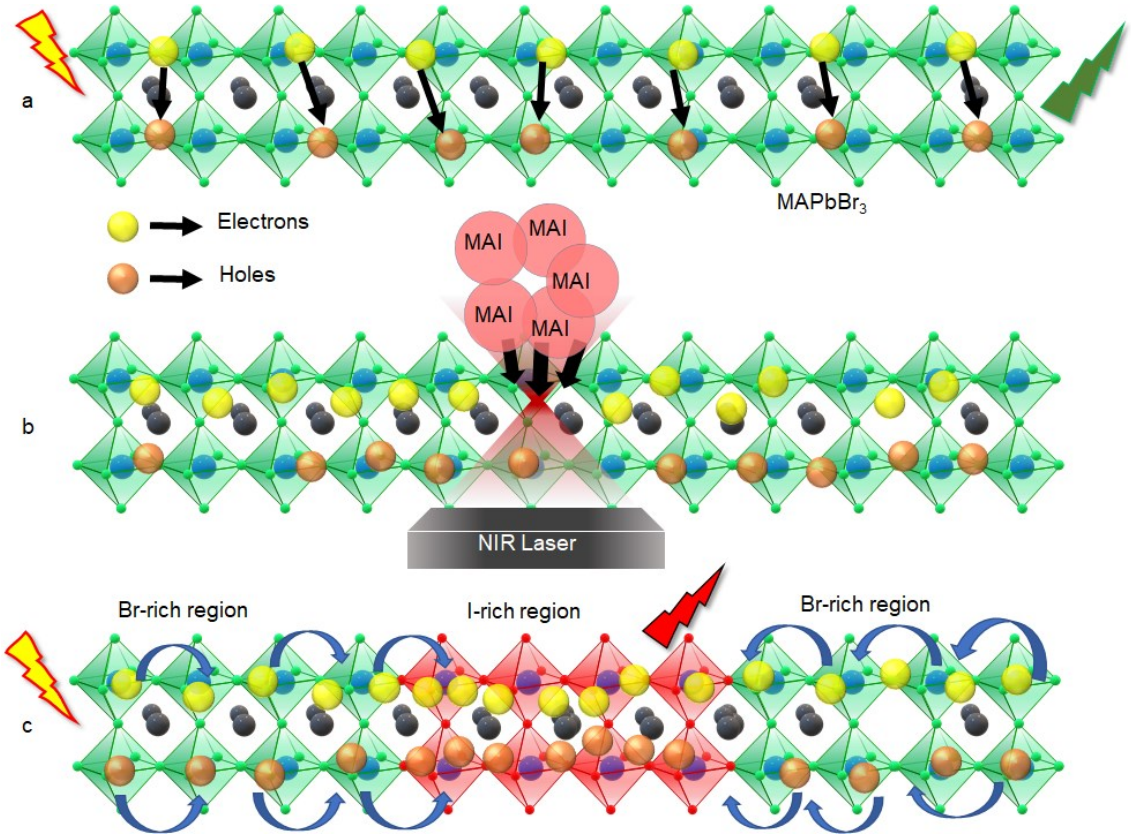

Figure 5.06: Schematic representation of the heterostructure formation and charge carrier accumulation in the $MAPbBr_3$ crystals. (a) an as-prepared $MAPbBr_3$ crystal showing uniform distribution of charge carriers in the whole area, (b) procedure for the laser trapping induced site-specific halide exchange reaction, (c) transportation and recombination of charge carriers in the prepared heterostructure to the iodide-rich region from the bromide-rich region.

As illustrated in Figure 6b, we utilized this potential mechanism to induce the site-specific halide exchange reaction which creates a halide composition-gradient heterostructure with distinct $MAPbBr_3$ and $MAPbBr_{3-x}I_x$ in the same crystals. In such a halide-graded heterostructure the carriers quickly diffuse toward the narrow-bandgap region which is driven by the efficient energy funnelling (Figure 6c). Due to this movement and accumulation of charge carriers the PL decay in the iodide-rich region become fast while a gradual increase of the PL decay apart from the iodide-rich domain is observed. As a consequence of the carrier transport and recombination into the iodide-rich domain from the surrounding bromide-rich region, a low PL lifetime value compared to the initial value results in the surrounding area upto several micrometres.

5.4 Conclusions

In summary, we have successfully demonstrated the fabrication of perovskite heterostructures in different dimension of $MAPbBr_3$ crystals by controlling the anion exchange reaction at desired sites using laser trapping technique. We have also shown the accumulation of charge carriers in the halide exchanged iodide-rich domains which is facilitated by the transportation of charge carriers by the raising bandgap distribution. Thus, these findings open a new window toward the fabrication of high-quality perovskite heterojunction based optoelectronic devices.

5.5 References

1. Lee M. M., Teuscher J., Miyasaka T., Murakami T. N., Snaith H. J., Efficient Hybrid Solar Cells Based on Meso-Superstructured Organometal Halide Perovskites. *Science* **2012,** *338*, 643−650.

2. Tan Z.−K., Moghaddam R. S., Lai M. L., Docampo P., Higler R., Deschler F., Price M., Sadhanala A., Pazos L. M., Credgington D., Bright Light-Emitting Diodes Based on Organometal Halide Perovskite. *Nat. Nanotechnol*. **2014,** *9*, 687−692.

3. Xing G. , Mathews N., Lim S. S., Yantara N., Liu X., Sabba D., Grätzel M., Mhaisalkar S., Sum T. C. Low-Temperature Solution-Processed Wavelength-Tunable Perovskites for Lasing. *Nat. Mater*. **2014**, *13*, 476−480.

4. Wang, L.; Yuan, G. D.; Duan, R. F.; Huang, F.; Wei, T. B.; Liu, Z. Q.; Wang, J. X.; Li, J. M. Tunable Bandgap in Hybrid Perovskite $CH_3NH_3Pb(Br_{3-y}X_y)$ Single Crystals and Photodetector Applications. *AIP Adv*. **2016**, 6, 45115.

5. Kojima A., Teshima K., Shirai Y., Miyasaka T., Organometal halide perovskites as visible-light sensitizers for photovoltaic cells *J. Am. Chem. Soc*., **2009**, *131*, 6050–6051.

6. Stranks S. D., Eperon G. E., Grancini G., Menelaou C., Alcocer M. J. P., Leijtens T., Herz L. M., Petrozza A., Snaith H. J. Electron-Hole Diffusion Lengths Exceeding 1 Micrometer in an Organometal Trihalide Perovskite Absorber *Science* **2013**, *342*, 341−345.

7. Dong Q., Fang Y., Shao Y., Mulligan P., Qiu J., Cao L., Huang J. Solar Cells. Electron-Hole Diffusion Lengths > 175μm in Solution-Grown $CH_3NH_3PbI_3$ Single Crystals. *Science,* **2015**, *347*, 967−970.

8. Dequilettes D. W., Koch S., Burke S., Paranji R. K., Shropshire A. J., Ziffer M. E., Ginger D. S. Photoluminescence lifetimes Exceeding 8 μs and Quantum Yields Exceeding 30% in Hybrid Perovskite Thin Films by Ligand Passivation. *ACS Energy Letters,* **2016**, 1, 438–444.

9. Wehrenfennig, C.; Eperon, G. E.; Johnston, M. B.; Snaith, H. J.; Herz, L. M. High charge carrier mobilities and lifetimes in organolead trihalide perovskites. *Adv. Mater.*, **2014**, 26, 1584–1589.

10. Jang D. M., Park K., Kim D. H., Park J., Shojaei F., Kang H. S., Ahn J. P., Lee J. W., Song J. K. Reversible halide exchange reaction of organometal trihalide perovskite colloidal nanocrystals for full-range band gap tuning. *Nano Lett.,* **2015**, 15, 5191–5199.

11. Akkerman Q. A., D'Innocenzo V., Accornero S., Scarpellini A.Petrozza, A., Prato M., Manna L. Tuning the optical properties of cesium lead halide perovskite nanocrystals by anion exchange reactions. *J. Am. Chem. Soc*., **2015**, 137, 10276−10281.

12. Nedelcu G., Protesescu L., Yakunin S., Bodnarchuk M. I., Grotevent M. J., Kovalenko M. V. Fast anion-exchange in highly luminescent nanocrystals of cesium lead halide perovskites ($CsPbX_3$, X = Cl, Br, I). *Nano Lett.,* **2015**, 15, 5635–5640.

13. Levchuk I., Osvet A., Tang X., Brandl M., Perea J. D., Hoegl F., Matt G. J., Hock R., Batentschuk M., Brabec C. J. Brightly luminescent and color-tunable formamidinium lead halide perovskite FAPbX3 (X = Cl, Br, I) colloidal nanocrystals. *Nano Lett.,* **2017**, *17*, 2765–2770

14. Minliang L., Amael O., Dylan L., Christopher S. K., Connor G. B., Qiao K., Teng L., Letian D., Naomi S. G., David T. L., Peidong Y. Intrinsic anion diffusivity in lead halide perovskites is facilitated by a soft lattice *PNAS,* **2018**, *115*, 11929-11934.

15. Xia H. R., Li L. X., Wei J. Q., Wang J. Y., Yang Z. H., Guan Q. C., Jiang W. L. Phase transition and the soft lattice mode of a perovskite crystal studied by Raman scattering and thermal measurements *Journal of Materials Research*, **1999**, *14*, 4701 – 4705.

16. Dou L., Lai M., Kley C. S., Yang Y., Bischak C. G., Zhang D., Eaton S. W.,Ginsberg N. S., Yang P. Spatially resolved multicolor CsPbX3 nanowire heterojunctions via anion exchange. *PNAS*, **2017**, 114, 7216–7221.

17. Tong C.-J., Li L., Liu L.-M., Prezhdo O. V. Synergy between ion migration and charge carrier recombination in metal-halide perovskites *J. Am. Chem. Soc.,* **2020**, *142*, 6, 3060–3068

18. Dunfield S. P, Bliss L., Zhang F., Luther J. M., Zhu K., Hest M. V., Reese M. O., Berry J. J., From defects to degradation: a mechanistic understanding of degradation in perovskite solar cell devices and modules *Adv. Energy Mater*., **2020**, *10*, 1904054.

19. Tian W., Leng J., Zhao C. Jin S. Long- distance charge carrier funneling in perovskite nanowires enabled by built- in halide gradient. *J. Am. Chem. Soc*., **2017**, *139*, 579–582.

20. Ashkin A. Acceleration and trapping of particles by radiation pressure. *Physical Review Letters,* **1970**, 24, 156–159.

21. Yuyama K., Islam M. J., Takahashi K., Nakamura T., Biju V. Crystallization of Methylammonium Lead Halide Perovskites by Optical Trapping. *Angew. Chem. Int. Ed*., **2018**, *57*, 13424−13428.

22. Nguyen V.C., Katsuki H., Sasaki F., Yanagi H. Single-Crystal Perovskites Prepared by Simple Solution Process: Cast-Capping Method. *J. Cryst. Growth,* **2017**, *468*, 796–799.

23. Huang Y., Zhang Y., Sun J., Wang X., Sun J., Chen Q., Pan C., Zhou H. The exploration of carrier behavior in the inverted mixed perovskite single-crystal solar cells. *Adv. Mater. Interfaces,* **2018**, *5*, 1800224.

24. Wang K. H., Li L. C., Shellaiah M., Sun K. W. Structural and Photophysical Properties of Methylammonium Lead Tribromide ($MAPbBr_3$) Single Crystals *Sci. Rep.,* **2017**, *7*, 1–14.

25. Sun, S.; Yuan, D.; Xu, Y.; Wang, A.; Deng, Z. Ligand-Mediated Synthesis of Shape-Controlled Cesium Lead Halide Perovskite Nanocrystals via Reprecipitation Process at Room Temperature. *ACS Nano,* **2016**, *10*, 3648–3657.

26. Schmidt, L. C.; Pertegás, A.; González-Carrero, S.; Malinkiewicz, O.; Agouram, S.; Mínguez Espallargas, G.; Bolink, H. J.; Galian, R. E.; Pérez-Prieto, J. Nontemplate Synthesis of CH3 NH3PbBr3 Perovskite Nanoparticles. *J. Am. Chem. Soc.,* **2014**, *136*, 850–853.

27. Ghimire, S.; Chouhan, L.; Takano, Y.; Takahashi, K.; Nakamura, T.; Yuyama, K.; Biju, V. Amplified and Multicolor Emission from Films and Interfacial Layers of Lead Halide Perovskite Nanocrystals. *ACS Energy Lett.,* **2019**, *4*, 133–141.

28. Nie W., Tsai H., Asadpour R., Blancon J.-C., Neukirch A. J., Gupta G., Crochet J. J., Chhowalla M., Tretiak S., Alam M. A., Wang H.-L., Mohite A. D. High-Efficiency Solution-Processed Perovskite Solar Cells with Millimeter-Scale Grains. *Science,* **2015**, *347* , 522–525.

29. Islam M. J., Shahjahan M., Yuyama K. I., Biju V. Remote Tuning of Bandgap and Emission of Lead Perovskites by Spatially Controlled Halide Exchange Reactions. *ACS Mater. Lett.*, **2020**, *2* , 403–408.

30. Shahjahan M., Yuyama K., Okamoto T., Biju V. Heterojunction Perovskite Microrods Prepared by Remote-Controlled Vacancy Filling and Halide Exchange. *Adv. Mater. Technol.,* **2021**, *6* , 2000934.

31. Pan D., Fu Y., Chen J., Czech K. J., Wright J. C., Jin S. Visualization and Studies of Ion-Diffusion Kinetics in Cesium Lead Bromide Perovskite Nanowires. *Nano Lett.* **2018**, *18*, 1807–1813

32. Tian W., Zhao C., Leng J., Cui R., Jin S. Visualizing Carrier Diffusion in Individual Single-Crystal Organolead Halide Perovskite Nanowires and Nanoplates. *J. Am. Chem. Soc.* **2015,** *137*, 12458−12461

Summary and perspectives

In summary, I have demonstrated the fabrication of heterostructures in perovskite single crystals and thin films by modifying their bandgap. The bandgap modification was achieved by halide exchange reaction with the use of a tightly focused NIR laser beam. The laser trapping force was used for inducing the halide exchange reaction at the specific sites of the perovskite crystals. In this work, I also studied the role of halide vacancies on the halide exchange reaction of perovskite crystals and demonstrated the site-selective defect passivation at the desired location of the crystals through vacancy filling using the focused NIR laser beam. The study further investigated the transport and accumulation of charge carriers at the narrow-bandgap region of the prepared bandgap-graded heterostructures.

For the studies, I synthesized the microrod and microplate-shaped lead halide perovskite single crystals using facile solvent evaporation method and the nanocrystals through ligand-assisted reprecipitation method. Site-specific halide exchange reaction was induced in the crystals by immersing them in a reactive halide precursor solution. The optical force generated by the focused laser beam increased the local concentration of halide precursors at the focal volume and induced the halide exchange reaction in a specified domain under laser trapping. The change of emission color and spectra at the irradiated part confirmed the bandgap tuning of the crystals in a spatio-temporal manner.

The laser trapping tool was further utilized for the defect passivation and to reduce the nonradiative recombination of charge carriers at the specific sites of the perovskite crystals. I demonstrated the suppression of halide exchange reaction homogeneously in the whole crystal by treating the initial crystals with constituent halide precursor solution. The change of emission color and spectra, along with the SEM images and EDX mapping confirmed the halide vacancy filling of the crystals. Furthermore, I also suppressed the halide exchange reaction at a specific area of the microrod crystals through vacancy filling using the NIR laser. The increased PL intensity under the laser irradiation revealed the vacancy filling and suppression of halide exchange reaction exclusively at the laser irradiated part. The enhanced PL lifetime values also suggested the vacancy filling and decrease of the nonradiative recombination at the laser irradiated part.

Furthermore, I fabricated the narrow-bandgap iodide-rich domains in the wide-bandgap brome microcrystals or nanocrystal films at the focal point of a NIR laser beam

and studied the charge carrier dynamics in the prepared heterostructures. The time-resolved photoluminescence studies revealed the transportation and accumulation of the photogenerated charge carriers in the low-bandgap region from the wide-bandgap regions. Thus, the laser trapping controlled spatial bandgap engineering and charge carrier recombination will be an important milestone to develop various perovskite-based heterojunction devices.

List of Papers Presented in Conferences

1. **Interfacial Transport and Collection of Photogenerated Charge Carriers in Bandgap Engineered Lead Halide Perovskite Heterostructures.**

   Md Shahjahan, Lata chouhan, Vasudevanpillai Biju

   The 101th Annual Meeting of the Chemical Society of Japan, Online Meeting, 19-22 Mar 2021 **[e-poster]**

2. **Site-specific Halide Vacancy Filling in Perovskite Microcrystals by Optical Trapping.**

   Md Shahjahan, Ken-ichi Yuyama, Vasudevanpillai Biju

   Chemistry Association Hokkaido Branch 2021 Winter Research Presentation, Sapporo, Japan, 26-27 Jan 2021 **[Oral]**

3. **Heterojunction Perovskite Microrods Prepared by Remote-Controlled Vacancy Filling and Halide Exchange.**

   Md Shahjahan, Ken-ichi Yuyama, Vasudevanpillai Biju

   The 21st RIES-Hokudai International Symposium, Sapporo, Japan., 10-11 Dec 2020 **[e-poster]**

4. **Optically-controlled Halide Vacancy Filling in Perovskite Microcrystals.**

   Md Shahjahan, Ken-ichi Yuyama, Vasudevanpillai Biju

   Annual Meeting of the Japanese Photochemistry Association 2020, Japan, 9-11 Sep 2020 **[Oral]**

5. **Bandgap Modification at Specific Sites of Lead Halide Perovskite under Laser Trapping by Local Halide Exchange Reaction.**

   Md Shahjahan, Md Jahidul Islam, Ken-ichi Yuyama, Vasudevanpillai Biju

   2019 International Symposium of Research Institute for Electronic Science (RIES) and the Center for Emerging Functional Matter Science (CEFMS), Sapporo, Japan, 3-4 Dec 2019 **[Poster]**

6. **Bandgap Tuning of Lead Halide Perovskite by Local Halide Exchange Reaction under Laser Trapping.**

   Md Shahjahan, Md Jahidul Islam, Ken-ichi Yuyama, Vasudevanpillai Biju

   The 20th RIES-Hokudai International Symposium, Sapporo, Japan, 2-3 Dec 2019 **[Poster]**

7. **Site-specific Bandgap Modification in Lead Halide Perovskites by Chemical Reactions under Laser Trapping.**

   Md Shahjahan, Md Jahidul Islam, Ken-ichi Yuyama, Vasudevanpillai Biju

   Okinawa Colloids, Nago, Okinawa, Japan, 3-4 Nov 2019 **[Poster]**

8. **Modification of Band Gaps in Lead Halide Perovskites by Chemical Reactions Under Optical Trapping.**

   Md Shahjahan, Md Jahidul Islam, Ken-ichi Yuyama, Vasudevanpillai Biju

   Chemistry Association Hokkaido Branch 2021 Summer Research Presentation, Sapporo, Japan, 20 July 2019 **[Oral]**

List of Publications

1. **Heterojunction Perovskite Microrods Prepared by Remote-Controlled Vacancy Filling and Halide Exchange.**

   Shahjahan, M.; Yuyama, K.I.; Okamoto, T.; Biju, V.

   Adv. Mater. Technol. **2021**, *6* (2), 2000934 (Featured on the cover page).

2. **Remote Tuning of Bandgap and Emission of Lead Perovskites by Spatially Controlled Halide Exchange Reactions.**

   Islam, M. J.; Shahjahan, M.; Yuyama, K. I.; Biju, V.

   ACS Mater. Lett. **2020**, *2* (4), 403–408 (Featured on the cover page).

3. **Shape-dependent Kinetics of Halide Vacancy Filling in Organolead Halide Perovskites**

   Okamoto, T.; Shahjahan, M.; Biju, V.

   Adv. Optical Mater. **2021**, 2100355